博士論文

Study on Air-Sea Interaction over East Asia Using a Regional Atmosphere-Ocean Coupled Model

（領域結合モデルを用いた東アジアにおける大気海洋相互作用に関する研究）

Guo Xiaojun

郭 暁君

Department of Civil Engineering

Graduate School of Engineering

The University of Tokyo

September 2019

Abstract:

The coarse resolution of current state-of-the-art global climate models (GCMs) limits their applications on regional scales as the finer scale information and local climate conditions cannot be resolved at the scale of GCM. Recently, the coupled regional climate models (RCMs) have become useful tools for simulation of regional-scale climate change process and impact studies due to the higher-resolution model forcings and inclusion of air-sea interactions. In this dissertation, a fully atmosphere-ocean coupled regional climate model RSM-ROMS is used, which consists of the atmosphere component, Regional Spectral Model (RSM) and the ocean component, Regional Ocean Modeling System (ROMS). The primary aim is to provide a more general and comprehensive assessments and understandings of the RSM-ROMS.

Chapter 2 aims to remove the systematic cold sea surface temperature (SST) biases over Subtropical Western North Pacific in RSM-ROMS. The long-standing cooler SST bias over Northwest Pacific is found to be pronounced in most Coupled Model Intercomparison Project Phase 5 (CMIP5) GCMs and some coupled RCMs, which limits the model skills in simulating the historical climate and making projection of future climate. Additionally, flux adjustment has been a big issue and so that investigated more in coupled GCMs with the aim to reduce the substantial model errors, but not so much in coupled RCMs. A set of experiments are carried out using RSM-ROMS by employing the flux adjustment and increasing the horizontal resolution from 25 km to 10 km, combinedly and separately, to explore their effects on the simulation of atmospheric and oceanic climate during the warmer season (May-August) in 2006. Both approaches exhibit apparent advantages in the SST simulation. The largest reduction (around 1.09 °C) in cold SST bias can be achieved when the two methods are combined. Among all surface heat flux components, the latent heat flux exhibits the most prominent improvement, which is associated with the improved simulations of the near-surface wind speed and air-sea humidity difference. Flux adjustment appears to exert large positive impacts on the simulation of most atmospheric variables and some oceanic variables in the upper ocean layer. Noted that very small differences are detected in the ocean currents when the flux adjustment is adopted. Increasing spatial resolution can improve the climate simulation in most aspects, especially in the simulation of ocean dynamic and thermodynamic process, no matter whether the flux adjustment scheme is activated or not. Fine grid experiment better captures the observed mean Kuroshio Current path South of Japan due to the better representation of mesoscale eddy activities while the coarse grid run produces the erroneous path. Noted that both approaches cannot guarantee the improved performances in all aspects, and their effects are time and space dependent.

In another aspect, air–sea interaction on the intraseasonal timescales is essential for weather prediction and climate simulation. The advantages of air-sea coupling in the East Asia climate have been well revealed in the previous studies. However, it is still unclear whether RSM-ROMS has the ability to reproduce the realistic feedbacks in the climate system. Thus, chapter 3 aims to confirm the fidelity of this fully coupled RCM in simulating the features of intraseasonal air-sea interaction over East Asia. The intraseasonal (10-60-day) variability over East Asia during 1999-2008 is examined using the coupled model RSM-ROMS and uncoupled model RSM at a resolution of 25

km. Compared with the uncoupled run, the coupled model is more skillful in simulating the intensity of intraseasonal rainfall. In particular, the features (e.g., propagation direction) of eastward propagating boreal winter intraseasonal oscillation and associated MJO events are well captured in the coupled run in spite of slightly weaker amplitude while the uncoupled model misrepresents this phenomenon in the entire tropical regions. The coupled model better reproduces the observed spatial and temporal characteristics (e.g., quadrature phase relationship, amplitude) of intraseasonal SST-precipitation relationship, especially over Western Pacific. However, the uncoupled model forced by prescribed SST tends to produce in-phase variation due to the spurious SST forcing. Additional experiment confirms that the inferior representation in the uncoupled run is due to lack of coupling rather than the atmospheric bias which is unrelated to coupling. The improved simulated positive surface shortwave radiation-SST feedback in the coupled run is potentially attributed to the improved simulation of negative SST-cloud feedback. The temporal coupling feedbacks between the atmosphere and ocean surface can be captured by the coupled model although there are slight differences in the phase lag of time compared with observation.

Chapter 4 aims to clarify the main process responsible for the SST variation by quantifying the relative contribution of atmospheric process to the SST tendency in RSM-ROMS. The atmospheric process (i.e., net surface heat flux) has a leading contribution to the SST variation in RSM-ROMS. However, the coupled model tends to overestimate the contribution of net heat flux in most oceanic region due to the simulated shallower mixed layer depth. The shortwave radiation and latent heat flux are two primary contributing components. Overall, the coupled model RSM-ROMS has substantial advantages in the local air-sea interaction simulation.

Some deficiencies still remain in RSM-ROMS, such as the lower intraseasonal SST variation and shallower mixed layer depth. Chapter 5 focuses on exploring how well the higher horizontal or ocean vertical resolution improves the mean climate and intraseasonal variability. The thicker thickness (around 10 meters) of uppermost layer in the ocean submodel is insufficient to resolve the vertical variation near the ocean surface, which possibly restricts the model capabilities in simulating the realistic upper ocean heat budget for RSM-ROMS. Thus, in order to explore the impacts of higher vertical resolution, two experiments are conducted with 30 layers (around 10 meters) and 50 layers (around 0.5 meters) for the settings of ocean layers (thickness of uppermost layer), respectively. The results show that increasing vertical resolution effectively enhances the lower intraseasonal SST variation over the Kuroshio-Oyashio Current region due to the lower thermal inertia caused by thinner uppermost layer thickness. The shallower mixed layer depth over Western Pacific and Indian Ocean deepens with the magnitude of approximately 10 meters by increasing the vertical resolution. Following the improved simulation of mixed layer depth, the contribution of atmospheric process to SST variation is more realistically presented, with the originally overestimated contribution percentage reduced at a magnitude up to 20%. However, increasing vertical resolution cannot improve or even slightly degrade the simulation of salinity in the maritime continent and coastal regions where there is huge input of grand rivers, indicative of the necessity to introduce the river routing scheme. In another aspect, two experiments are performed over tropical regions with 25 km and

10 km resolution, respectively. Better overall representation of ocean thermodynamics is obtained in tropical regions with an increase of horizontal resolution from 25 km to 10 km. Most importantly, higher horizontal resolution produces more realistic features (e.g., amplitude and direction) of MJO-related convection propagation with higher pattern correlation coefficient.

In general, increasing the horizontal and ocean vertical resolution lead to subtle but significant changes in the mean climate (especially ocean thermodynamics) and intraseasonal variability. It should be mentioned that the effects of modifying model resolution are straightforward and model dependent. The finer-resolution simulations are not always superior, implying that the model physical and dynamical configuration at this resolution might not be optimal. Moreover, compared with observation, the coupled simulations still remain deficient such as weaker intensity of MJO-related convection propagation and shallower mixed layer depth. The RSM-ROMS might exhibit better performance than reported here using improved physics schemes (e.g., mixing, radiation, convection and cloud schemes) in the individual submodels.

To conclude, the benefits of air-sea coupling, increasing horizontal and ocean vertical resolution in RSM-ROMS have been well demonstrated in this thesis. It is verified that RSM-ROMS is an effective and powerful tool to simulate the natural climate system and conduct impact assessments. It not only greatly compensates the previous studies but also facilitates further development of the higher resolution version of RSM-ROMS.

Acknowledgements

First, I would like to express my sincere gratitude to my advisor Professor Kei Yoshimura for his guidance and support for my PhD study in these three years.

Many thanks also to the co-supervisors Professor Kazuhisa Tsuboki, Professor Taikan Oki, Professor Hiroyasu Hasumi and Professor Yoshimitsu Tajima who kindly provided me a lot of insightful suggestion and comments, which inspired me to improve my research from various perspectives.

Thanks to Tomoko Nitta who always kindly gave me suggestion and patiently helped me solve the problem either in the research or life.

Thanks to Inna who enriched my life in Japan and accompanied me to spend a lot of late nights in the lab.

Thanks to all the lab members and secretaries who helped me and made me feel warm.

Thanks to The University of Tokyo which provided me the scholarship and supported me to finish my study.

Finally, I would like to give great thanks to my parents and my sister for giving me enormous supports spiritually and accompanying me through the tough time. Although we are far away from each other, but I know you are always behind me.

I hope I could be stronger and braver to pursue and protect what I want, find myself and be myself.

Summer ends, life still goes on.

Table of Contents

List of Figures

List of Tables

Chapter 1

Introduction

1.1 Research background

1.1.1 Development of coupled global climate models

The earliest attempts to global climate models (GCMs) is the atmospheric GCMs with prescribed SST and sea ice. Nevertheless, the components (e.g., atmosphere, ocean, hydrosphere) of the climate system should not be treated independently. Thus, the atmosphere and ocean components are combined to form the atmosphere-ocean general circulation models (AOGCMs). The air–sea coupling has become crucial in explaining the climate processes on the time scales from the subseasonal to decadal variability. The concept of air-sea coupling is straightforward: large-scale sea surface temperature (SST) anomalies induce atmospheric cooling or diabatic heating, which further modify the atmospheric circulation as well as the heat fluxes and wind stresses at the air-sea interface (Fedorov, 2008). In the late 1960s, the first coupled ocean-atmosphere GCM occurred with idealized land-ocean distributions employed (Manabe and Bryan, 1969). Later the coupled GCMs suffered from the climate drift caused by the imbalances of heat fluxes, and the modellers used some approaches (e.g., flux adjustment, tuning of convection, cloud parameterization scheme) to solve this issue (e.g., Sausen et al., 1988). The need for flux adjustment gradually diminished with increasing knowledge of physical processes controlling the climate system.

1.1.2 Development of coupled regional climate models

Although nowadays the coupled AOGCMs have been maturely developed, some big challenges remain to be realized. Most of current state-of-the-art coupled GCMs are run at a coarser resolution with scales of hundreds of kilometer, which limits their application on regional scales. Some important finer-scale information in determining orographic rainfall and other important climate phenomena cannot be resolved at the scale of GCM. Additionally, the atmosphere and ocean components in current AOGCMs often use different horizontal grids with the consideration for computational cost. How to link different components in a flexible, scientifically sensible and computationally affordable ways is still one of big issues to be addressed in current coupled GCM (Harris, 2018).

The alternative method to overcome these limitations is the development of regional climate models (RCMs). The high resolution RCMs allow better representation of fine-scale climate processes and feedbacks by providing regional-scale forcings (e.g., land cover; high-resolution orography; topography; land-ocean coastlines) lost in coarse-scale GCMs, which further facilitates the impact studies which demands information on much finer spatial scales (Rummukainen, 2010). The occurrence of RCMs allows us to focus on the climate change over the area of interest, which supports the decision and adaptation studies for the climate service community.

As the atmosphere-only RCMs neglect the regional air-sea feedback, the RCM research community has stepped into the transition point: from the hydrostatic atmospheric models to the very high-resolution RCMs coupled with other components of climate system such as atmosphere-ocean coupling, atmosphere-chemistry/aerosol coupling RCMs (Schrum, 2017; Giorgi and Gao, 2018). In particular, the coupled models typically outperform the uncoupled ones in simulating the extreme weather phenomena over the ocean due to the realistic air-sea coupling (Li et al., 2012; Wei et al., 2014). The simulation outputs from RCMs are extensively used in the climate change impact studies of different sectors (e.g., agriculture, hydrology, air quality) (Giorgi, 2019).

However, there is still not a generally standard in spite of growing use of the A-O fully coupled RCMs in regional climate change assessments (Schrum, 2017). More RCMs are now being applied at the horizontal resolutions of 5-10 km, or even go down to 1-2 km. Hence, some problems (e.g., expensive computation, increased computational potentials) still remain unresolved in current state-of-the-art coupled RCMs, which potentially limits the advancement of high-resolution version coupled RCMs. The technical and human resources need to be balanced by carefully selecting the suitable modeling strategy (Schrum, 2017).

In this study, a fully couple regional atmosphere-ocean system of Regional Spectral Model and Regional Ocean Modeling System (RSM-ROMS) model is used. The detailed description of this model will be shown in chapter 2. It has been extensively used in the studies of climate assessments and projections, and proved to perform well in the historical climate simulation (Ham et al., 2016; Misra et al., 2018; Dai et al., 2018) and future climate projection (Li et al., 2012). Some previous studies suggest that using a stand-alone model might still be acceptable or even perform better in some applications (Schrum, 2017). But it heavily depends on the model physics itself. Thus, the benefit and disadvantages of the coupled RCM (i.e., RSM-ROMS) needs to be well clarified by comparison with the uncoupled one.

In another aspect, increasing the spatial resolution is one of the effective methods for coupled GCMs to reduce the systematic model biases and improve the monsoon intraseasonal oscillation (MISO) simulation (e.g., Peatman and Klingaman, 2018). However, high-resolution

global simulations usually demand vast computational resources that cannot be afforded by many modellers. One of the biggest advantages in the RCM is that it is cheaper than a GCM at the same resolution. More RCMs are now being applied at the horizontal resolutions of 5-10 km. Large-scale tropical climate phenomena (e.g., MJO) in previous studies are investigated using a coarse-resolution AGCM coupled to either a coarse-resolution ocean General Circulation Models (OGCM) or an idealize one-dimensional model to assess the feedback effect. There is still little work on the sensitivity of tropical intraseasonal variabilities to different horizontal resolutions using a high-resolution fully coupled RCM framework. Li et al. (2012) shows that RSM-ROMS effectively reproduces the realistic small-scale oceanic features in the 10-km resolution run. However, the effects of higher resolution on simulation of ocean thermodynamics and intraseasonal oscillation have not yet been tested in other regions.

1.2 Research objectives

The general objective of this study is to provide a more general and comprehensive assessments and understandings of the RSM-ROMS, and develop a very high-resolution version coupled RCM for impact and vulnerability assessment in natural ecosystems and other human activity sectors.

With the aim to clarify to what extent the coupled RCM could reproduce the nature climate system, the local intraseasonal air-sea interaction and some important tropical intraseasonal activities are assessed and quantified in the coupled RSM-ROMS compared with its atmosphere-only model RSM. The main processes contributing to the SST variation and possible discrepancies in RSM-ROMS are also revealed.

With the motivation to develop a high-resolution version of RSM-ROMS, the finer horizontal resolution and vertical ocean resolution are used to obtain a better representation of oceanic thermodynamics and the tropical intraseasonal activities over East Asia.

1.3 Organization of this thesis

The thesis is organized as follows. Chapter 2 describes the effects of flux adjustment and model horizontal resolution on the climate simulation over Subtropical Western North Pacific. The assessments of local air-sea interaction on intraseasonal timescales over East Asia are given in chapter 3. Contributions of atmospheric and oceanic processes to SST variation are investigated in chapter 4. Impacts of higher horizontal and vertical ocean resolution on mean climate and intraseasonal variability over East Asia are examined in chapter 5. Finally, chapter 6 presents the conclusions and future work.

Chapter 2

Climate simulation over Subtropical Western North Pacific: effects of heat flux adjustment and horizontal resolution

2.1 Introduction

Ocean is the lower boundary for atmosphere and covers a large part of the earth. Atmosphere and ocean exchange the energy, mass and momentum at the air-sea interface. Sea surface temperature (SST) could lead to changes in the atmospheric (e.g., wind stress) and oceanic climate (e.g., upwelling and downwelling) which in turn modify SST itself (Chelton and Xie, 2010). The long-standing systematic model SST bias in the coupled models limits the skills in climate simulation, creates the uncertainties within models and produces the significant model spreads in the future climate projection (e.g., Prodhomme et al., 2014). Thus, a realistic air-sea interaction in coupled models is highly dependent on an accurate representation of the SST, which is favorable to the better modeling of other climate feedbacks.

The systematic SST bias within the coupled models is still an unresolved problem, which hinders the development of coupled GCMs and RCMs. In terms of the coupled RCMs, the long-standing cold SST bias over Asia-western North Pacific monsoon domain has been found to be pronounced in most Coupled Model Intercomparison Project Phase 5 (CMIP5) GCMs and some state-of-the-art coupled RCMs (e.g., Zou and Zhou, 2011, Wang et al., 2018). Zou and Zhou (2013) showed that the cold bias of simulated summer mean SST was around 2°C over the Kuroshio region and the coastal region of East Asia using a flexible regional ocean–atmosphere–land system model.

The cold SST bias also occurred over the Western North Pacific Ocean in the coupled regional model RSM-ROMS (Ham et al., 2016; Dai et al., 2018). It remains a grand challenge to correct this cooler SST bias. The model SST bias was ascribed to a number of complex feedbacks and processes, including the mismatch of net surface heat flux between atmosphere and ocean component (Han et al., 2012; Ham et al., 2016), spurious ocean dynamic and mixing processes(Song et al., 2015), bias in the net downward shortwave radiation associated with cloudiness(Dai et al., 2018) .

A great deal of efforts has been made to remove the systematic bias within the models by adopting some approaches. Physical tuning is the most common method used to alleviate the bias

within the RCMs. Zou and Zhou (2011) showed that the cold bias over Northwest Pacific Ocean could be effectively reduced by enhancing the convection suppression based on the case of 1998 summer monsoon. However, parameter tuning is computationally expensive and time-consuming. A quick and cheaper alternative method to remove the bias is flux adjustment (or flux correction). Contrary to the parameters optimization that will create artificial compensating error interactions, flux adjustment does not introduce these errors between submodels (Dommenget and Rezny, 2018). The main benefit of flux adjustment is that it is more transparent and easy to quantify. This method is traditionally used in the GCMs to avoid the drift of simulated climate away from a realistic state and maintain a stable climate state through adding fluxes (e.g., heat, freshwater or momentum) at the surface of ocean model (Sausen et al., 1988). The accuracy of SST simulation is directly affected by the sea surface heat flux. In order to balance the inconsistences of surface heat flux between different sub-systems of coupled models, the flux adjustment is applied during the coupling process in the model.

Although the flux adjustment becomes less common with the development of physical schemes optimization, nowadays it is still used by some state-of-the-art GCMs (e.g., Peatman and Klingaman, 2018). Based on a coupled GCM, it was found that the heat flux adjustment could reproduce more realistic mean climate (e.g., SST, precipitation, wind stress) and slightly improve the ENSO hindcast skill (Pan et al., 2011). Ding et al. (2013) used a fully coupled atmosphere-ocean-sea-ice model and revealed that heat flux correction could improve the upper ocean temperature and the wind stress fields followed by the enhancement of thermocline tilt along the equator. Pookkandy et al. (2016) showed that significant flux correction in the temperature was essential to maintain the upper ocean stratification close to the observations based on a coupled single column ocean model. Li et al. (2012) briefly mentioned that the prominent systematic warm bias over the Southern half of the California coastal region was effectively removed with flux adjustment introduced in RSM-ROMS.

Another convenient solution to remove the systematic bias is higher resolution. In recent years, increased computing power has made it possible to develop the coupled models at a much finer spatial resolution. Many previous studies have shown that high resolution improves model accuracy and allows important small-scale processes to be simulated. Miliniski et al. (2016) found that high horizontal resolution could eliminate the warm bias close to the African coast due to the better representation of the wind stress using a global coupled climate model. Based on a coupled regional climate model, Akhtar et al. (2017) showed that finer grid improved the wind speed over coastal regions and subsequently the simulations of turbulent heat flux. Li et al. (2012) showed that the 10-km resolution experiment could better generate the finer-scale oceanic features (e.g., warming the

SST, decrease the upwelling motion) over California Current System using RSM-ROMS. Thus, the development of high-resolution RCMs is crucial to enhance the fidelity of oceanic climate simulation.

This study is motivated by three aspects: first, flux adjustment has been a big issue and so that investigated more in coupled GCMs, but not so much in coupled RCMs. Second, the pronounced cold SST bias over Northwest Pacific Ocean occurs in most coupled RCMs and remains unsolved. Third, there are sharp SST gradients and active eddies over the Kuroshio Extension region Southeast of Japan. It is essential to reproduce these distinct thermodynamic features of ocean in models. The aim of this study is to evaluate the model performance of the employed methods (i.e., flux adjustment and increasing model horizontal resolution) in improving the atmospheric and oceanic simulation over Subtropical Western North Pacific(SWNP) based on a regional air-sea coupled climate model RSM-ROMS, which further provides some hints in the development of air-sea coupled RCMs.

2.2 Model, experiment and validation dataset

2.2.1 RSM-ROMS model

The model used in this study is a fully coupled atmosphere-ocean regional climate model (RSM-ROMS) based on the Regional Spectral Model RSM for the atmosphere component and the regional ocean model ROMS version 3 for the ocean component (Li et al., 2012).

The atmosphere component RSM is a hydrostatic regional atmospheric model (Juang et al., 1997; Juang and Kanamitsu, 1994), which has been used in many dynamical downscaling studies. There are 28 sigma levels in the atmosphere. The following physical parameterization schemes are used: the Relaxed Arakawa Schubert scheme for convective parameterization (Moorthi and Suarez, 1992); the fractional cloudiness scheme of Slingo (1987); the four-layer community Noah land surface model (Ek et al., 2003).

The ocean model component ROMS is a three-dimension, free-surface, terrain-following model (Shchepetkin and McWilliams, 2003). Thirty sigma coordinate levels are used with at least five grid points existing in the top 100 meters. Either local or nonlocal closure scheme could be used for the vertical mixing parameterization in ROMS. The local closure schemes are the Generic Length Scale parameterization (GLS, Umlauf and Burchard, 2003) and Mellor-Yamada Level 2.5 (Mellor and Yamada, 1982). The GLS is a two-equation turbulence model that allows a wide range of

vertical mixing closures, which consists of the popular k-kl (Mellor-Yamada level 2.5), k-e, and k-w schemes. The nonlocal closure boundary scheme is the K-profile boundary layer scheme (Large et al., 1994), which has been expanded to include both surface and bottom oceanic boundary layers. In this ROMS configuration, the local GLS approach is activated as the mixing scheme. The performances of these schemes are testified in some previous studies (e.g., Warner et al., 2005a). The bathymetry data is obtained from 5-Minute Gridded Global Relief Data (ETOPO5), which is a 5 arc-minute global relief model of the Earth's surface that integrates land topography and ocean bathymetry.

The atmospheric lateral forcing is derived from the T62L28 6-hourly National Centers for Environmental Prediction (NCEP)/Department of Energy (DOE) reanalysis (R-2) [Kanamitsu et al., 2002]. A new spectral nudging scheme developed by Hong and Chang (2012) is applied for the lateral boundary conditions. The Monthly Simplified Ocean Data Assimilation (SODA) dataset with a resolution of 0.5 degree is served as the oceanic lateral forcing. RSM and ROMS share the same grids without interpolation in the coupling process. The coupling between the atmosphere and ocean components takes place every 24 hours.

2.2.2 Heat flux adjustment

Flux adjustment is a quick correction of the surface net heat flux by inserting the actual observed SST information. The sea surface net heat flux provided by the atmosphere to the ocean is modified by adding a correction term that scales with the SST error of the model.

The equation of corrected net heat flux on the ocean surface can be described as:

$$NHF = NHF_{(model)} + dQdSST \times (SST_{(model)} - SST_{(ref)}) \quad \textbf{(Eq. 2.1)}$$

Where $dQdSST$ is the SST relaxation coefficient, $SST_{(model)}$ is the sea surface temperature of the model and $SST_{(ref)}$ is derived from monthly mean climatology Optimally Interpolated Sea Surface Temperature (OISST) dataset. $NHF_{(model)}$ is the net downward heat flux calculated in the model while NHF is the corrected one. The NHF consists of the net shortwave radiation (SWR), longwave radiation (LWR), latent heat flux (LHF) and sensible heat flux (SHF). The net downward surface heat flux can be expressed as: NHF =SWR+LWR+LHF+SHF. All the sea surface heat fluxes in this equation is positive for the downward direction.

In order to correct the mean state toward the observed, the flux correction term (i.e., $\Delta Q =$

$dQdSST \times (SST_{(model)} - SST_{(ref)})$) is added to the tendency equation of the sea surface temperature in the models as a constant or seasonally changing value. The SST relaxation coefficient $dQdSST$ indicates the surface net heat flux sensitivity to the sea surface temperature. In this study, the NHF is corrected by adding a linear relaxation of ocean model SST towards observed SST. Thus, the SST relaxation coefficient $dQdSST$ is set to the constant value.

2.2.3 Experimental design

Figure 2.1 shows the simulation and analyzed domain (SWNP, 23°N–36°N, 130°E–162°E) which covers part of the Kuroshio Extension region. RSM-ROMS exhibits pronounced cold SST bias over this region. Additionally, the stronger SST gradient, most active ocean currents and largest air-sea surface heat flux exchange take place over this region (Qiu, 2002). It is necessary to explore the capabilities of high-resolution model to capture these distinct oceanic features. Thus, the domain is chosen for analysis taking the computation time into account as well.

To investigate the impact of flux adjustment and increasing model horizontal resolution on the climate simulation, a set of experiments are carried out, combined and separately (Table 2.1). The same surface atmospheric forcings, oceanic forcings, and initial conditions are used for these experiments. The twin experiments CTL_25km and CTL_10km were conducted without flux adjustment, but with a horizontal resolution of 25 km and 10 km, respectively. In order to explore the effect of flux adjustment intensity, additional experiments with a weak (i.e., dQdSST = -50 W/m^2/°C) or strong SST relaxation coefficient (i.e., dQdSST = -100 W/m^2/°C) are conducted. FLX(50)_25km and FLX(100)_25km indicate that the experiments are run with flux adjustment at a horizontal resolution of 25 km, but with dQdSST values of -50 and -100 W/m^2/°C, respectively.

Each experiment is integrated from 1 January to 31 December 2006, and the results during May-August are analyzed.

Table 2.1 List of experiments performed

Name	Resolution (km)	Flux adjustment scheme setting
CTL_25km	25 km	Without heat flux adjustment
FLX(50) _25km		With flux adjustment (dQdSST = -50 W/m^2/°C)
FLX(100)_25km		With flux adjustment (dQdSST = -100 W/m^2/°C)
CTL_10km	10 km	Without heat flux adjustment
FLX(50) _10km		With flux adjustment (dQdSST = -50 W/m^2/°C)
FLX(100)_10km		With flux adjustment (dQdSST = -100 W/m^2/°C)

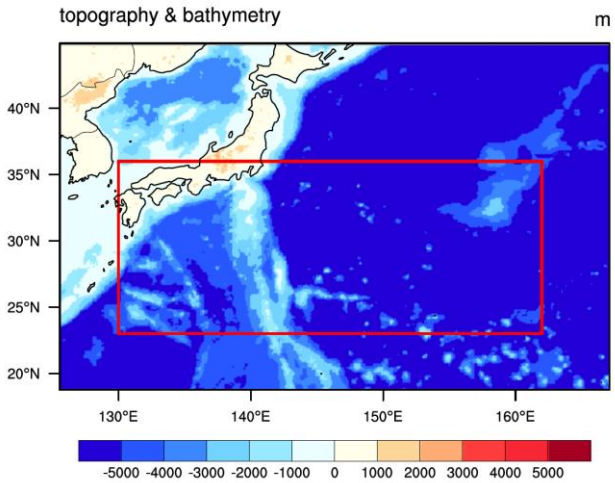

Figure 2.1 Simulation domain, model topography and bathymetry (unit: meter) from ETOPO5 for RSM-ROMS simulation. The red box indicates the analyzed domain.

2.2.4 Validation dataset

In this study, only the climate over the ocean is analyzed, land is excluded using mask analysis. Multiple validation data sets are used to evaluate the coupled model performances. Model-simulated sea surface temperature is compared with the monthly OISST version 2 dataset with a resolution of 0.25 degree (Reynolds et al., 2007). Precipitation is validated with the Global Precipitation Climatology Project (GPCP) monthly product with a resolution of 2.5 degree (Huffman et al., 1997). Latent heat, sensible heat flux and surface net heat flux are evaluated using the Objectively Analyzed air-sea Fluxes (OAFlux) product at 1.0 degree resolution (Yu et al., 2008). Shortwave and longwave radiation are compared against the International Satellite Cloud Climatology Project (ISCCP) radiation on a 1x1 degree grid (Zhang et al., 2004). The 10-meter zonal and meridional wind is verified by the Quick Scatterometer (QuikSCAT) Level 2B Ocean Wind product from the Jet Propulsion Laboratory website (Dunbar et al., 2006). Zonal and meridional wind stress components are validated with the QuikSCAT satellite wind stress on a 0.5°×0.5° latitude-longitude grid from Centre ERS d'Archivage et de Traitement (CERSAT) [Centre ERSd'Archivage et de Traitement, 2002].

The validation dataset for ocean state simulation is derived from SODA 2.2.4 dataset, which provides an oceanic reanalysis including the temperature, salinity, zonal and meridional velocities and vertical velocity with a horizontal resolution of 0.5 degree and 40 vertical levels (Carton and Giese, 2008). The sea surface height is assessed using the monthly satellite altimetry product of the Archiving, Validation, and Interpretation of Satellite Oceanographic (AVISO) (http://aviso.oceanobs.com) [Ducet et al., 2000].

10-meter wind speed ($ws10$) is calculated based on the following equation:

$$ws10 = \sqrt{u10^2 + v10^2} \quad \textbf{(Eq. 2.2)}$$

Where $u10$ and $v10$ are 10-meter zonal and meridional components of 10-meter wind speed, respectively.

Wind stress magnitude (τ) is calculated based on following equation:

$$|\tau| = \sqrt{\tau_x^2 + \tau_y^2} \quad \textbf{(Eq. 2.3)}$$

Where τ_x and τ_y are the zonal and meridional component of wind stress, respectively.

The ocean heat content (*OHC*) is calculated based on the following equation:

$$OHC = Cp \int_{h2}^{h1} \rho T dZ \quad \textbf{(Eq. 2.4)}$$

Where Cp is the specific heat capacity of the ocean water (i.e., 3850 J/(kg·°C), ρ is the density of sea water (i.e., 1025 kg·m^{-3}), $h1$ is the top depth of ocean layer, $h2$ is the bottom depth, T is the ocean temperature (unit: °C).

The mixed layer depth is defined as the shallowest depth with the ocean temperature differing from corresponding ocean temperature at the depth of 13 meters by 0.5 °C. The vertical profiles of ocean temperature at each grid are vertically interpolated into every 1-meter interval to guarantee the accuracy of mixed layer depth calculation. The observed MLD is calculated based on the monthly ocean temperature from SODA 2.2.4 dataset.

2.3 Impacts on atmospheric simulation

2.3.1 Sea surface temperature and precipitation

SST is the direct product of air-sea interaction, and plays an important role in governing the ocean's heat content and regulating climate. Thus, the impacts on SST simulation is first given in this section. The monthly variations of SST bias between model and observation for all experiments is shown in Figure 2.2. This cold bias persists throughout the whole year, peaking in July and in December with the magnitude of around -2.03 °C and -1.37 °C in the CTL_25km run. As the bias is more prominent in the warmer season, thus the following analysis about the impacts of flux adjustment and increasing resolution on the climate simulation is based on the warmer months from May to August (MJJA). The regional mean SST bias during MJJA is reduced from -1.53 °C in CTL_25km to -0.58 °C in FLX(50)_25km by the effect of flux adjustment. It is noted that the benefit of higher resolution is less apparent if flux adjustment is introduced. More notable improvement caused by increasing resolution occurs in the twin experiments without flux adjustment, with cold SST bias reduced by 0.43°C in the CTL_10km compared with the CTL_25km. The largest reduction of the cold bias (around 1.09°C) is achieved when flux adjustment and increasing resolution are combined (i.e., FLX(50)_10km), even the effect is not a linear superposition. The increase of absolute value of SST relaxation coefficient dQdSST from 50 W/m^2/°C (FLX(50)_25km) to 100 W/m^2/°C (FLX(100)_25km) gives an extra slight reduction of the cold SST bias (around 0.16 °C).

Figure 2.3 shows the spatial correlation coefficient (SCC) and root mean square error (RMSE) of SST and precipitation between simulations and observation during MJJA. The RMSE is reduced by 0.11 °C and 0.13 °C in the FLX(50)_25km and FLX(100)_25km compared with CTL_25km, indicating that the improvement of SST weakens with stronger SST relaxation (Figure 2.3(a)). The

largest reduction of RMSE by the impact of increasing resolution occurs when the flux adjustment scheme is deactivated, with the decrease of 0.05 °C in the CTL_10km compared with CTL_25km.

SST could affect the precipitation through the modulation of atmospheric instabilities. The RMSE of precipitation is substantially reduced by approximately 0.52 and 0.66 mm/day in the experiments of FLX(50)_25km and FLX(100)_25km compared with the CTL_25km (Figure 2.3(b)). However, the spatial pattern is not further improved, with the magnitude of SCC reaching 0.84, 0.80 and 0.79 in the CTL_25km, FLX(50)_25km and FLX(100)_25km, implying that stronger flux adjustment exhibits a slight degradation of precipitation simulation over this region. The response of precipitation to the SST warming is more complicate as it is also affected by other climatic factors. Thus, the improved SST does not guarantee the corresponding improvement in the precipitation.

In another aspect, contrary to the improvement of SST at a finer grid, increasing resolution exhibits an adverse effect on the precipitation simulation (Figure 2.3(b)), with slight decrease (increase) of the SCC (RMSE). It indicates that the parameterization in model physical and dynamical configuration might not be appropriate at a finer resolution. Stronger flux adjustment could make the model SST closer to the observation. However, it also slightly degrades the spatial distribution of precipitation with excessive net heat flux adjusted. It is supposed that the coupled model could sustain a relatively good skill of all the climatic variables when heat flux adjustment remains small. Thus, the following analysis will focus on the comparison of the results between the experiments without flux adjustment and that with weak flux adjustment (i.e., dQdSST = -50 $W/m^2/°C$).

Figure 2.4 presents the spatial variations of bias in SST and precipitation for different experiments (upper and middle panels). In the CTL_25km run, the SST during MJJA exhibits the cold bias over most of the oceanic region except the coastal region of Southeast Japan, which is gradually alleviated with flux adjustment introduced and model resolution enhanced. In particularly, the colder SST bias over South of the Kuroshio Current is significantly improved, the warm bias near the coastline of Japan is also reduced. The improvement in the cold SST bias by the flux adjustment effect is latitude-dependent (Figure 2.4(e)), with largest reduction found at the lower latitudes (e.g., compared FLX(50)_25km with CTL_25km). It is noted that finer resolution reduces the cold SST bias more at latitudes North of 30°N when flux adjustment scheme is turned off. The most notable improvement in SST simulation throughout all the latitudes is attained when the two methods are combined.

The spatial distributions of precipitation averaged from May to August for different experiments and observation is shown in Figure 2.5. In observation, the heaviest rain band is

located over the Southeast coast of Japan, and decreases from the Northwest to the Southeast over SWNP. All the four experiments are able to capture the observed rainfall pattern. The dry rainfall bias is reduced most significantly at latitudes South of 30°N (Figure 2.5(j)). The precipitation over the coastal area of Southeast Japan is largely overestimated at a finer resolution of 10-km (Figure 2.4(c-d)), which possibly leads to the slight larger RMSE in the CTL_10km and FLX(50)_10km run (Figure 2.3(b)).

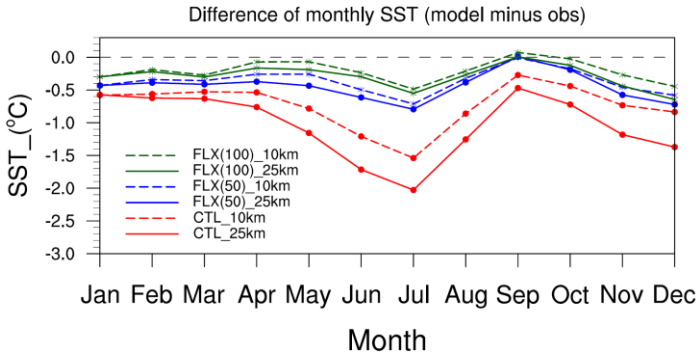

Figure 2.2 Monthly variation of SST bias (model minus observation, unit: °C) in different experiments for the period during January - December 2006.

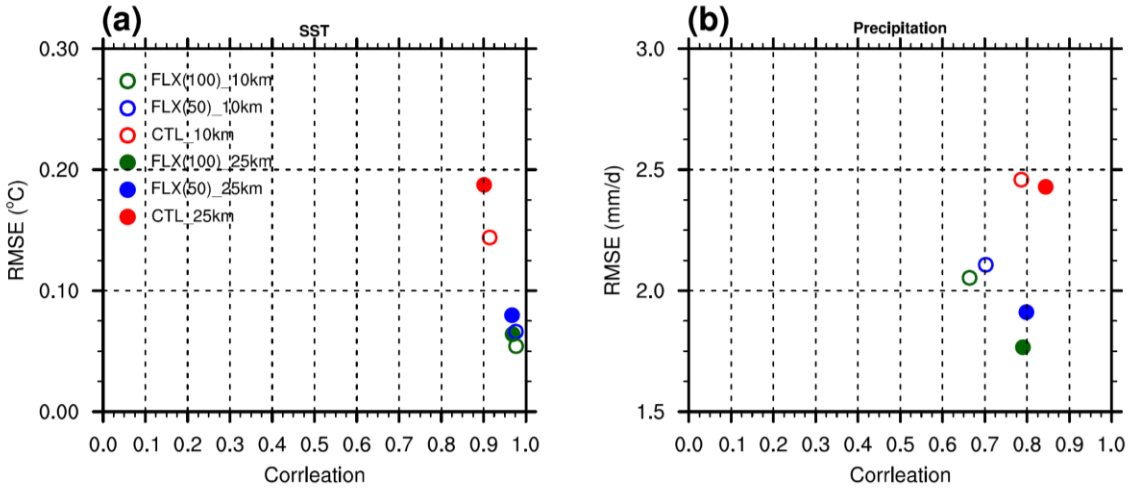

Figure 2.3 Scatter plots of spatial correlation coefficient and root mean square error (RMSE) for (a) SST and (b) precipitation during May-August 2006.

(x-axis indicates the spatial correlation coefficient, y-axis indicates the RMSE)

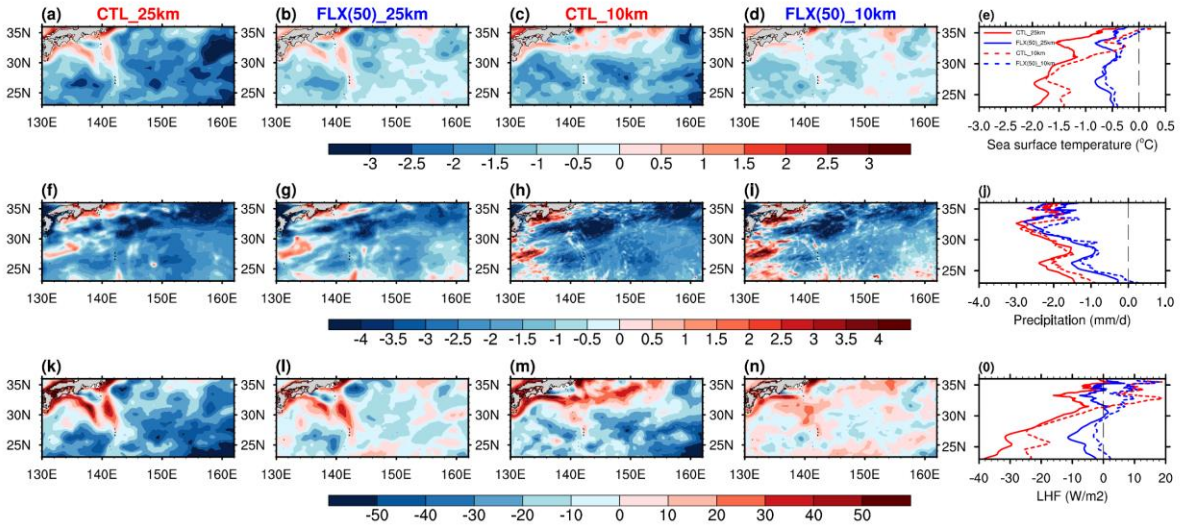

Figure 2.4 Spatial pattern of difference in SST (unit : °C) between (a-d) four experiments and observation (model minus observation) and (e) latitude cross section of zonally averaged (130°-162°E) SST bias during MJJA in the experiments of CTL_25km (red solid line), CTL_10km (red dash line), FLX(50)_25km (blue solid line) and FLX(50)_10km (blue dash line).

The middle panel (f-j) is same as the upper panel, but for the precipitation (unit: mm/day). The lower panel (k-o) is same as the upper panel, but for the latent heat flux (positive upward, unit: W/m^2).

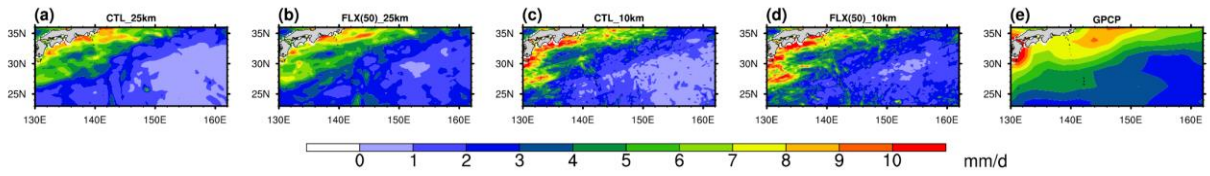

Figure 2.5 Spatial pattern of precipitation (unit: mm/day) for (a-d) four experiments and (e) GPCP during May-August 2006.

2.3.2 Surface heat fluxes

The exchange of heat fluxes at the air-sea interface greatly affect the SST variation, instead, the change in SST can modulate the surface heat flux. The corrected SST could introduce a thermal feedback to correct the surface net heat flux. Thus, how the surface heat fluxes respond to flux adjustment and increasing resolution needs to be examined.

Figure 2.6 provides the SCC and RMSE of the regional-averaged net surface heat flux and four heat flux components (i.e., SWR, LWR, LHF and SHF) between four experiments and observation during MJJA. Flux adjustment has little impact on the longwave radiation simulation. However, its effects on the shortwave radiation, latent heat and sensible heat are much more remarkable. Following the warming of SST by the flux adjustment effect, the RMSE (SCC) of the LHF and SHF are reduced (increased) by 16.21 W/m^2 (0.32) and 3.09 W/m^2 (0.15) in the FLX(50)_25km , respectively, compared with the CTL_25km. In contrast to the positive impacts on the turbulent fluxes, flux adjustment has a negative effect on the shortwave radiation. There is a slight performance degradation on the shortwave radiation with an increase of RMSE. Caused by the larger improvement in the turbulent fluxes, the NHF simulation is subsequently improved by the effect of flux adjustment in spite of worse performance in the shortwave radiation. In another aspect, increasing resolution exhibits slight improvements in both radiative and turbulent fluxes in the experiments either with or without flux adjustment. It is noted that the combination of these two methods obtains the best result in the heat fluxes simulation except shortwave radiation. For example, the RMSE and SCC for surface net heat flux are 28.75(18.00) W/m^2 and 0.59(0.75) in the CTL_25km (FLX(50)_10km) run. More (less) latent heat flux is released from the ocean in the region where warmer (cooler) SST bias occurs (upper and lower panels in Figure 2.4). In the 10-km resolution runs, more released latent heat flux accompanying with excessive evaporation might lead to the heavier rainfall over Southeast coast of Japan (middle and lower panels in Figure 2.4). More (less) upward latent heat flux is partially attributed to the increased (decreased) air-sea specific humidity (Figure 2.9). The SCC(RMSE) are 0.77(0.90 g/kg), 0.92(0.61 g/kg), 0.82(0.69 g/kg) and 0.95(0.73 g/kg) in the CTL_25km, FLX(50)_25km, CTL_10km and FLX(50)_10km run.

The regional-mean heat fluxes bias in the four experiments is shown in Figure 2.7. The large positive downward LHF exhibits a persistent decrease by 15.76, 10.18 and 21.95 W/m^2 in the experiments of FLX(50)_25km, CTL_10km and FLX(50)_10km, respectively, compared with CTL_25km. The reduction of positive bias in the LWR is mainly contributed by enhanced resolution while that in SHF is primarily affected by flux adjustment. The negative bias in the shortwave radiation becomes larger with flux adjustment scheme activated, contributing to the negative bias in the NHF. The negative bias of SWR is reduced by 6.59 W/m^2 in the FLX(50)_25km

compared with CTL_25km, which is closely associated with the simulation in cloud cover (Dai et al., 2018). Following the warming of SST by the flux adjustment effect, the convection increases and subsequently induces excessive cloudiness, which blocks the net shortwave radiation to reach the ocean surface. The total cloud cover (TCC) is increased by 1.66% in the FLX(50)_25km compared with CTL_25km(Figure 2.8(a-b)).

Increasing resolution exhibits slight reduction of the biases in all the heat fluxes. Compared with the CTL_25km experiment, larger decrease in the bias is found in the shortwave radiation and latent heat flux, with large bias reduced by 7.61 W/m^2 and 10.18 W/m^2 in the CTL_10km, respectively (Figure 2.7). The TCC is decreased by 1.99% in the CTL_10km (Figure 2.8(c)), which allows more shortwave radiation to reach into the ocean surface. The SCC (RMSE) in the CTL_10km and CTL_25km are 0.91(6.70%) and 0.94(4.95%), respectively.

It is noted that there are some inconsistencies between SST bias and the heat flux bias. Cold SST bias is corresponding to the positive net heat flux, implying that the cold SST bias over this region is not due to the bias in the net heat flux. Instead, the ocean dynamics plays an important role in inducing the cold SST bias, which will be analyzed in next section. The main components contributing to the positive net surface heat flux biases are latent heat flux and longwave radiation. Although largest negative bias occurred in the SWR, the summation of positive LHF and LWR exceeds the negative bias in SWR, which consequently leads to the negative bias in NHF.

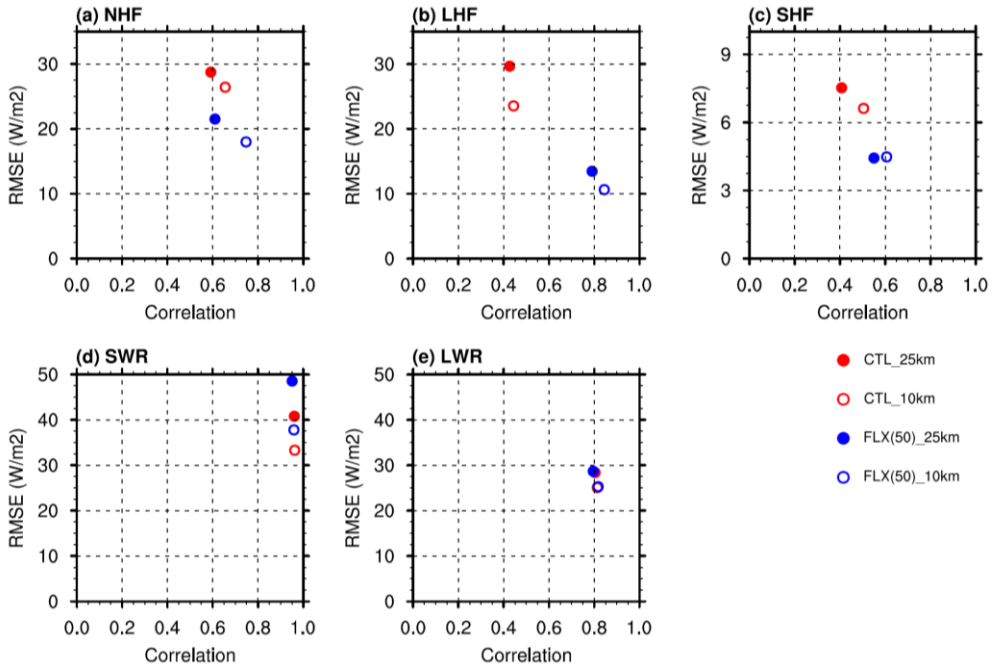

Figure 2.6 Scatter plots of spatial correlation coefficient and root mean square error (RMSE, unit: W/m^2) for (a) surface net heat flux(NHF), (b) latent heat flux(LHF), (c) sensible heat flux(SHF), (d) shortwave radiation(SWR) and (e) longwave radiation(LWR) during May-August 2006.

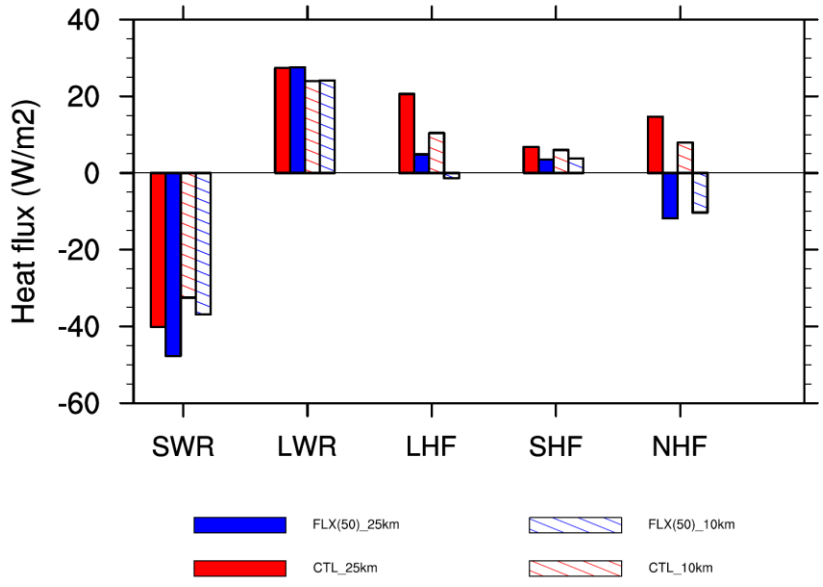

Figure 2.7 Regional-averaged bias (model minus observation) in net shortwave radiation (SWR), longwave radiation (LWR), latent heat flux (LHF), sensible heat flux (SHF) and net surface heat flux (NHF) in four experiments during May-August 2006. (Positive sign denotes that the heat flux is downward into the ocean, unit: W/m^2)

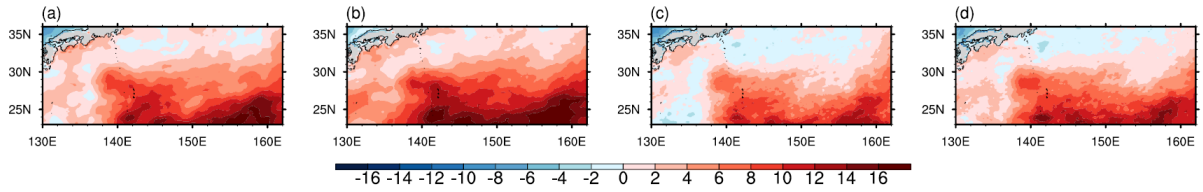

Figure 2.8 Spatial pattern of bias in MJJA total cloud cover (unit : %) between the experiment of (a) CTL_25km, (b) FLX(50)_25km, (c) CTL_10km and (d) FLX(50)_10km and the observation (model minus observation).

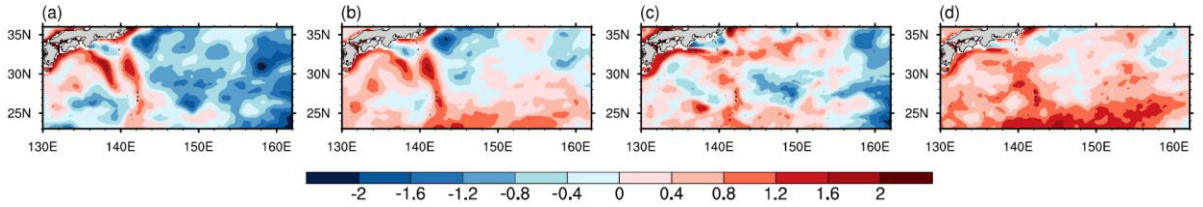

Figure 2.9 Spatial pattern of difference in MJJA air-sea specific humidity difference (unit : g/kg) between the experiment of (a) CTL_25km, (b) FLX(50)_25km, (c) CTL_10km and (d) FLX(50)_10km and the observation (model minus observation).

2.3.3 Near-surface wind

The above subsections show that cooler SST bias is remarkably reduced followed by the surface heat fluxes variation under the impact of flux adjustment and increasing resolution. The SST variation also causes notable change in the near-surface atmospheric variables through air-sea exchange. The response of near-surface wind to the two methods is provided in this subsection.

Figure 2.10 shows the SCC and relative RMSE for wind stress, 10-meter wind speed, 10-meter zonal and meridional wind for different experiments. Compared with CTL_25km, the pattern correlation coefficient for the 10-meter wind speed (wind stress) is increased by 0.25(0.04), 0.03(0.01) and 0.27(0.09) in the FLX(50)_25km, CTL_10km and FLX(50)_10km, respectively. Correspondingly, the relative RMSE for 10-meter wind speed (wind stress) is reduced by 6.24% (7.03%), 0.08% (0.33%) and 5.93% (9.11%) in the FLX(50)_25km, CTL_10km and FLX(50)_10km, respectively. It indicates that flux adjustment has larger impacts on the near-surface wind. Increasing model resolution alone (e.g., compared CTL_25km with CTL_10km) has a smaller impact on the near-surface wind. Flux adjustment largely reduces the relative RMSE in the meridional wind, which contributes to the improved 10-meter wind speed. The relative RMSE

for meridional wind (zonal wind) are 59.32% (51.67%), 45.16% (53.73%), 60.09% (51.91%) and 46.25% (48.35%) in the experiments of CTL_25km, FLX(50)_25km, CTL_10km and FLX(50)_10km, respectively. The remarkable improvement in the latent heat flux simulation (Figure 2.6) is associated with the improved near-surface wind speed.

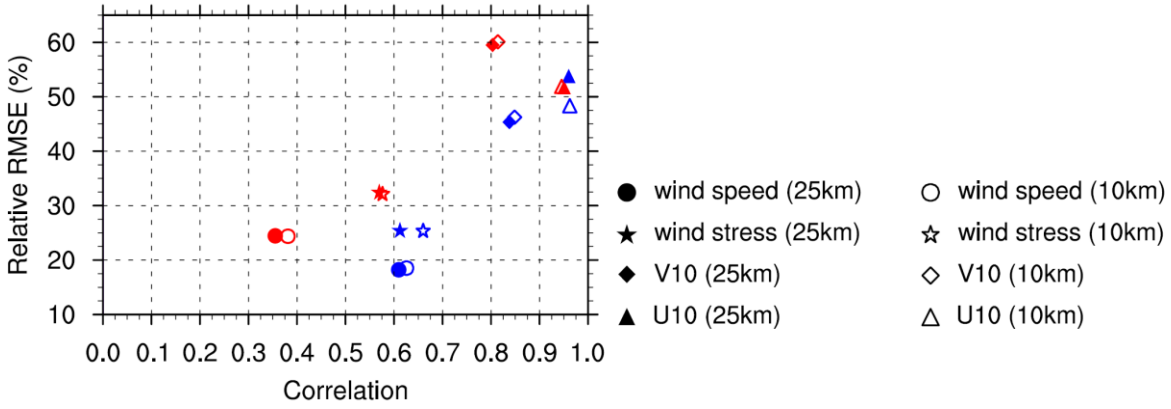

Figure 2.10 Scatter plots of spatial correlation coefficient (x-axis) and relative RMSE (y-axis) for 10-meter zonal wind, 10-meter meridional wind, 10-meter wind speed and wind stress magnitude. (Red and blue markers are for the experiments without and with flux adjustment (i.e., dQdSST = -50 W/m^2/°C), respectively; the solid (hollow) marker represents 25-km (10-km) resolution experiments)

2.4 Impacts on ocean state simulation

2.4.1 Ocean temperature and salinity

Figure 2.11 illustrates the vertical profiles of the SCC and RMSE of ocean temperature and salinity for four experiments. Both increasing resolution and flux adjustment offer positive impacts on the vertical distribution of ocean temperature and salinity. The maximum RMSE of temperature occurs at a depth of approximately 50 and 400 meters in all experiments. The temperature is slightly improved in the top 700 meters by the effect of flux adjustment. In the finer-grid experiments (i.e., CTL_10km, FLX(50)_10km), the improvement is much more substantial throughout the whole ocean layers, with maximum increase of SCC in temperature (salinity) by around 0.3 (0.15). The large RMSE of temperature and salinity in the thermocline are greatly reduced (Figure 2.11(c-d)). Adoption of flux adjustment scheme alone has smaller effects on the oceanic variables. When flux adjustment and increasing resolution are combined, the largest improvement in temperature and salinity in the top 600 meters could be obtained with main contribution from increasing resolution. The SCC (RMSE) for temperature and salinity at a depth of approximately 50 meters is increased

(reduced) by 0.1(0.69°C) and 0.2 (0.04 PSU) in the FLX(50)_10km experiment compared with CTL_25km. It is noted that flux adjustment produces larger positive effects on temperature and salinity at depths of 200-700 meters when the simulations are conducted with 25-km resolution. The effect of flux adjustment on the model skill in temperature and salinity is less apparent when the horizontal resolution is enhanced.

The improvements of ocean temperature and salinity vary among latitudes and depths (Figure 2.12(a-d) and Figure 2.12(f-i)). In observation, a remarkable thermocline tilt is located over a latitude range of 32°N and 36°N with the temperature decreased rapidly downward. The largest negative bias in ocean temperature occurs in the top 700 meters at the latitude of around 32°N (Figure 2.10(a)) and is substantially alleviated by the impacts of the two methods, which further favors the improved ocean salinity. Specially, the positive impacts of increasing resolution on the temperature and salinity simulation are much more evident. The experiments with 10-km resolution (i.e., CTL_10km, FLX(50)_10km) exhibit much more substantial reduction of bias by comparison with the corresponding runs at a coarser resolution of 25-km. The coldest temperature bias at a depth of 400 meters at latitude 32°N has a reduction of around 2°C in the CTL_10km compared with CTL_25km. The depth-cross profiles of temperature and salinity are shown in Figure 2.12(e) and Figure 2.12(j). There are persistent negative bias in the top 1000 meters, with largest negative bias of -1.41 °C at a depth of 35 meters. This maximum negative bias is reduced by around 0.63°C, 0.36°C and 0.84°C in the FLX(50)_25km, CTL_10km and FLX(50)_10km run, respectively. The vertical distribution of salinity bias exhibits opposite distribution at depths of 100-600 meters and below 600 meters. The positive bias occurs at depths 100-600 meters while the negative bias at depths below 600 meters. The pronounced negative (positive) bias is reduced by 0.05 PSU (0.04 PSU) at a depth of around 275(735) meters in the experiment of FLX(50)_10km compared with the CTL_25km. It should be noted that the high salinity bias in the top 100 meters is reduced accompanying with the warming of ocean temperature.

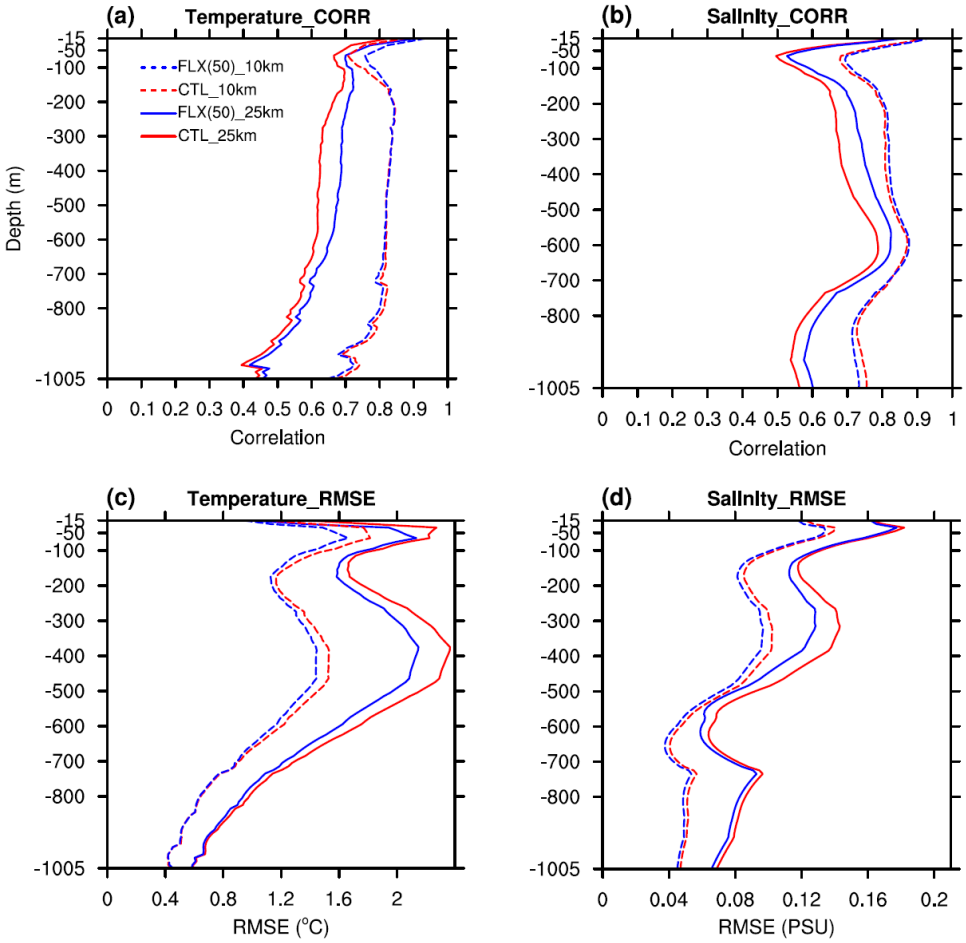

Figure 2.11 Vertical profiles of (a-b) spatial correlation coefficient and (c-d) RMSE for the regional-averaged temperature (left column) and salinity (right column) at depths of 15-1005 meters in the experiments of CTL_25km (red solid line), CTL_10km (red dash line), FLX(50)_25km (blue solid line) and FLX(50)_10km (blue dash line) during MJJA 2006. (The X-axis indicates the value of spatial correlation coefficient; the Y-axis indicates the depths)

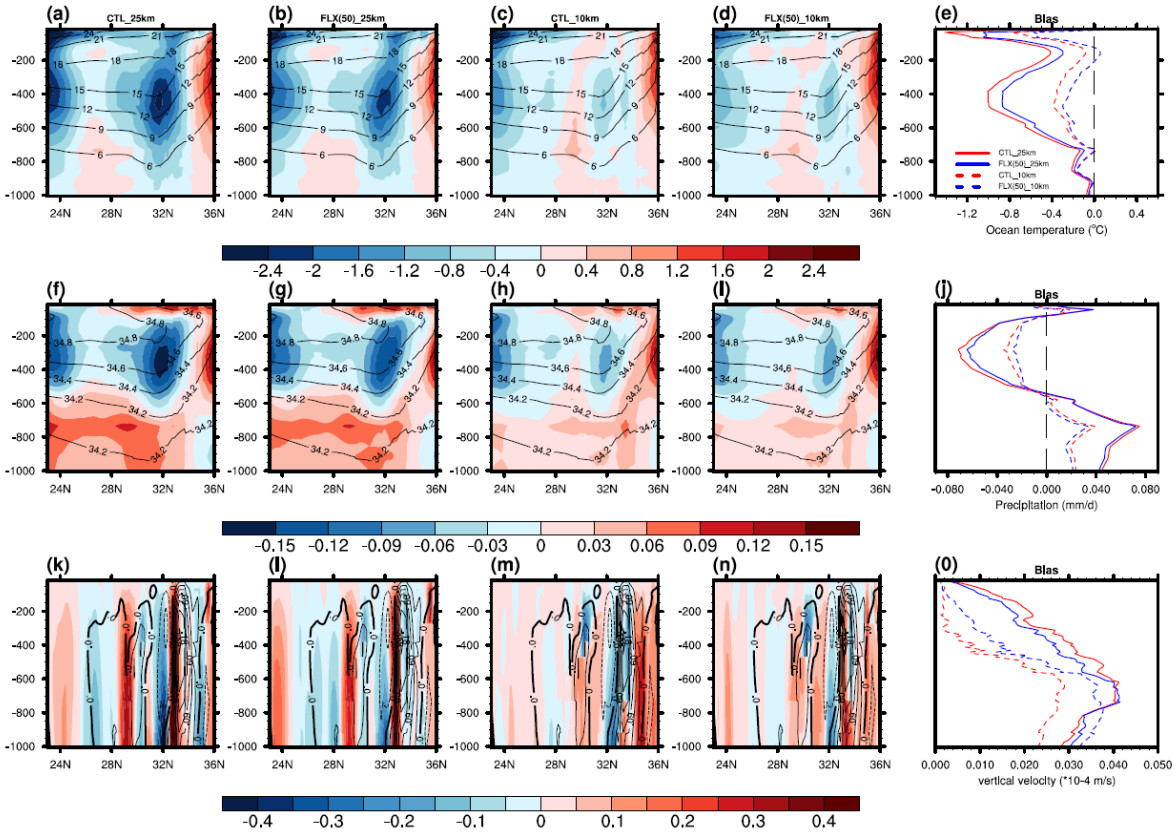

Figure 2.12 Depth-latitude cross section of zonally averaged (130°-162°E) bias (model minus observation) in the ocean temperature (unit: °C) for the experiments of (a) CTL_25km, (b) FLX(50)_25km, (c) CTL_10km and (d) FLX(50)_10km compared with the SODA dataset during MJJA (Contour lines in (a-d) indicate the observation results), and (e) vertical profile of bias in regional average ocean temperature for the four experiments in the top 1000 meters (Y-axis).

The middle panel (f-j) is for the salinity (unit: PSU).

The lower panel (k-o) is for the vertical velocity (unit: $\times 10^{-4}$ m/s).

2.4.2 Ocean currents

The Kuroshio Current which flows northeastward near Japanese coast is crucial in maintaining and changing the global climate. The ocean currents affect the ocean temperature through horizontal advection and vertical mixing. Some previous studies revealed that the Kuroshio Current path could cause significant atmospheric effects due to SST variation (e.g., Xu et al., 2010). Thus, accurate reproduction of the Kuroshio Current path has been a great concern for the climate oceanographers.

Figure 2.13 shows the spatial distribution of sea surface height (SSH) and ocean currents at a depth of 15 meters for the four experiments and observation. The 110-cm SSH contour can be used as a good indicator for the Kuroshio Extension axis. In observation, the 110-cm SSH contour is located at the maximum meridional gradient of SSH (Figure 2.13(e)). The Kuroshio Current is observed to closely follow an offshore non-large-meander path. A strong anticyclonic circulation (centered at 31°N, 136°E) is located at the South coast of Japan accompanying with high SSH center. Increasing resolution greatly improves the ocean current simulation. In particular, the finer resolution could accurately capture the observed non-large-meander path of the Kuroshio during MJJA (Figure 2.13(c-d)). However, An unrealistic larger meander path extending southward to around 28°N is produced at a coarser resolution (i.e., CTL_25km, FLX(50)_25km)[Figure 2.11(a-b)]. The 25-km resolution runs produce much stronger cyclonic eddies (centered at 32.5°N, 138°E) with a wider spatial coverage off Southeast coast of Japan. This misrepresented stronger cyclonic eddy accompanying with strong upwelling brings cold water to the ocean surface and leads to the cooler SST (Xu et al., 2010), which can be seen in Figure 2.13(a-b). However, very small differences in the Kuroshio Current path are detected between the experiments with and without flux adjustment (e.g., compared FLX(50)_25km with CTL_25km).

It is found that the interaction between the Kuroshio and the anticyclonic eddy triggers the occurrence of the offshore Nonlarge meander. The realistic simulation of Kuroshio Current path variation highly depends on the model capabilities in capturing the mesoscale eddies activities (Miyazawa et al., 2004). Figure 2.14 illustrates the surface relative vorticity for model simulations and observation in June 2006. In the 10-km resolution run, the mesoscale eddies (with 100-300km scales) and filamental structures (several 10km) in the Kuroshio Current could be better resolved (Figure 2.14(b)). In particular, the strong mesoscale anticyclonic eddies (centered at the [31°N, 137°E]) in the subtropical frontal region favour the formation of the Non-large meander path, which is better reproduced in the 10-km resolution run. And the better representation of the mesoscale eddies in the finer run also helps to regulate the Kuroshio Extension path.

The latitude-depth distribution of bias in the vertical velocity for four experiments is shown in Figure 2.12(k-0). In observation, strong upwelling (downwelling) occurs at a latitude of around 33°N (31°N), which is accompanied by the larger cyclonic (anticyclonic) eddy near the Kuroshio Current path in Figure 2.13. The intensity of the stronger upwelling and downwelling intensified compared with observation in the experiments with 25-km resolution (i.e., CTL_25km, FLX(50)_25km). In particular, the upwelling is most intense at the latitude of 32 °N, which leads to the coldest sea surface temperature. However, increasing resolution (i.e., CTL_10km, FLX(50)_10km) could effectively alleviate the unrealistic strong vertical motion. The strong upwelling averaged over the region is significantly alleviated in the finer resolution runs (e.g., compared CTL_10km with CTL_25km), which facilitates less cooler water brought from the deep ocean to the ocean surface and warms the SST. As seen from the spatial distribution of bias in vertical velocity for the CTL_25km and CTL_10km run, either positive or negative vertical velocity bias along the Kuroshio Current Path South of Japan in the coarser run is well resolved in the finer run. The wind stress curl is supposed be the major contributor for the reduction in upwelling motion in the upper ocean at the latitude of 32°N. In the 25-km resolution run, the prominent positive wind stress curl bias in the Kuroshio coastal region offshore (extending from 130°E to 145°E) induces surface divergence, forcing upward movement of water, and results in the upwelling through Ekman pumping (Figure 2.12(k) and Figure 2.16(a)). In the 10-km resolution run, the strong offshore upwelling is greatly reduced (Figure 2.15(b-c)) accompanied with the reduced positive wind stress curl bias (Figure 2.16(b-c)), especially within the latitudes between 31.5 °N~32.5 °N, which consequently leads to the alleviation of cold SST bias. The SCC (RMSE) are 0.13(1.50×10^{-7} N/m^3) and 0.11(1.99×10^{-7} N/m^3) in the experiment of EXP_25km and EXP_10km.

In general, increasing horizontal resolution better captures the vertical motions over the Kuroshio Current region while flux adjustment exhibits a minor impact.

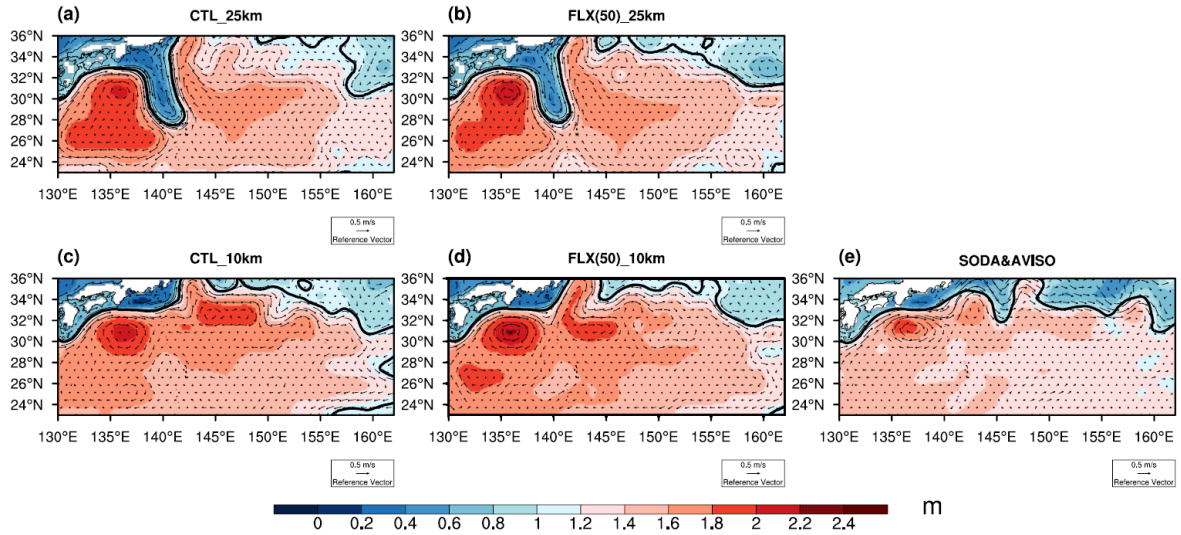

Figure 2.13 Spatial distribution of sea surface height (color shading; unit: meter) and ocean current (unit: m/s) at a depth of 15 meters in the experiment of (a) CTL_25km, (b) FLX(50)_25km, (c) CTL_10km , (d) FLX(50)_10km and (e) observation during MJJA 2006. (The thick black line is the 110-cm sea surface height, which represents the Kuroshio Extension axis)

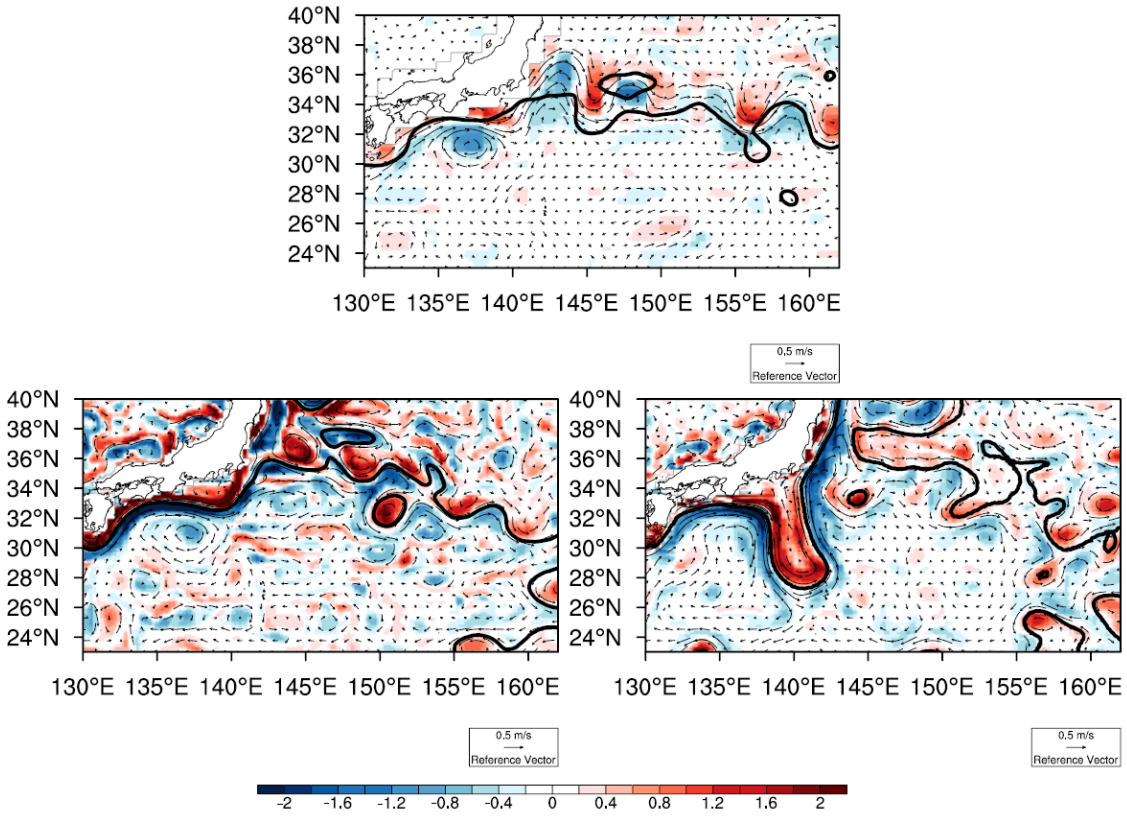

Figure 2.14 Spatial distribution of relative vorticity (color shading, unit: × 10^{-5} s-1) and ocean current (unit: m/s) at a depth of 15 meters in the experiment of (a) observation, (b) CTL_10km and (c) CTL_25km in June 2006. (The thick black line is the 110-cm sea surface height, which represents the Kuroshio Extension axis)

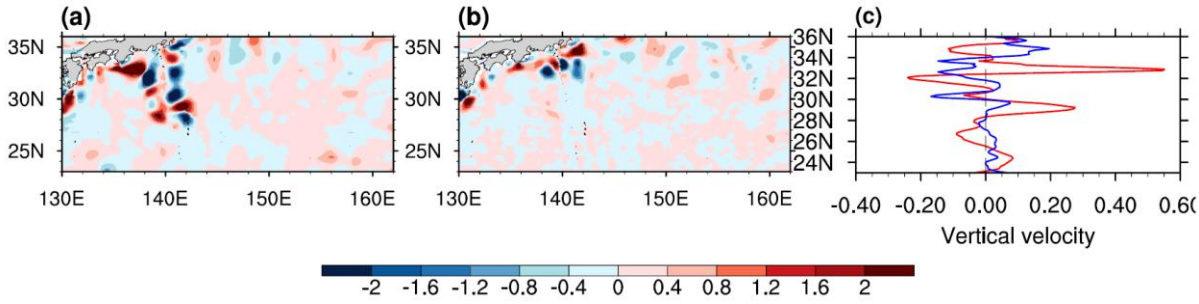

Figure 2.15 Spatial distribution of difference (model minus observation) in MJJA vertical velocity (unit: × 10^{-4} m/s) in the top 30 meters between the experiments of (a) CTL_25km and (b) CTL_10km and observation and (c) latitude cross section of zonally averaged (130°-162°E) vertical velocity bias in the experiments.

(red solid line indicates CTL_25km, blue solid line indicates CTL_10km)

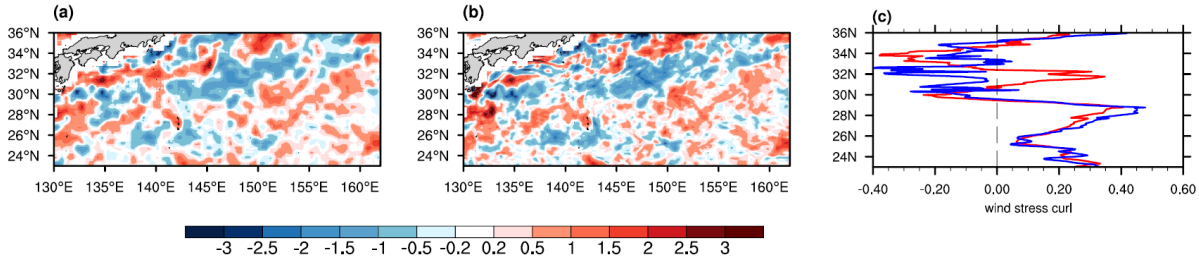

Figure 2.16 Same as Figure 2.15, but for wind stress curl (unit: ×10^{-7} N/m^3).

2.4.3 Sea surface height, mixed layer depth and ocean heat content

The change in SST is always accompanied with the response of ocean thermodynamics. The sea surface height is an important indicator for some important global and regional scale climate phenomena that occur at the sea surface (e.g., El Niño and La Niña events). The pattern distribution of bias in sea surface height for four experiment and the corresponding latitudinal distribution are shown in Figure 2.17. It is found that there are some inconsistencies between SST bias and SSH bias. The positive sea surface height anomalies over most of oceanic region correspond to the negative SST bias in the CTL_25km run (Figure 2.4(a) and Figure 2.17(a)), which is contrary to the previous study that shows there are large positive correlation between the SST and sea surface height in the subtropical front zones (Qiu et al., 2015). Following the warming of SST in the finer run, the sea surface height is slightly increased (Figure 2.17(c-d)). In particular, there is large negative sea surface height over South of Japan at the longitude of around 140°E in the CTL_25km run (Figure 2.17(a)). Following the alleviation of warm SST bias, the negative sea surface height bias is also greatly reduced, which consequently contributed to the better simulated pattern distribution in finer run. The SCC (RMSE) in the experiment of CTL_25km, FLX(50)_25km, CTL_10km and FLX(50)_10km is 0.59(0.31 meters), 0.64(0.30 meters), 0.79(0.27 meters) and 0.81(0.28 meters). Although the RMSE does not exhibit large reduction, increasing horizontal resolution favours the better pattern distributions. The optimized simulation of SSH could be achieved when both the flux adjustment and finer resolution are adopted.

The change in SSH is attributed to the variation of oceanographic factors (e.g., ocean eddies, waves, atmospheric conditions). In particular, the mixed layer depth (MLD) plays a vital role in regulating the SSH variation. Typically, the deepening (shoaling) in mixed layer depth could induce a decrease (increase) in the sea surface height. The SCC (RMSE) in the experiment of CTL_25km, FLX(50)_25km, CTL_10km and FLX(50)_10km is 0.15(8.17 meters), 0.12(8.79 meters), 0.46(6.95 meters) and 0.39(7.65 meters). The deeper mixed layer depth over South of Kuroshio Current Path (around 140°E) shoals in the finer runs(Figure 2.18 (c-d)), which further results in the increased SSH (Figure 2.17(c-d)).

The sea surface height is closely associated with the thermal structure of the upper ocean. The ocean heat content (OHC) is one of the critical climatic parameters for atmospheric and oceanic studies. The better simulation in the upper-ocean heat content greatly facilitates the future projection of climate change. The positive (negative) SSH is consistent with more (less) upper OHC. The simulated and observed OHC are calculated based on equation 2.4. There is significant lower upper ocean heat content along the Kuroshio Current Path, which correspond to lower SSH in the CTL_25km run (Figure 2.19(a) and Figure 2.17(a)). When the horizontal resolution is

increased, following the increasing ocean temperature, the upper OHC is also enhanced accompanying with the increased SSH (Figure 2.17(c) and Figure 2.19(c)). The SCC (RMSE) in the experiment of CTL_25km, FLX(50)_25km, CTL_10km and FLX(50)_10km is 0.47(4.14×10^9 J/m^2) , 0.72 (3.77×10^9 J/m^2), 0.83 (2.80×10^9 J/m^2) and 0.84 (2.60×10^9 J/m^2). Noted that the most remarkable improvement in the above oceanographic parameters (i.e., SSH, MLD and OHC) could be found along the Kuroshio Current path at the latitude of around 32°N (Figure 2.17(e), Figure 2.18(e) and Figure 2.19(e)).

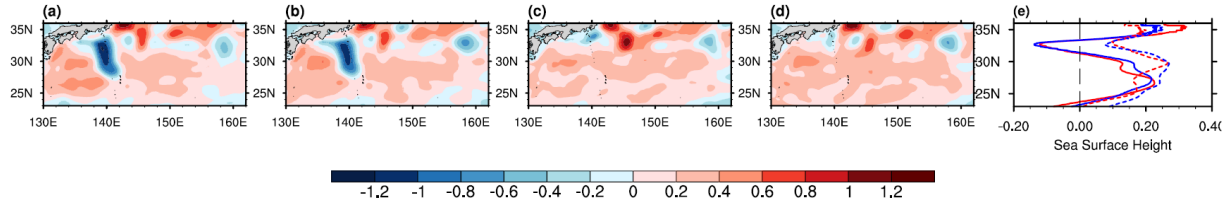

Figure 2.17 Spatial distribution of difference (model minus observation) in MJJA sea surface height (unit: meter) between the experiment of (a) CTL_25km, (b) FLX(50)_25km, (c) CTL_10km, (d) FLX(50)_10km and observation (model minus observation) and (e) latitude cross section of zonally averaged (130°-162°E) MJJA sea surface height bias for four experiments.

[red solid(dash) line indicates CTL_25km(CTL_10km); blue solid(dash) line indicates FLX(50)_25km(FLX(50)_10km)]

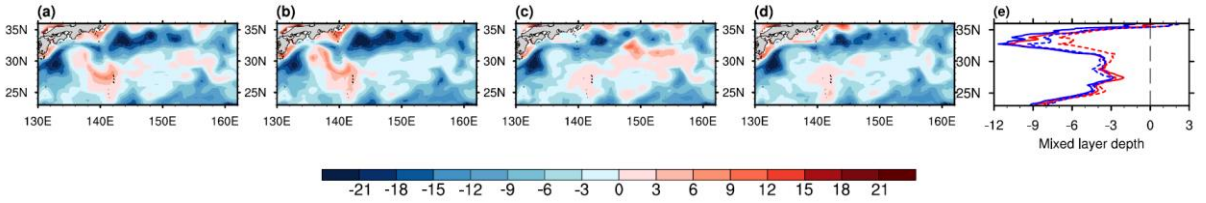

Figure 2.18 Same as Figure 2.17, but for mixed layer depth (unit: meter).

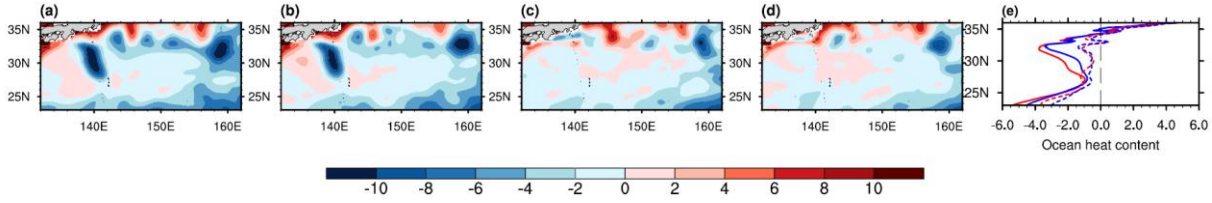

Figure 2.19 Same as Figure 2.17, but for ocean heat content (unit: $\times10^9$ J/m^2) in the top 500 meters.

2.5 Discussion

2.5.1 Space-time dependence of the methods

According to the results in section 2.3 and 2.4, neither flux adjustment nor increasing resolution could guarantee the improved simulation performance in all aspects. The limitations of flux adjustment in coupled modeling have been discussed in some studies (e.g., Pan et al., 2011; Ding et al., 2011; Dommenget and Rezny, 2018). It is not surprising that the model errors could not be corrected in all aspects by alleviating the temperature bias at the ocean surface alone. The bias in different model components and regions can be linked with each other as the climate system is strongly coupled. The non-linear effect of flux adjustment on modulating the internal modes of models is still not well understood. Based on a state-of-the-art global coupled model, Dommenget and Rezny (2018) show that flux adjustment does perform well in most, but not all aspects, which relies heavily on the kind of application the model is used for and on the objective of the application. In addition, a high-resolution coupled model could be useful for studying the oceanic climate, but they are still unable to outperform the coarse-resolution version in all aspects, which is also revealed in some studies (e.g., Akhtar et al., 2018).

First, the results in this study is based on simulation in the warmer season of one year. It is still unclear whether the effects of two methods vary both in space and time. We conducted two additional 1-year (i.e., 2006) sensitivity experiments at a resolution of 25-km over East Asia domain (10°S–50°N, 70°E–170°E) with and without flux adjustment, respectively. The flux-adjustment coefficient dQdSST is set to be constant value over SWNP in this study. Considering regional-dependence of the feedback between heat flux and SST, the dQdSST was estimated based on the formulation of Barnier et al (1995) and the climatological monthly mean values from NCEP reanalysis to maintain the observed climatology. The dQdSST value varies at temporal and spatial time scales. The results show that the prominent cold SST bias over Indian Ocean and Western Pacific Ocean could be alleviated by more than 1°C (figures not shown), indicative of the overall advantages of flux adjustment in the SST simulation over East Asia. However, the pattern correlation of precipitation during May-August slightly degraded over most of the sub-regions except the Oyashio Current Region. The additional results imply that there are still large uncertainties in the precipitation simulation due to the nonlinear effects which has not yet been fully understood. Thus, the application of flux adjustment should be carefully examined.

In terms of temporal-scale dependence of the two approaches, the systematic SST biases are contained in the climatology of RSM-ROMS (Ham et al., 2016), thus it is supposed that the improvement in SST simulation is also evident over long-term period. In section 2.3.1, the performance of precipitation during warmer season is slightly degraded in the flux-adjusted and

high-resolution experiments (Figure 2.3(b)). We also analyzed the results over other months to explore the features of seasonal dependence of precipitation simulation over SWNP. The results show that the pattern correlation (RMSE) of precipitation during these months (October – December) are 0.69(2.55), 0.74(1.90), 0.76(2.38) and 0.76(1.95) in the CTL_25km, FLX(50)_25km, CTL_10km and FLX(50)_10km runs, respectively (Figure 2.20). It implies that the effects of these two methods on the precipitation is seasonal and regional dependent. It is supposed that the negative effects of flux adjustment and finer resolution on precipitation in warmer season are caused by the physics parameterization schemes. Both enhanced model resolution and sustained parameterization development in individual sub-models are required to remove the precipitation bias (Zuidema et al., 2016). In general, it is necessary to conduct the experiments over long-term periods with same model setting to confirm the robustness of model climatologies.

In another aspect, the inclusion of flux adjustment does not necessarily lead to the improved net heat flux, no matter in the small domain (e.g., SWNP) or large domain (e.g., East Asia). The performance of the net heat flux simulation is closely associated with that of four heat flux components. It is noted that the bias magnitude of the net downward shortwave radiation is largest compared with three other heat flux components due to the overestimation of cloud cover, which has also been demonstrated in other studies based on RSM-ROMS (Li et al., 2012; Ham et al., 2016). The shortwave and cloud bias further enlarged with the flux adjustment scheme activated, suggesting that the deficiencies existing within the RSM-ROMS damp the positive effects of flux adjustment. Thus, some fundamental physics schemes (e.g., cloud parametrization and radiation scheme) should be improved to optimize the benefit of these two methods. In addition to the two convenient methods used in this study, other easy and effective solutions such as increasing vertical resolution are also applicable. The ocean temperature at top layer in RSM-ROMS is taken as SST. The thickness of uppermost ocean layer in RSM-ROMS over East Asia is around 10 meters, which might still not be sufficient to resolve the mesoscale oceanic features over the Kuroshio Current region. Thus, increasing vertical resolution of ocean component is a possibly effective method to remove the SST bias.

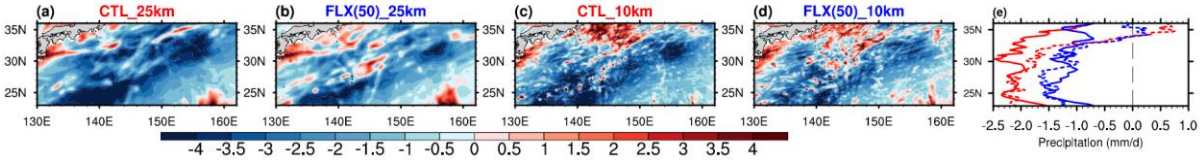

Figure 2.20 Same as Figure 2.4, but for the precipitation (unit : mm/day) during October-December in 2006.

2.5.2 Large meander Kuroshio path in 2004

It is revealed that the offshore non-large-meander path during MJJA is well produced in the finer resolution experiments (i.e., CTL_10km, FLX(50)_10km). The Kuroshio takes three typical paths, namely, the nearshore and offshore non-large-meander paths and the typical large-meander path (Kawabe 1995). It is found that the Kuroshio took a large meander path south of Japan for the first time in the summer of 2004 since 1991 (Xu et al., 2010). To explore the effects of finer horizontal resolution on other type of Kuroshio path, two additional experiments are conducted during May-September 2004 without the flux adjustment at a resolution of 10-km and 25-km, respectively. The results show that the observed large-meander path during August-September 2004 is also better captured in the 10-km resolution runs (Figure 2.21). However, the large-meander path persists for short period, then moves eastward and changes into offshore non-large meander path (Figure not shown). In the coarser resolution run, the Kuroshio Current path is misrepresented with unrealistic larger meander path extending excessively southward to the latitude of 28°N. Thus, the higher resolution does not necessary guarantee the accurate representation of the large meander Kuroshio path. Miyazawa et al. (2004) suggests that the mesoscale eddies produced by the flow instabilities have strong effects on the persistence of large-meander paths of the Kuroshio Current, which needs further detailed analysis.

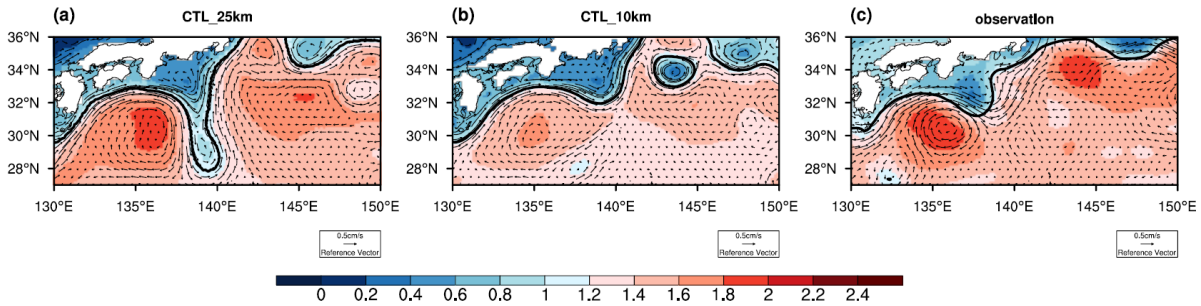

Figure 2.21 Spatial distribution of sea surface height (colour shading; unit: meter) in the experiment of (a) CTL_25km, (b) CTL_10km and (c) observation during August-September 2004. (The thick black line is the 110-cm sea surface height, which represents the Kuroshio Extension axis)

2.6 Summary

With the motivation to alleviate the cold SST bias over Subtropical Western North Pacific Ocean in an atmosphere-ocean coupled regional climate model RSM-ROMS, two conventional methods, flux adjustment and increasing horizontal resolution are employed to explore their impacts on the atmospheric and oceanic climate simulation during May-August of 2006 through several experiments.

All the experiments with flux adjustment and increasing resolution either individually or combinedly could effectively improve the SST simulation. Compared with the non-flux-adjusted experiments with 25-km resolution (i.e., CTL_25km), the cold SST bias over SWNP during MJJA could be reduced by 0.44 °C, 0.95 °C and 1.09 °C in the experiment of CTL_10km, FLX(50)_25km and FLX(50)_10km, respectively. The improved SST also leads to better performance in other climatic variables through air-sea feedback. The latent heat flux exhibits the most prominent improvement among all heat fluxes, which is primarily caused by the substantial decrease of large positive bias in the near-surface wind speed. The flux adjustment also has positive effects on the simulation of some oceanic variables. The biases in the ocean temperature and salinity in the top 700 meters are slightly alleviated. However, very small differences are detected in the simulation of ocean currents (e.g., upwelling and downwelling) when flux adjustment is activated. In contrast to the minor impact of flux adjustment, the benefit of enhanced horizontal resolution in the ocean state simulation is much more apparent. Both the ocean temperature and salinity are greatly improved with notable decrease (increase) of the RMSE (SCC) throughout the whole ocean layers. In particular, the non-large-meander path of the Kuroshio is better captured at a finer grid (i.e., 10-km) while unrealistic larger meander path is produced at 25-km resolution. In addition, the finer resolution also exerts slightly positive impacts on the simulation in most atmospheric variables (e.g., SST, all heat flux components). Figure 2.22 illustrates the spatial correlation coefficient between experiments and observation during MJJA for eighteen climatic variables including the upper ten atmospheric variables and lower seven oceanic variables. It gives a more complete picture to demonstrate the relative effects of flux adjustment and increasing resolution on the climate simulation. In general, flux adjustment appears to exhibit larger impacts on the atmospheric simulation while the benefit of increasing horizontal resolution is much more prominent on the ocean state simulation. The combined results for these experiments indicate that a better simulation of the climate over SWNP could be achieved through the application of small flux adjustment in parallel with increasing horizontal resolution.

Both of the two methods are useful approaches to remove the model SST bias. Nevertheless, the heat flux-adjusted and high-resolution version of RSM-ROMS is still deficient, which is unable

to outperform the non-flux-adjusted and coarse-resolution version in all aspects of the simulated climatology. The effects of these two methods are time and space dependent, which could give useful hints on the future application of coupled RCMs. The RSM-ROMS might exhibit better performance than reported here using improved physical schemes including the cloud scheme, radiation scheme and mixing scheme in the individual submodels. In addition, it is revealed that the upwelling motion is the primary reason for the colder SST bias from the preliminary analysis, the relative contribution needs to be quantified based on a mixed-layer heat budget analysis.

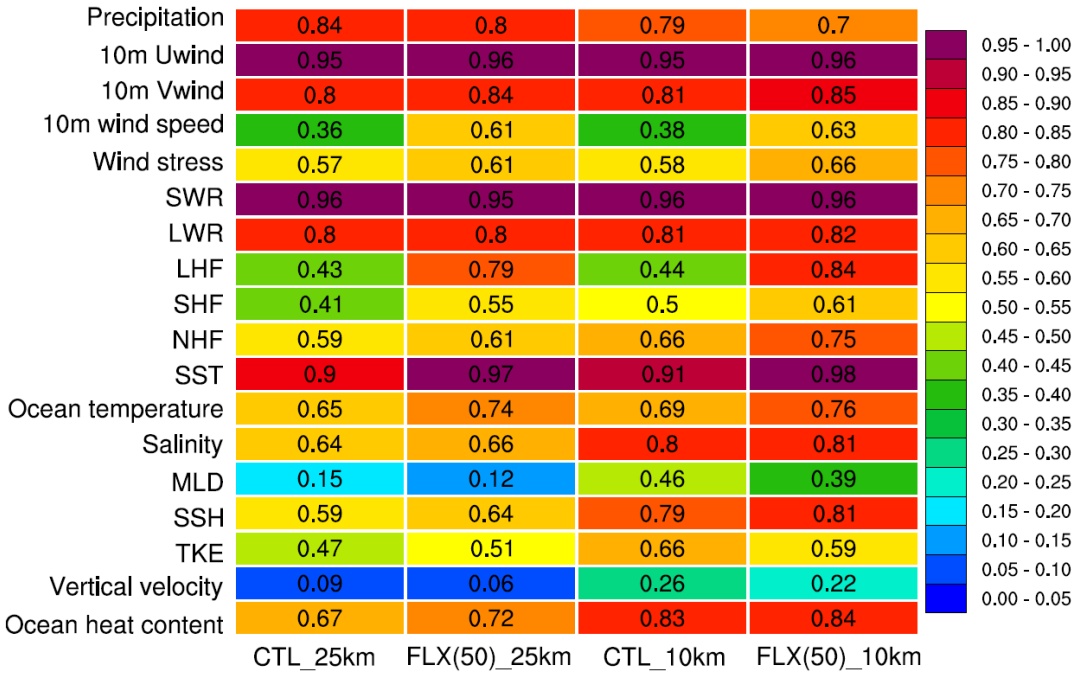

Figure 2.22 Portrait diagram display of spatial correlation metrics for the atmospheric and oceanic variables during MJJA 2006 between the experiments and observation.

(The x-axis shows the experiments; the y-axis shows different variables; each color represents specific range of pattern correlation, reddish color indicates higher correlation, bluish color indicates lower correlation; the values in each cell indicates the pattern correlation coefficient of one specific variable for a specific run)

(The total kinetic energy (TKE) of the ocean is calculated by this equation: $\mathrm{TKE} = \frac{1}{2}(u^2 + v^2)$; where u and v are zonal and meridional components of the geostrophic currents, respectively)

Chapter 3

Local intraseasonal air-sea interaction over East Asia

3.1 Introduction

There are multi-scale interactions (e.g., air-sea, air-land interaction) at various temporal and spatial scales in the climate system. Air-sea interaction is a major driver of the internal variability of climate system. The atmosphere and ocean interact through the exchange of heat, freshwater, momentum and energy at the air-sea interface, which is extremely essential for the occurrence of major climate phenomena. In particular, the intraseasonal oscillation (ISO) with periods of 10-90 days plays a crucial role in the modulation of global climate, which could bridge the gap between medium range and seasonal prediction and meet user demands. Thus, realistic simulation of air-sea interaction in the climate models is of essential significance, which allows for better prediction of future climate.

The intra-seasonal sea surface temperature fluctuation could be a potential predictor for the intraseasonal precipitation variation associated with strong MISO events (e.g., Zhang et al., 2019). Thus, the relationship between SST and precipitation could indicate the nature of local air-sea interactions, which is an important aspect in the measurement of model behaviors on the intraseasonal timescales (Wu and Kirtman, 2007). There are two types of SST-precipitation feedback mechanisms (i.e., positive feedback and negative feedback) in the climate system. The positive feedback (i.e., ocean forcing) indicates that the warming of SST could induce intense convective activities through triggering more water vapor over the ocean surface. The negative feedback (i.e., atmospheric forcing) indicates that strong convective event could reduce the downward surface shortwave radiation into the ocean surface through increasing the cloud fraction, which further cools the SST due to the cooling effect of cloud.

In recent decades, some previous studies have been carried out to demonstrate the ability of climate models to simulate the intraseasonal rainfall variability and the associated atmospheric features. Feng et al. (2018) demonstrated that the coupled climate reanalysis CERA-20C better captured the intraseasonal SST-precipitation relationship compared with the uncoupled reanalyses CERA-20C. Based on the monthly outputs from an AO coupled RCM, Wang et al.(2015) revealed that the coupled run could reproduce more realistic SST-rainfall correlation in Baltic Sea while the uncoupled atmosphere-standalone run produces a weak correlation. Umakanth and Kesarkar (2018) showed that the air-sea coupled RCM better represented the northwest-Southeast tilt of precipitation anomalies during active/break phase of Indian monsoon.

Northward propagation in boreal summer and eastward propagation in boreal winter are two distinguished features of tropical intraseasonal oscillation. Simulation of these two phenomena heavily relies on the interactive air-sea feedbacks. Peatman and Klingaman (2018) showed that air-sea coupling slightly improved some aspects of the northward propagation of boreal summer intraseasonal oscillation (BSISO) simulation over Indian Ocean, Bay of Bengal while degrades others. Based on the NCEP Climate Forecast System model CFSv2, Sharmila et al. (2013) suggested that air-sea interaction is beneficial to simulate the observed features (e.g., amplitude, periodicity, northward propagation) of monsoon ISO compared to the atmosphere-only model. The critical role of air-sea coupling in the simulation of Madden-Julian Oscillation is also revealed in previous studies using coupled GCMs (Klingaman and Woolnough, 2014; Shelly et al., 2014).

Most of works on the intraseasonal air-sea interaction analysis are based on either reanalysis (e.g., Feng et al., 2018) or global climate models with coarser resolution (e.g., Krajendran et al., 2012; Roxy et al., 2013). Nevertheless, there are still some limitations in the studies based on RCMs, such as narrow research domain, or using RCM with simple oceanic dynamic (e.g., Qian et al., 2012; Umakanth and Kesarkar, 2018). Rare of them use fully coupled regional climate model with dynamic and thermodynamic ocean coupling. In addition, although the advantages of air-sea coupling have been well revealed in previous studies, the results could be model dependent.

In this study, a fully coupled regional atmosphere-ocean model (RSM-ROMS) is used. Dai et al. (2018) demonstrated that the coupled model reproduces more realistic simulation of interannual and intraseasonal variation of East Asian summer monsoon, and improves the simulation of rainfall variability on both interannual and intraseasonal timescales. The coupled model could reproduce the observed SST-precipitation and SST-evaporation feedbacks. However, the analysis is based on the unfiltered dataset. Misra et al. (2018) show that the coupled model RSM-ROMS has excellent skills in capturing the intraseasonal variability over Indian Summer Monsoon region based on the 10-km resolution experiment. However, this study did not make comparison with the uncoupled model and only focused on the climate in Indian summer monsoon region. There is still no general and comprehensive assessments of air-sea interaction on the intraseasonal timescales. It is still not clear whether this coupled RCM has the ability to capture a realistic intraseasonal air-sea interaction over other ocean regions (e.g., Western Pacific).

The purpose of this study is to confirm the fidelity of fully coupled RCM (RSM-ROMS) in the simulation of intraseasonal variabilities and local intraseasonal air-sea interaction over East Asia. In this chapter, the key question to be addressed is how well the RSM-ROMS reproduces the local intraseasonal relationship between SST and precipitation and surface heat fluxes over East Asia in comparison with the uncoupled model.

3.2 Experiment, methodology and validation dataset

3.2.1 Experimental design

There are complex land-atmosphere-ocean interactions over East Asia summer monsoon region. Thus, the model experiments are conducted over the East Asia CORDEX domain (17.22 °S-59.50°N, 65.11°E - 174.89°E). The analyzed domain covers tropical and subtropical East Asia area (10°S-30°N, 70-170°E) as the intraseasonal air-sea interaction is more prominent South of 30°N (Figure 3.1).

Two sets of experiments are conducted at a horizontal resolution of 25-km using the coupled model RSM-ROMS and its atmosphere component RSM, respectively (Table 3.1). The atmospheric lateral forcing is same in these two runs (section 2.2.1 in chapter 2). The main difference between these two runs is the oceanic forcing. The uncoupled run is driven by the daily interpolated OISST dataset with the resolution of 1 degree. In the coupled run, the initial and boundary conditions are derived from monthly SODA reanalysis with a horizontal resolution of 0.5 degree. The SST is updated with the driving of heat fluxes every 24 hours.

The two runs are performed for the 1998-2008 period, and the first year (i.e., 1998) is discarded accounting for the sufficient spin-up time for the ocean. Thus, the local intraseasonal air-sea interaction is assessed using the ten-year (1999-2008) daily model outputs. Most of the analysis on this study focus on boreal summer.

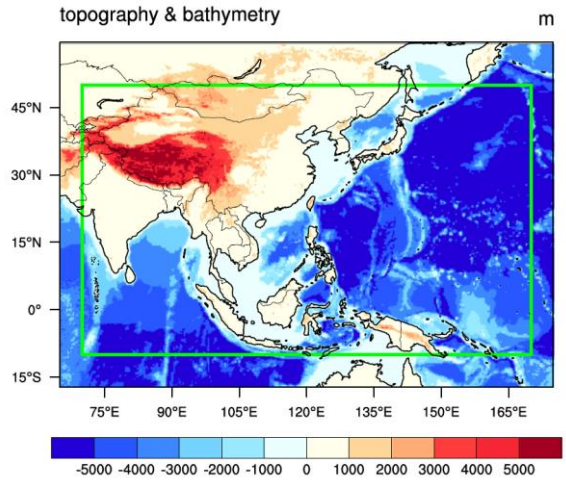

Figure 3.1 Simulation domain, model topography and bathymetry (unit: meter) from ETOPO5 for model simulation. The green box indicates the analyzed domain.

Table 3.1 List of experiments performed

Experiments Name	Model Components	Atmosphere Lateral Forcing	Ocean Lateral Forcing	Model Resolution	Simulation Period
Uncoupled (RSM)	Atmosphere	T62L28 6-hourly NCEP R2	Weekly Optimum Interpolated SST (OISST) from NOAA (daily interpolated, 1°×1°)	25km	01/01/1998~ 31/12/2008
Coupled (RSM-ROMS)	Coupled atmosphere-ocean		Initial and boundary conditions are from monthly 0.5°×0.5° Simplified Ocean Data Assimilation (SODA)		

3.2.2 Methodology and Validation dataset

Following the method of Feng et al.(2018), 10-year time series are filtered with 10-60-day butterworth bandpass filtering to isolate the intraseasonal signals. The temporal evolutions of SST with the timescales lower than 60 days in the uncoupled and coupled run are similar. Thus, the air-sea interaction on the timescales of 10-60 days tend to reflect the distinct difference between the two runs. Prior to the filtering, the climatological annual cycles during 1999-2008 are removed from the raw data. The temporal correlation coefficient and regression anomalies are employed to validate the model performance in simulation of air-sea interaction. The correlation and regression coefficients are calculated based on the Eq. 3.1 and Eq. 3.2, respectively:

$$Re_x = \frac{\sum(x_i-\bar{x})(SST_i-\overline{SST})}{\sum(SST_i-\overline{SST})^2} \qquad \textbf{(Eq. 3.1)}$$

$$Corr_x = \frac{\sum(x_i-\bar{x})(SST_i-\overline{SST})}{\sqrt{\sum(SST_i-\overline{SST})^2}\sqrt{\sum(x_i-\bar{x})^2}} \qquad \textbf{(Eq. 3.2)}$$

Here Re_x is the regression coefficient, $Corr_x$ is the temporal correlation coefficient, SST_i is the time series of SST, x_i is the time series of other atmospheric variable. The significance of the linear correlation coefficient and regression coefficient are estimated at the 90% significance level by employing the Student's t test. Following the method of Wu and You (2018), assuming that the

decorrelation time scale is 30 days, so there are 3 degrees during June-August per year and the total degree of freedom for 10-year data is 30.

To make comparison of the model simulation performances against the observation, several products are used in this study. Observed SST are obtained from the daily Optimum Interpolation Sea Surface Temperature (OISST) with a resolution of 1 degree. The precipitation is validated using the Tropical Rainfall Measuring Mission (TRMM) 3B42 version 7 daily data product (Huffman et al., 2007) at the spatial resolution of 0.25 degree and daily temporal resolution for the period of 1999-2008. The GPCP One-Degree Daily data (GPCP 1DD) Version 1.1 (Huffman et al., 2001) with a 1.0 degree grid spacing is used to guarantee the reliability. The OAFlux heat fluxes dataset (Yu and Weller, 2007) is found to exhibit the smallest difference with other flux dataset (He et al., 2017), thus it is used to validate the relationship between SST and heat fluxes in Chapter 3 and explore the contribution of surface heat fluxes to SST variation in Chapter 4. The sign of heat fluxes is positive for flux into the ocean. Net heat flux is obtained as follows: NHF = SWR+LWR+SHF+LHF, where SWR, LWR, SHF and LHF indicate the net surface shortwave radiation, net surface longwave radiation, latent heat flux and sensible heat flux, respectively. The radiation fluxes SWR and LWR are obtained from the difference of the downward minus upward radiation.

3.3 Intraseasonal precipitation variation

3.3.1 Spectrum analysis

To detect the predominant periodicity, power spectrum analysis is applied to the area-averaged rainfall anomaly time series. The statistically significant part of the mean power spectrum for 10 summers (JJA during 1999-2008) in observation is concentrated within the frequency band corresponding to 40-50 days which exceeds 95% significance level. The prominent bump in the observed spectral density between 40 and 50 days is also seen in the uncoupled and coupled runs (Figure 3.2(a) and Figure 3.2(b)). In general, the predominant period of summer precipitation is well captured by both models. It is noted that the amplitude of the power magnitude is slightly weaker in the coupled run.

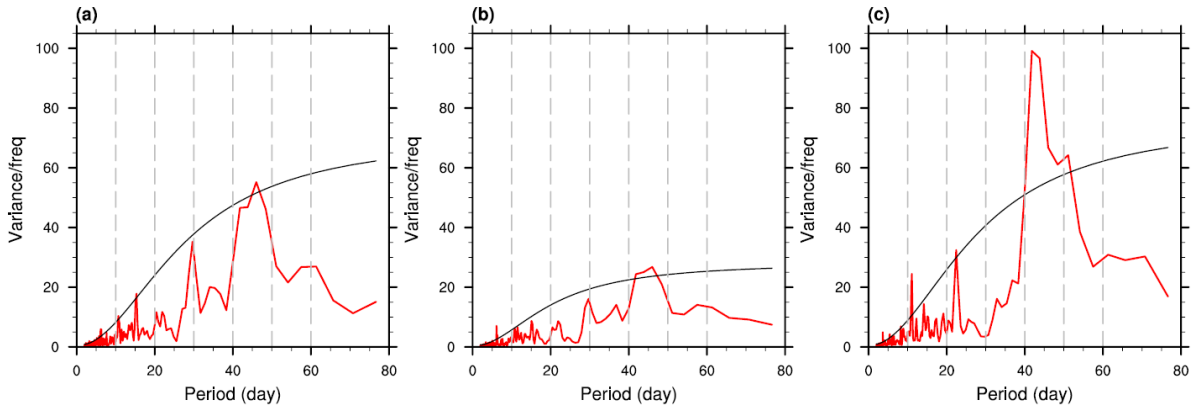

Figure 3.2 Mean power spectrum of unfiltered precipitation anomalies time series over East Asia (10°S-30°N, 70-170°E) during June-August (JJA) of 1999-2008. The black line indicates the 95% confidence level.

3.3.2 Spatial variation

The benefits of the coupled model in simulating the ISO have been revealed in some previous studies using different coupled models (e.g., Umakanth and Kesarkar, 2018). The intensity of monsoon intraseasonal variability could be indicated by the standard deviation of precipitation. Figure 3.3 shows the spatial distribution of standard deviation of intraseasonal precipitation during 1999-2008. In observation, there is strong intraseasonal variabilities over eastern coast of Arabian Sea, Bay of Bengal, Eastern Tropical Indian Ocean, South China Sea and Eastern Philippine Sea (Figure 3.3(c)). Both runs largely underestimate the intraseasonal variation over Bay of Bengal, South China Sea and Eastern Philippine Sea with much lower intraseasonal rainfall found in the couple run (Figure 3.3(a-b)). However, the coupled model could effectively alleviate the unrealistic large positive bias of intraseasonal precipitation over the Southern Tropical Indian Ocean and Subtropical Western Pacific (Figure 3.3(f-g)). The spatial correlation coefficient and RMSE for the coupled (uncoupled) experiment are 0.47(0.39) and 2.43(2.22) mm/day, respectively. Same analysis is repeated using the daily rainfall dataset from GPCP 1DD to confirm the robustness of the finding based on TRMM 3B42 dataset. The ISO estimated by the GPCP estimates is substantially lower than that by TRMM, especially over some oceanic region (e.g., Bay of Bengal, South China Sea, Eastern Philippine Sea) with the magnitude difference of around 3 mm/day (Figure 3.3(c-d)). It implies that there are still large uncertainties within the rainfall validation dataset. The statistical metrics of model performances in simulations of the intraseasonal precipitation are shown in Table 3.2. The coupled model still has better skills based on the GPCP daily rainfall, with the SCC and RMSE reaching around 0.43(0.39 mm/day) and 2.75 (1.52 mm/day)

in the coupled (uncoupled) run, respectively. Overall, the main conclusion of the study is not sensitive to the choice of validation dataset, RSM-ROMS provides a viable tool for understanding East Asian Monsoon.

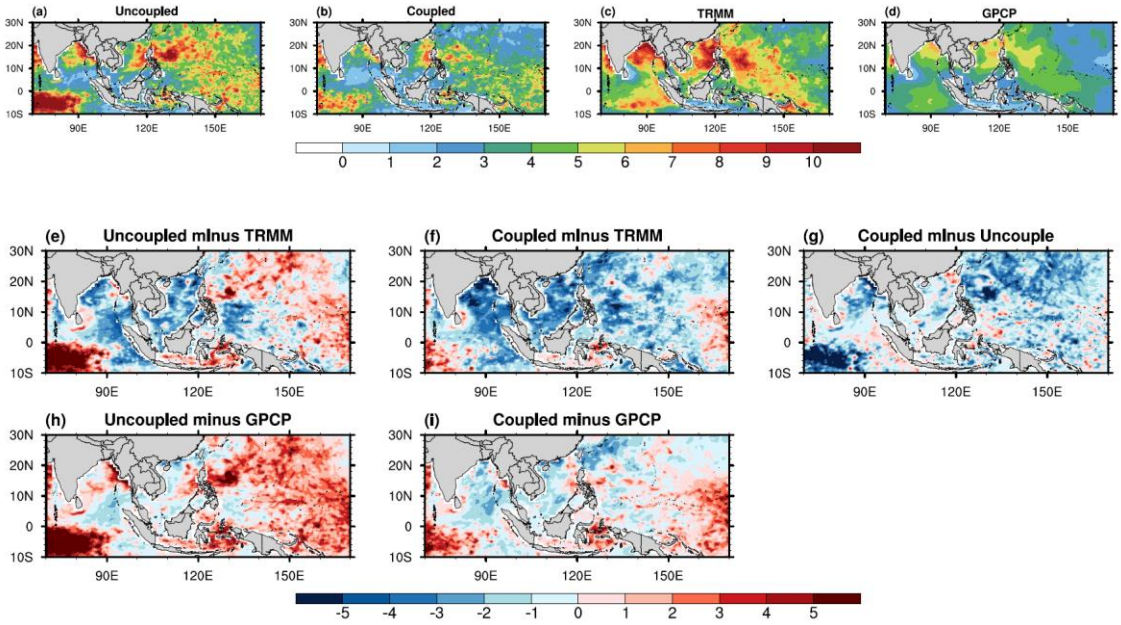

Figure 3.3 Standard deviation of JJA intraseasonal (10-60-day) precipitation(unit: mm/day) in the (a) uncoupled model, (b) coupled model, (c) TRMM_3B42 , (d) GPCP_1DD and (e) Uncoupled minus TRMM_3B42, (f) Coupled minus TRMM_3B42, (g) Coupled minus uncoupled run, (h) Uncoupled minus GPCP_1DD and (i) Coupled minus GPCP_1DD.

Table 3.2 Statistical performances of intraseasonal rainfall variabilities against TRMM and GPCP

Observation dataset	Model simulations	Spatial correlation	RMSE (mm/day)	Bias (mm/day)
TRMM	Coupled	**0.48**	**2.45**	**-0.08**
	Uncouple	0.40	2.22	-1.27
GPCP	Coupled	**0.42**	**1.54**	**0.22**
	Uncouple	0.40	2.77	1.57

3.4 Eastward and northward propagation of tropical intraseasonal oscillation

3.4.1 Eastward propagation

The Madden-Julian Oscillation (MJO) is the most dominant component of ISO during boreal winter, which is featured by the eastward movement trapped along the equator. The MJO is a coupled phenomenon, thus how well the coupled model could reproduce this tropical intraseasonal activity needs to be investigated. Figure 3.4 illustrates 30-day-lead-lag of the intraseasonal precipitation during boreal winter (November-April) for nine years. In observation, large precipitation appears at day 0 over Tropical Indian Ocean, and then propagates eastward to the Tropical Western Pacific Ocean after 30 days (Figure 3.4(c)). The direction of the propagating ISO in the tropical regions is well captured by the coupled model, but the amplitude is weaker compared with the observation, which is possibly caused by the weaker SST-precipitation in the coupled run (Figure 3.4(b)). In the uncoupled run, the eastward propagation ceases over the Eastern Indian Ocean and is misrepresented in the entire tropical regions (Figure 3.4(a)). The pattern correlation coefficient of the propagation pattern are 0.51 and 0.65 in the uncoupled and coupled run, respectively.

Take one strong MJO event (January 2001-March 2001) as an example, Figure 3.5 illustrates lag-longitude diagram of the intraseasonal rainfall anomalies during this strong MJO event. The heavy precipitation is observed to propagate from Tropical Indian Ocean to Central Pacific from January 15th to the end of February. In the coupled run, the features of eastward propagation are well captured. The remarkable improved intensity and direction is detected along the longitude between 140-170°E. In the uncoupled run, the eastward propagation weakens and stops at the longitude of 140°E. The pattern correlation with observations is around 0.21(0.02) in coupled (uncoupled) run, suggesting that this improvement is mainly due to the effect of air-sea coupling (e.g., more realistic phase relationship between SST and convection). The eastward propagating features also tend to be better captured for other strong MJO events (Table 3.3). It is noted that there is weaker amplitude of ISO between the longitudes of 90°E-130°E in the coupled run comparing with observation and uncoupled one, which might be caused by the mean state bias in coupled model. It is suggested that the degradation of mean-state SST errors could lead to a compensating effect of the improvement from air-sea coupling (Klingaman and Woolnough, 2014). The role of mean state bias and air-sea coupling in the simulation of eastward propagation should be separated by conducting additional experiments.

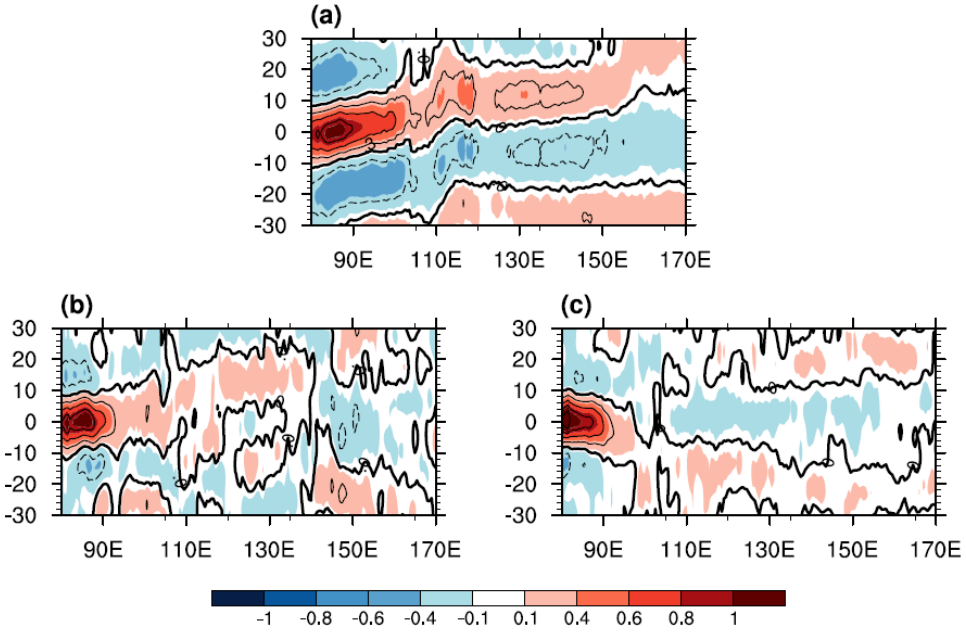

Figure 3.4 Lag-longitude diagram of regressed anomalies of intraseasonal(10-60-day) rainfall averaged over 10°S-10°N in the (a) observation, (b) coupled run and (c) uncoupled run during November-April (NDJFM) for nine years (November 1999-April 2008).

The filtered rainfall anomalies averaged over the Tropical Indian Ocean (10°S-10°N, 80-90°E) are used as the reference time series to compute the regression.

(The x-axis indicates the longitudes; the y-axis indicates the lead-lag day)

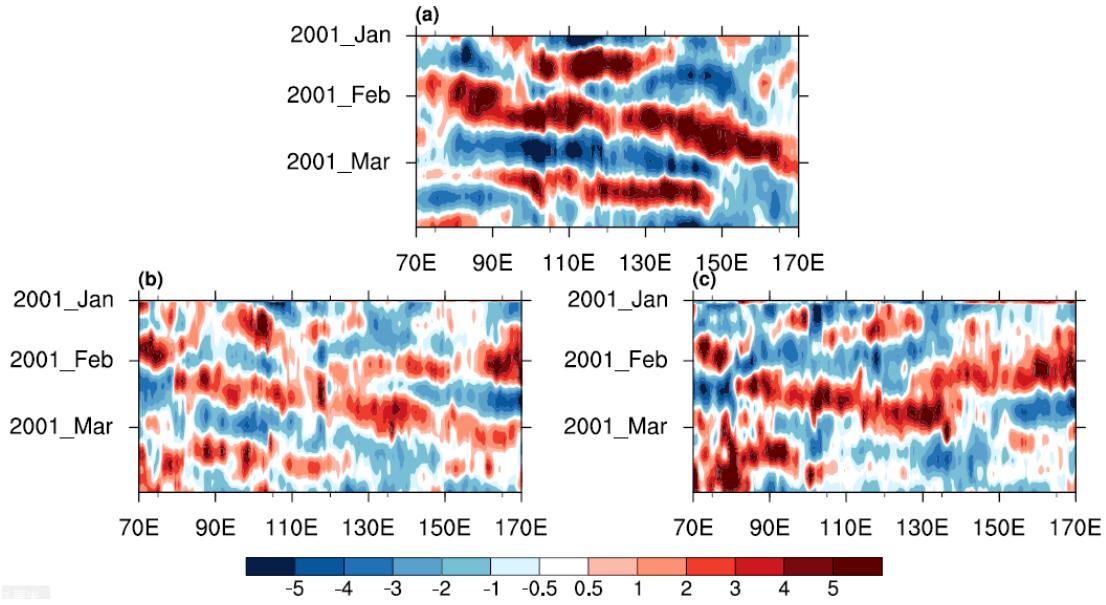

Figure 3.5 Time-longitude (10°S-10°N) diagram of intraseasonal (10-60-day) precipitation anomalies in the (a) observation, (b) coupled run and (c) uncoupled run during January-March 2001.

Table 3.3 Spatial correlation coefficient for lead-lag precipitation between the uncoupled, coupled run and observation for several strong MJO events.

MJO events		Model simulation	
		Uncoupled	Coupled
No.1	November 2000~December 2000	0.05	**0.11**
No.2	January 2001~March 2001	0.02	**0.21**
No.3	October 2002~ December 2002	0.43	**0.43**
No.4	June 2004 ~ July 2004	0.26	**0.37**
No.5	March 2005~ May 2005	0.16	**0.22**

3.4.2 Northward propagation

Northward-propagating intraseasonal oscillation is distinct during boreal summer monsoon season over Indian Ocean (IO) and western North Pacific (WNP). The intraseasonal precipitation anomalies could indicate the ISO activities. The 30-day lead-lag regression of zonal averaged intraseasonal precipitation anomalies with respect to the corresponding intraseasonal rainfall anomalies over Eastern Indian Ocean and Tropical Western Pacific is illustrated in Figure 3.6. In observation, the convection originates from near-equatorial areas and propagates northward to around 15°N about 10 days later before becoming weak at the head of Bay of Bengal (Figure 3.6(c)). There is also a southward branch which originates from near-equatorial regions. The northward branch could be captured in both experiment (Figure 3.6(b-c)). However, the northward propagation tends to decay faster at a latitude of around 20°N. The coupled model well captures the southward branch while the uncoupled one misrepresents it. Over Western Pacific, there is an observed intraseasonal variabilities propagating from Southern equatorial Western Pacific Ocean to Northern part (Figure 3.6(f)). The main difference between these two runs is the northward propagation originates from a latitude of 10°S to the equatorial region. The coupled run generates the realistic intensity and propagation speed while the uncoupled run produces a nearly standing propagation (Figure 3.6(d) and (e)).

In general, air-sea feedbacks is most beneficial to the simulation of ISO propagation in the near-equatorial areas while exhibits less effects on the northward propagation at the latitude north than 5°N. It is noted that the northward convection propagation in the uncoupled run still remains with slightly weaker intensity. Similar result is also revealed in some previous studies based on the global climate model (Peatman and Klingaman, 2018). Klingaman et al. (2008) shows that the

atmosphere-only model could capture the realistic intraseasonal variability if it is given by the accurate SST forcing with high temporal frequency. Gao et al. (2018) suggests that the air-sea feedbacks might account for 12-20% of the BSISO propagation while the atmospheric dynamics are responsible for the rest. The couple feedbacks are important but not necessary to the propagation of convection. It is supposed that an atmosphere-only model with a reasonable representation of atmospheric dynamics could capture the ISO propagation without the need of air-sea coupling.

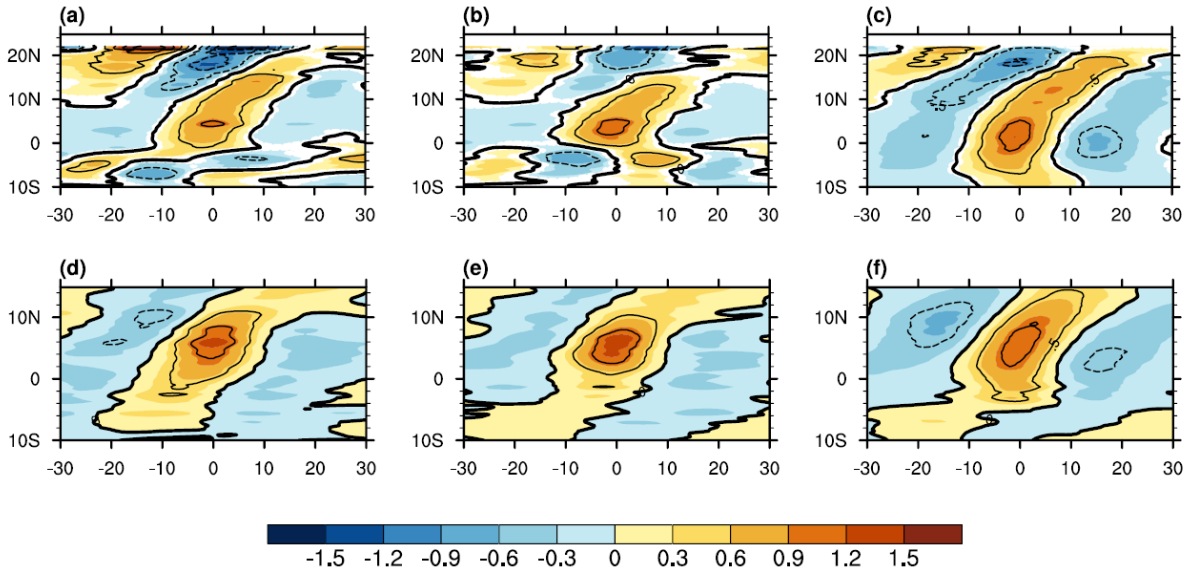

Figure 3.6 Regressed anomalies of zonally (75 - 90 °E) averaged intraseasonal (10-60-day) rainfall with respect to the intraseasonal rainfall over Tropical Eastern Indian Ocean (0-10°N, 75-90°E) (upper panels) in the (a) uncoupled run, (b) coupled run and (c) observation during May-September.

Lower panel is same as the upper panel, but for the zonally (130-150°E) averaged intraseasonal rainfall with respect to the intraseasonal rainfall over Tropical Western Pacific (0-10°N, 130-150°E).

(The x-axis represents the lagging day, and the y-axis represents the latitude)

3.5 Relationship between sea surface temperature and precipitation

3.5.1 Spatial variability

The simultaneous local SST-precipitation relationships for model simulations and observation during summer (June-August) 1999-2008 is shown in Figure 3.7. In observation, the negative correlation with a statistically significant test at 90% occurs in most oceanic region especially over Tropical Indian Ocean and Northwest Pacific, signifying the dominance of atmospheric forcing. There is a small-scale significant positive feedback over southern South China Sea and Northern Tropical Indian Ocean, indicative of the dominance of ocean forcing (Figure 3.7(a)).

The coupled model accurately reproduces the corresponding negative correlation (Figure 3.7(b)), particularly over Northwest Pacific Ocean, which agrees well with the result in Dai et al.(2018) based on the unfiltered precipitation and SST dataset. Slight difference is detected over the ocean region southeast of Japan where there is large negative feedback in our result while positive feedback in Dai et al.(2018). It is possibly caused by the feedback on the intraseasonal timescales and the period of dataset. The simulated negative feedback in the coupled run is slightly weaker over Tropical Western Pacific compared with the observation. The uncoupled model forced by the prescribed SST reproduces the unrealistic positive statistically significant positive feedback (i.e., dominance of ocean forcing) over tropical western Pacific region and central Indian Ocean, head of Bay of Bengal due to lack of atmospheric feedbacks on the ocean(Figure 3.7(c)).

It is observed that the negative feedback prevails over Eastern Indian Ocean with correlation larger than 0.5. However, unlike western Pacific Ocean, coupled model cannot produce the strong strength of air-sea interaction over Indian Ocean. The uncoupled simulation cannot reproduce the feedback when the strong atmospheric forcing is dominant while it tends to capture the feedback when the atmosphere responds to the oceanic forcing passively. This similar features in the uncoupled simulation could also be found in the atmospheric global circulation model (AGCM) (Wu and Kirtman, 2007).

When the precipitation anomalies from uncoupled simulation is correlated with the SST anomalies from the coupled simulation, the observed significant negative correlation over Western Pacific Ocean is also reproduced (Figure 3.7(d)), which implies that the improved SST-precipitation simulation is due to the inclusion of accurate air-sea feedback. The inferior representation of the simultaneous air-sea feedback over Tropical Indian Ocean in both experiments might be caused by the deficiency in the atmospheric dynamics of atmosphere model. Figure 3.8 shows the local relationship with SST lagging precipitation for 10 days. The large-scale negative

feedback when SST lags rainfall for 10 days is better reproduced with introduction of air-sea coupling.

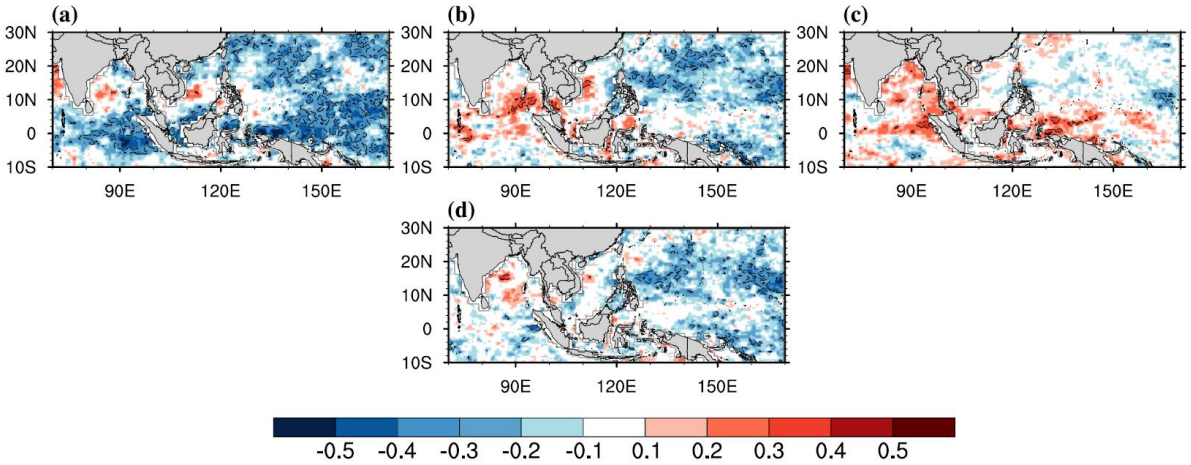

Figure 3.7 Simultaneous relationship between JJA intraseasonal (10-60-day) SST and precipitation in the (a) observation, (b) coupled run, (c) uncoupled run and (d) correlation between SST from the coupled run and the precipitation from the uncoupled run during 1999-2008.

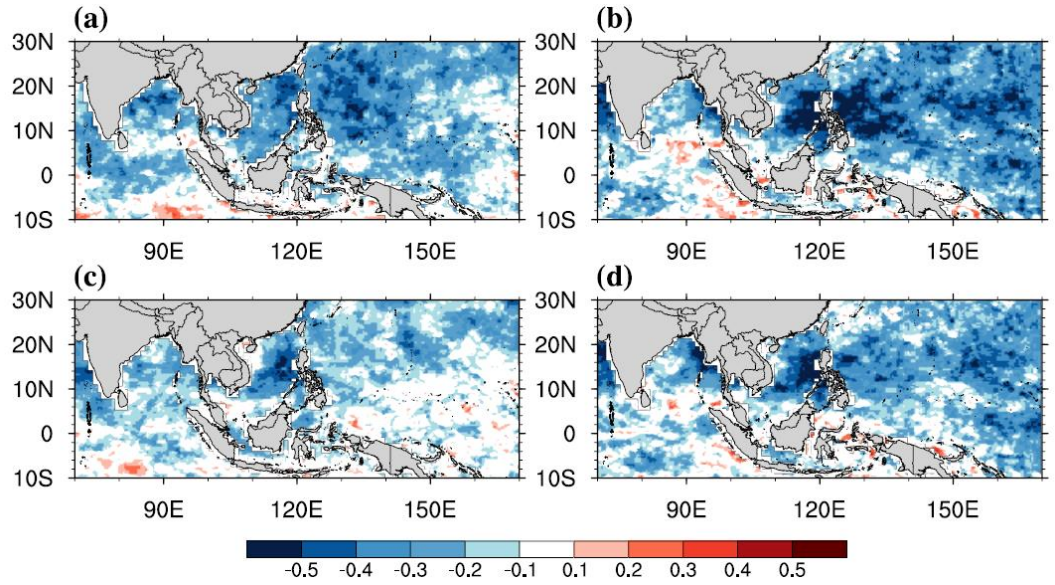

Figure 3.8 SST-precipitation correlation with SST lagging precipitation for 10 days in the (a) observation (b) coupled run, (c) uncoupled run and (d) correlation between SST from the coupled run and precipitation from the uncoupled run during JJA 1999-2008.

3.5.2 Temporal evolution

To explore the model capabilities in simulating the temporal evolution of SST-precipitation relationship, five sub-regions (i.e., ETIO, BOB, SCS, TWP and SWNP) are selected to do further analysis. The 30-day lead-lag local intraseasonal SST-precipitation relationship for all season, summer (June-August) and winter (December-February) in five sub-regions is shown in Figure 3.9. The corresponding leading (lagging) time denotes how quickly the rainfall(SST) responds to the SST(rainfall) anomalies, and the magnitude of the correlation indicates intensity of the driving force (Wu et al., 2007). The air-sea interaction is observed more prominent in summer than in winter with larger magnitude of correlation coefficient. In general, the coupled model could better reproduce the temporal evolution of SST-precipitation relationship compared with the uncoupled one in spite of region and season. It seems that the benefit of coupled run in simulating the temporal features is more prominent over the sub-regions where the atmospheric forcing dominates (e.g., EIO, TWP, SWNP). There are strongest and most frequent intraseasonal variation over TWP, which has been widely used to examine the coupled model performance in previous studies (Kumar et al., 2012; Feng et al., 2018). SST and precipitation exhibit a clear quadrature phase relationship in observation and coupled run while the uncoupled one produce in-phase variation (Figure 3.9(j-i)). In terms of the amplitude of summer season case, the observed maximum(minimum) correlation coefficient when SST leads(lags) precipitation is around 0.58 (-0.60). The coupled model simulates slightly weaker air-sea coupling strength, with maximum (minimum) correlation coefficient at around 0.38(-0.50) in the coupled run. The weaker intensity of intraseasonal precipitation variation (Figure 3.3(f)) and eastward propagation (Figure 3.5(b)) is possibly due to the weaker SST-precipitation relationship. The uncoupled model reproduces much weaker amplitude. In terms of the response time, in observation, the corresponding days with maximum(minimum) correlation occurred at around 16 (5) day in summer. The coupled model produces slightly faster atmospheric response to the ocean forcing with response time of 10 days. The reason for the shorter lag of precipitation when SST leads might be that the atmospheric convective parameterization is sensitive to the SST perturbations (e.g., Tompkins, 2001; Klingaman et al., 2011). However, uncoupled model produces much faster response time (around 4 days) of the precipitation due to the strong SST forcing. In winter, either amplitude or response time is well simulated in coupled model, with 1-3 days difference in simulation of response time (Figure 3.9(l)). It is noted that in one winter case the uncoupled one tends to produce more realistic amplitude and response time when SST lags precipitation (e.g., Figure 3.9(f)). The feedback of precipitation also depends on other factors (e.g., atmospheric moisture, remote SST effect) in addition to the local SST effect.

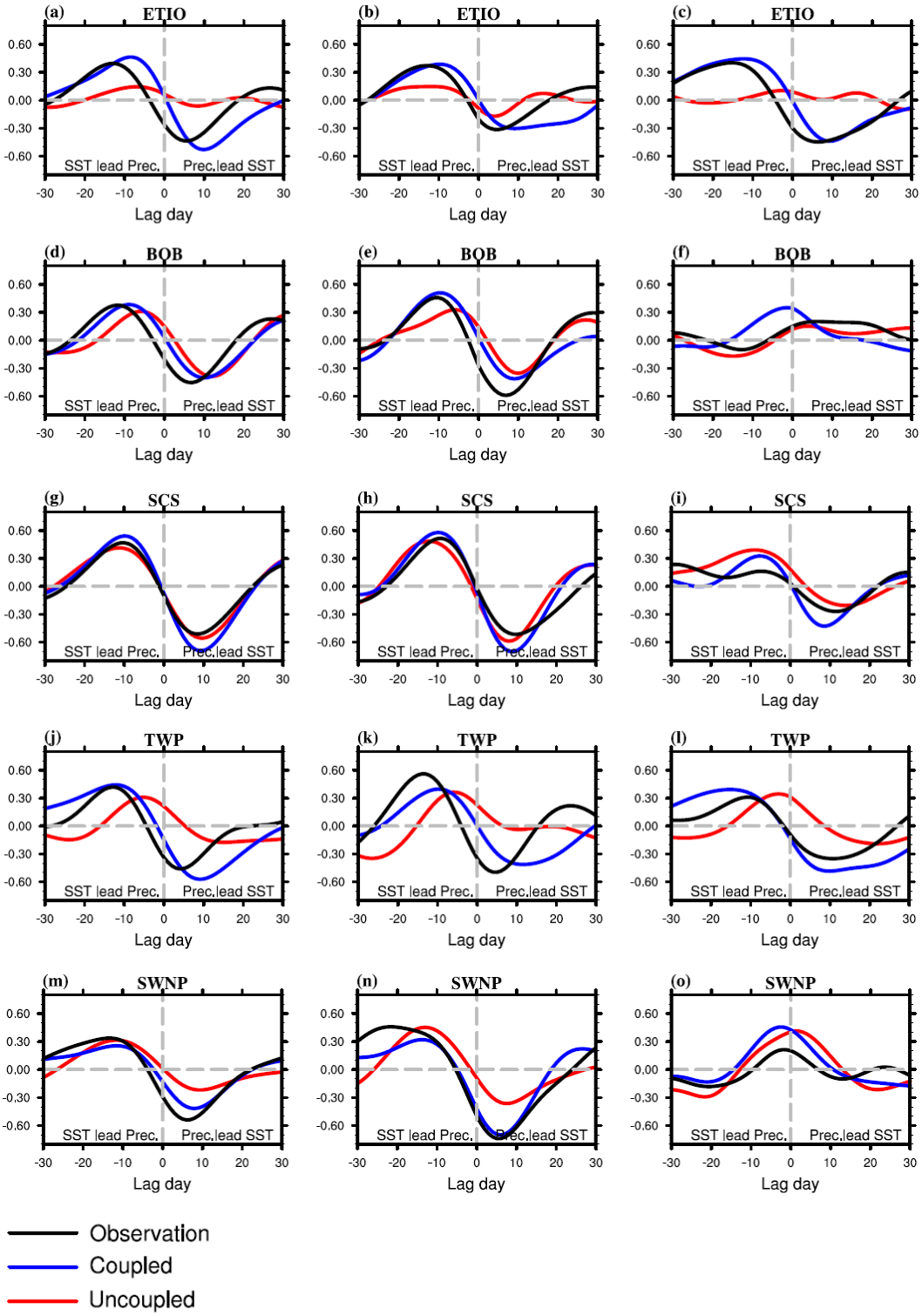

Figure 3.9 30-day lead-lag correlation between (a) annual, (b) JJA and (c) DJF SST and precipitation in uncoupled model (red line), uncoupled model(blue line) and observation(black line) over (a-c) Eastern Tropical Indian Ocean (ETIO;10°S-0°N, 75°E-90°E), (d-f) Bay of Bengal (BOB; 14°N-22°N, 85°E-95°E), (g-i) South China Sea(SCS; 10°N-20°N, 110°E-120°E), (j-l) Tropical Western Pacific (TWP; 10°S-10°N, 130°E-150°E) and (m-o) Subtropical Western North Pacific (SWNP; 15°N-30°N, 130°E-150°E).

3.6 Relationship between sea surface temperature and surface heat fluxes

Another important aspect of atmosphere-ocean coupling is relationship between surface heat flux and SST, which could also provide important information about the nature and intensity of atmospheric or oceanic forcing due to the coupled variation (Wu and You, 2018). The covariations between heat flux and SST are much stronger over East Asia summer monsoon region. Thus, the covariation of SST and heat flux is analyzed in summer (June-August) (Wu et al., 2015).

3.6.1 Spatial variabilities

Shortwave radiation and latent heat flux are two main components of net heat flux (Wu and You, 2018). Figure 3.10 shows the simultaneous correlation between SST and net heat flux, shortwave radiation and latent heat flux in model simulations and observation. In observation, there is a prominent positive correlation (larger than 0.5) in the NHF-SST relationship extending from Eastern Tropical Indian Ocean to Tropical Western Pacific, indicative of the dominance of atmospheric forcing (Figure 3.10(c)). The distribution of positive simultaneous SST-NHF feedback is well consistent with that of negative SST-rainfall feedback (Figure 3.7(c)) as the occurrence of precipitation events is closely associated with the variation of net heat flux. The positive NHF-SST feedback extends eastward from Bay of Bengal to Western Pacific in the coupled run while uncoupled run exhibits significant negative feedback (i.e., dominance of ocean forcing). It is noted that the large positive feedback over ETI and TWP could not be produced by coupled run, which possibly associated with the uncertainties within the validation dataset. The positive feedback over the Tropical region is not so prominent when the SST from TropFlux is used (Figure not shown).

In terms of the simultaneous feedback of heat flux components, in observation, the feedback is more prominent in shortwave radiation than latent heat flux, the positive shortwave radiation-SST correlation is detected over most oceanic region, implying that the shortwave radiation contributes positively to SST variation (Figure 3.10(f)). The extensive positive SST-shortwave radiation correlation is well reproduced by the coupled model (Figure 3.10(e)). As the heat fluxes has no influence on the SST variation, the magnitude of the correlation is relatively weak in uncoupled run, in particular in the shortwave-SST feedback (Figure 3.10(d)).

Cloud is the proxy of the large-scale precipitation process, which has the cooling effect on the SST through modulating the shortwave radiation into the ocean surface. Only the simultaneous relationship between SST and total cloud cover (TCC) in model simulations are shown in Figure

3.10(j-k) as there is no reliable cloud validation dataset. The distribution of SST-shortwave radiation correlation is consistent with the SST-TCC correlation except for the opposite sign (e.g., Figure 3.10(e) and Figure 3.10(k)), suggesting that the improved positive SST-shortwave radiation feedback is potentially related to the improved negative SST-cloud feedback.

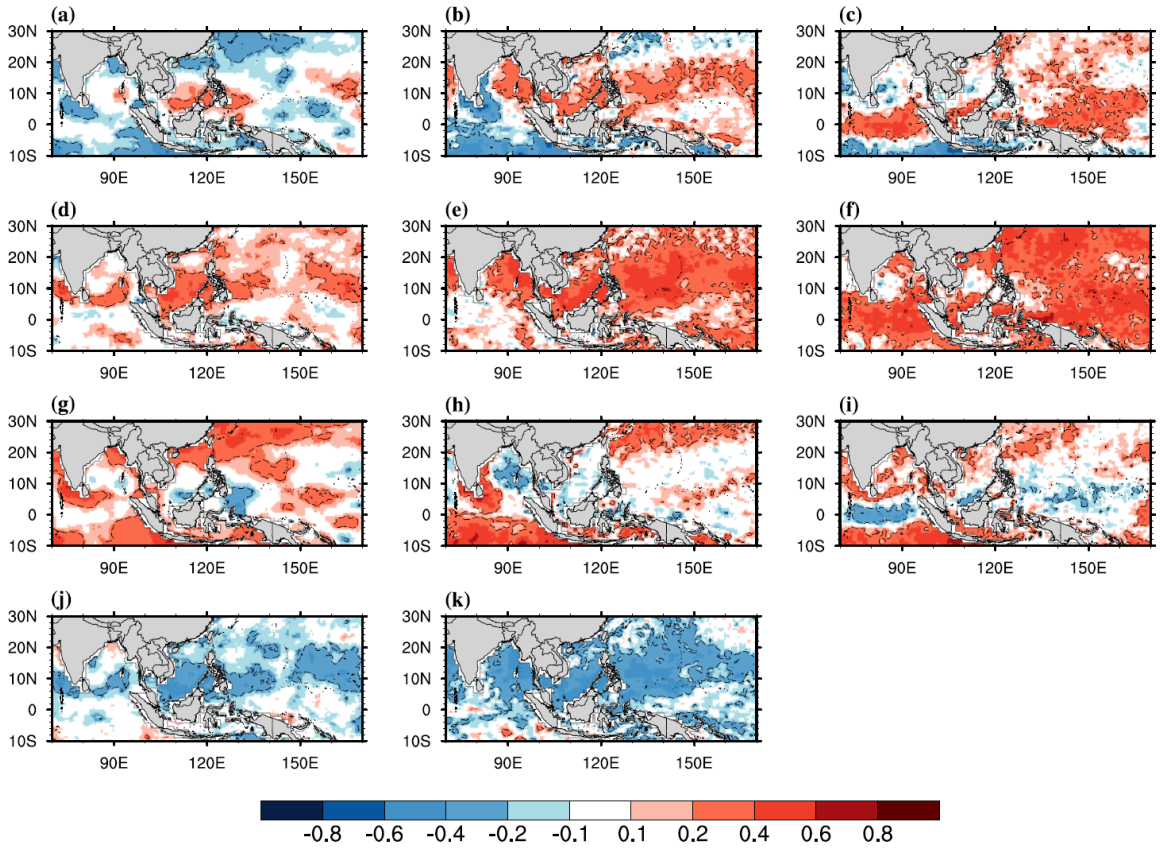

Figure 3.10 Simultaneous correlation between sea surface temperature and (a-c) net surface heat flux, (d-f) net downward shortwave radiation, (g-i) latent heat flux and (j-k) total cloud cover in the uncoupled run (left column), coupled run (middle column) and observation(right column) during JJA 1999-2008.

3.6.2 Temporal evolution

To clarify the temporal evolution of SST-heat fluxes relationship, 30-day lead-lag correlations between SST and heat fluxes (i.e., net heat flux, shortwave radiation and latent heat flux) are calculated over Tropical Western Pacific as an example (Figure 3.11). In observation, the temporal evolution of the two heat flux components (i.e., SWR, LHF) are similar to the change of net heat flux, which indicates that these heat fluxes contribute positively to the net heat flux change. In observation, when SST leads the heat fluxes, the minimum correlation (response time) for SST-NHF, SST-SWR and SST-LHF relationship are -0.53(15 day), -0.57 (15 day) and -0.45(16 day), respectively. The coupled run exhibits slightly better skills with simulated response time (minimum correlation) of NHF at around 11 days (-0.58) while uncoupled run produces faster response time and weaker amplitude of driving force. The amplitude and response time of SST-NHF is contributed by the feedbacks of SST-SWR and SST-LHF. The 4-day faster response of NHF could be attributed by the 7-day faster response of LHF. Larger discrepancies occurred in LHF-SST relationship in coupled one is possibly due to the effects of SST on the near-surface wind speed and air-sea humidity difference. Similarly, the uncoupled run produces much weaker intensity with minimum correlation of SST-LHF(SST-SWR) at around -0.33(-0.20). When SST leads, both of the amplitude and phase are improved in coupled simulation.

When SST lags, there is no causal relationship between heat flux and SST in uncoupled run as the forced SST is specified, with weaker magnitude of maximum correlation(e.g., 0.37 for SST-NHF; 0.20 for SST-SWR) compared with observation (e.g., 0.49 for SST-NHF; 0.53 for SST-SWR). In the coupled run, the most pronounced improvement occurred in the amplitude of maximum SST-SWR correlation. However, the coupled model tends to overestimate the intensity of response of SST to the NHF and LHF with magnitude of maximum correlation 0.2 larger than the observation. These discrepancies are related to the contribution of heat fluxes to the SST variation, which will be investigated in Chapter 4. Figure 3.12 shows the temporal coupling between SST and other atmospheric variables (i.e., precipitation, NHF and SWR). In observation, positive net heat flux leads the positive SST anomalies by 3 days, and consequently triggers the large convection anomalies through inducing unstable atmosphere in 13 days following the strong warming of SST. The downward heat fluxes into the ocean reach minimum with a lag of 1-2 days after the strong convection occurs, and finally resulting in the cold SST in 4 days. The coupled model can reproduce the whole air-sea feedback processes although there are some differences in the phase lag compared with observation.

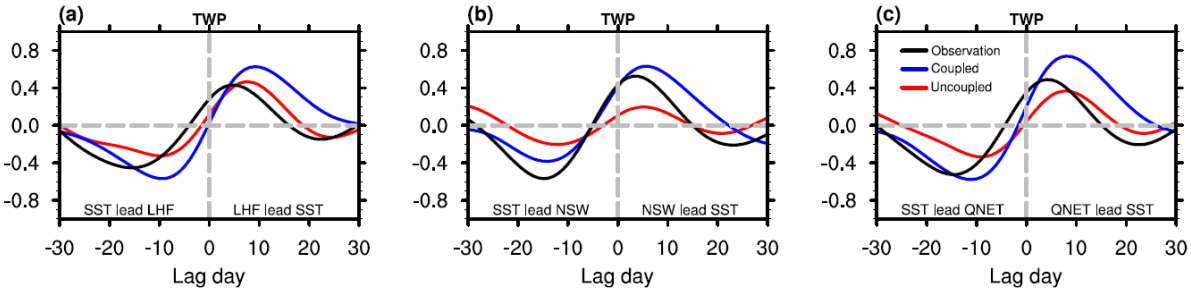

Figure 3.11 30-day lead-lag correlation between JJA sea surface temperature and (a) latent heat flux, (b) shortwave radiation and (c) net heat flux over Tropical Western Pacific.

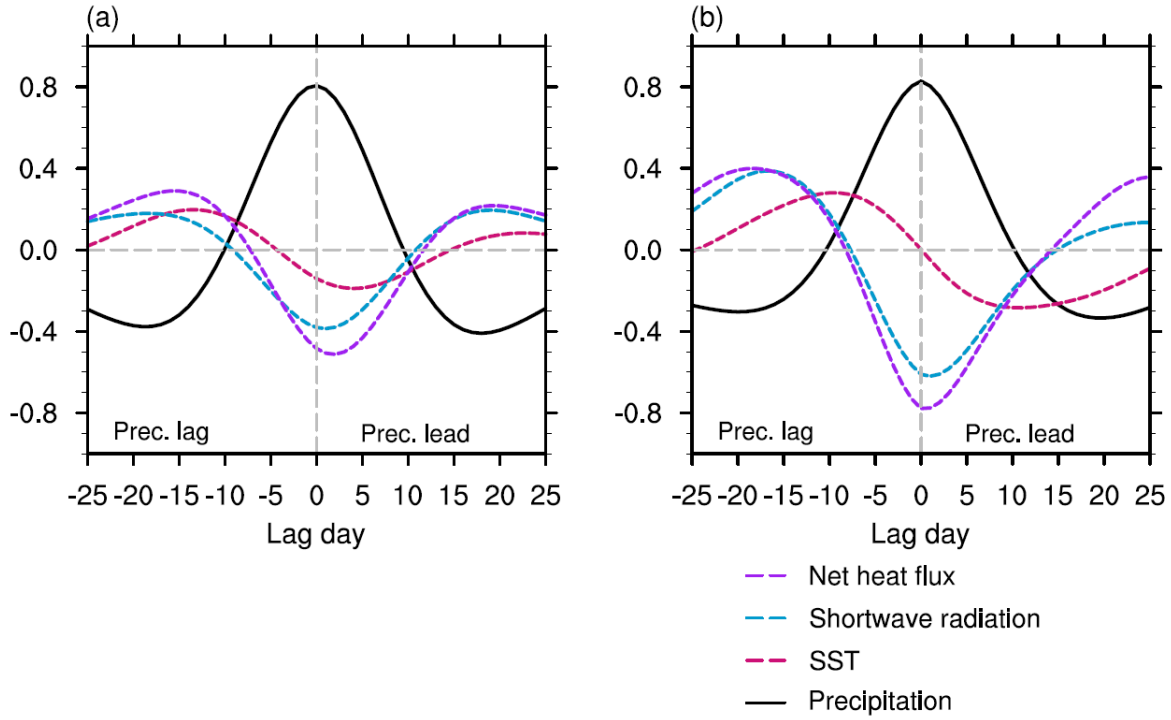

Figure 3.12 Lead-lag regressed anomalies of JJA precipitation (black solid line), sea surface temperature (red dash line), shortwave radiation (blue dash line) and net heat flux(purple dash line) with respect to the precipitation averaged over Tropical Western Pacific in the (a) observation and (b) coupled model RSM-ROMS during 1999-2008.

3.7 Discussion

To confirm the essential role of the air-sea coupling, a perfect experiment is carried out to isolate the coupling issue. The RSM is forced by daily SST simulated by the coupled model (uncoupled_CPLSST hereafter), which is integrated from 1 January 1998 to 31 December 2000. The first year is discarded for the spin-up time. The results of the new experiment are compared with those of uncoupled and coupled runs. Figure 3.13 illustrates the standard deviation of intraseasonal rainfall during May-September. The RMSE(spatial correlation coefficient) is 2.74 mm/day (0.28), 2.48 mm/day (0.38) and 2.45 mm/day (0.38) in the uncoupled , coupled and uncoupled_CPLSST experiment. The discrepancy in the uncoupled run suggests that the response to observed SST forcing in the atmosphere-only RCM differs from the SST-forced response in the observation. The pattern distribution of intraseasonal rainfall over East Asia in the coupled run is similar to that in the uncoupled_CPLSST. The SST-forced responses are same in the coupled run and uncoupled run. The difference between them is due to lack of coupling rather than the coupling unrelated bias in the atmosphere model. These findings agree well with the results of Dai et al. (2018) in which the coupling interval is 6 hours. Actually, we also tried the experiments with 1-hour coupling frequency. The differences between coupled run and uncoupled_CPLSST are still very small.

To check if the weekly SST forcing is also one of potential factor causing the inferior representation in RSM, another experiment (uncoupled_weekly_CPLSST hereafter) hereafter is carried out using the atmosphere-only model RSM forced by the daily interpolated weekly mean SST from the coupled run. The simulation is integrated from 1 January 1998 to 30 April 1998. The first month is discarded for the spin-up time. There are no fundamental differences between the uncoupled experiments forced by daily SST and daily interpolated weekly SST (Figure 3.14(f)). However, as seen from the statistical performance, the spatial correlation coefficient (RMSE) of the standard deviation of intraseasonal precipitation during February to April is 0.23(3.82 mm/day) and 0.25 (3.45 mm/day) in the experiment of uncoupled_weekly_CPLSST and uncoupled_CPLSST, respectively. It implies that the inferior representation in RSM might be due to either lack of air-sea coupling or the use of weekly-mean SST. It should be mentioned that the RMSE is 3.21 (3.23) mm/day in uncoupled_weekly_CPLSST (uncoupled_CPLSST) run, which indicates that the simulation performance in the intraseasonal precipitation variation is not sensitive to the use of weekly-mean SST during warmer season.

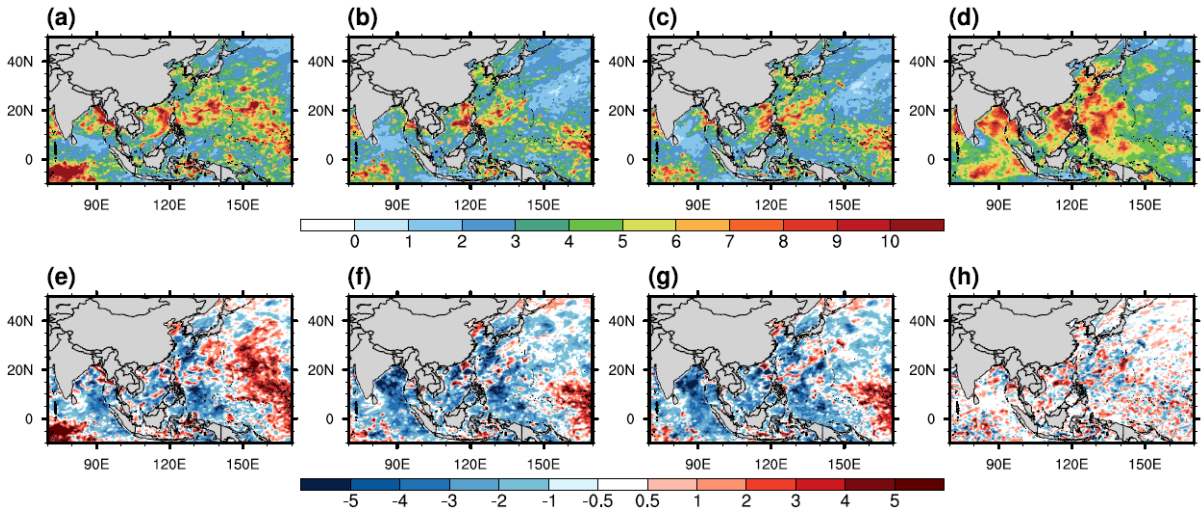

Figure 3.13 Upper panel: Standard deviation of intraseasonal (10-60-day) precipitation (unit: mm/day) in the (a) uncoupled run, (b) coupled run, (c) uncoupled_CPLSST run and (d) TRMM_3B42 during May-September.

Lower panel: differences in the standard deviation of intraseasonal precipitation between the (e) uncoupled run and TRMM_3B42, (f) coupled run and TRMM_3B42, (g) uncoupled_CPLSST and coupled run and (h) coupled and uncoupled run (the former minus the latter).

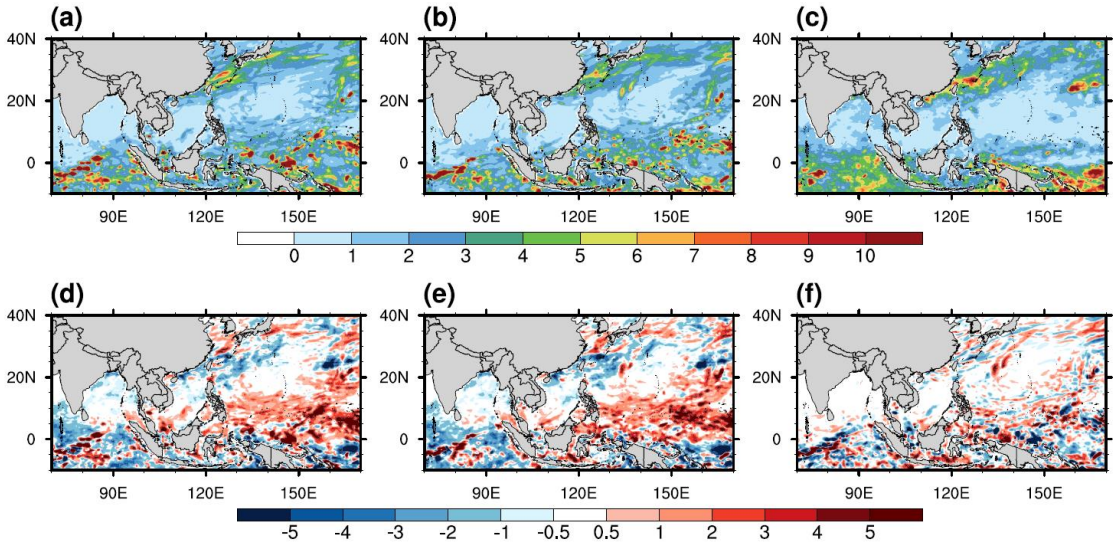

Figure 3.14 Upper panel: Standard deviation of intraseasonal (10-60-day) precipitation (unit: mm/day) in the (a) uncoupled_CPLSST run , (b) uncoupled_weekly_CPLSST run and (c) TRMM_3B42 during February-April.

Lower panel: differences in the standard deviation of intraseasonal precipitation between the (d) uncoupled_CPLSST run and TRMM_3B42, (e) uncoupled_weekly_CPLSST run and TRMM_3B42, (f) uncoupled_CPLSST and uncoupled_weekly_CPLSST run (the former minus the latter).

3.8 Summary

In this chapter, the advantages of air-sea coupling are well demonstrated in the coupled regional climate model RSM-ROMS. Compared with the uncoupled run, the intensity of intraseasonal precipitation variability and the two dominant ISO events (i.e., northward propagation and eastward propagation) are also improved, in particular in the eastward propagation features. The most prominent improvement in boreal summer northward propagation occurs near the equator. The direction of the boreal winter eastward propagating MJO-related precipitation anomalies is more realistically captured in the coupled model. .

The coupled model RSM-ROMS better reproduces the observed features (e.g., response time, coupling intensity) of local intraseasonal SST-precipitation relationship, particularly over Western Pacific, while these features are misrepresented in the uncoupled model RSM due to the spurious prescribed SST forcing. Further experiment proves that the improved intraseasonal features are due

to the inclusion of air-sea coupling in the coupling processes, the ocean-forced responses in the uncoupled and coupled are same. The coupled model better reproduces the cloud-related surface shortwave radiation-SST feedback due to the more realistic cloud-SST feedback.

In general, the coupled model exhibit overall improvement in the air-sea interaction over East Asia.

Chapter 4

Contributions of atmospheric and oceanic processes to SST variation

4.1 Introduction

In chapter 3, the response of SST to net surface heat flux in coupled run is extremely stronger than that in observation over TWP (Figure 3.10(c)). SST is served as an essential communicator between the lower atmosphere and the upper ocean through surface heat fluxes. The relationship between SST and surface heat fluxes largely depends on how the heat fluxes contribute to the SST variation, which further affects other air-sea feedbacks (e.g., SST-precipitation feedback). The SST variation is governed by atmospheric and oceanic processes. Wu and You (2018) demonstrated that the main processes responsible to the SST variation are greatly different between two CMIP5 coupled GCMs. The coupled GCM with SST variation dominated by oceanic processes tends to misrepresent the SST-precipitation feedback. Thus, quantification of the relative contribution of atmospheric and oceanic process to SST tendency is of essential importance. Clarification of the main process responsible to intraseasonal SST variation not only helps to obtain a more in-depth understanding of the coupled processes, but also give some hints to improve the simulation of air-sea interaction in coupled models.

4.2 Methodology and validation dataset

The roles of atmospheric and oceanic processes in generating SST anomalies are estimated using a heat budget equation in the upper-ocean mixed layer (Eq. 4.1; Wu and You 2018).

$$\frac{\partial T_m}{\partial t} = \frac{Q_{net}}{\rho C_p h_m} - V \cdot \nabla T_m - \frac{w_{ent}(T_m - T_d)}{h_m} + R \quad \textbf{(Eq. 4.1)}$$

$\frac{\partial T_m}{\partial t}$ represents the SST tendency, where T_m is the mixed layer temperature that is approximate to SST. $\frac{Q_{net}}{\rho C_p h_m}$ indicates the contribution from atmospheric process (i.e., net surface heat flux), where Q_{net} is the downward net surface heat flux, ρ is the water density, C_p is the capacity of water, h_m is the mixed layer depth. $V \cdot \nabla T_m$ represents the upper-ocean horizonatal advection; $\frac{w_{ent}(T_m - T_d)}{h_m}$ is the vertical entrainment; the residual term R includes some unsolved

processes, such as diffusion caused by the unresolved sub-grid turbulent, errors in the estimation of other terms and so on. The net surface heat flux represents the contribution of atmospheric processes while the oceanic advection and entrainment represents the contribution of oceanic processes (He et al., 2017).

The SST tendency in a specific day is the difference between the SST in the succeeding day minus the SST in the preceding day divided by 2 days (Wu and You, 2018). The calculation method for mixed layer depth is same as that shown in section 2.2.4.

4.3 Results

4.3.1 Intraseasonal variabilities of SST and surface heat flux

In observation, the standard deviation of intraseasonal SST variation exhibits a meridional change, with large magnitude of around 0.4-0.5°C (Figure 4.1(b)) over Subtropical Western North Pacific. In the coupled simulation, although the coupled model is able to reproduce the poleward increase of intraseasonal SST variability, the magnitude of the variabilities is remarkably underestimated. For example, the simulated SST variation is lower than observation by around 0.2 °C over the Kuroshio Current region. It is noted that there are some uncertainties, the OISST tends to underestimate the intraseasonal SST variability especially over Tropical Indian Ocean (Duvel and Vialard, 2007). Compared with the results of Wu and You (2018), the intraseasonal SST variation from OISST dataset is lower than that from TMI dataset by the magnitude of around 0.1-0.2 °C, in particular over the SWNP. The uncertainties in the observation dataset could explain nearly 50% of the model errors.

The intraseasonal NHF variability is observed to be pronounced over Bay of Bengal, Tropical Indian Ocean, South China Sea, and Eastern Philippine Sea, with the magnitude larger than 35 W/m^2 (Figure 4.1(e)). In RSM-ROMS, the strong net heat flux variability extends zonally from Bay of Bengal to the Subtropical Central Pacific. The coupled model tends to underestimate the NHF variation in the regions where there is strong observed NHF variability.

The distribution of intraseasonal SST variation is consistent with the intraseasonal NHF in most regions, indicative of the crucial contribution of NHF. However, there are some inconsistencies in the SST and net heat flux variation. For example, over the ocean region Southeast of Japan, the SST variation is strongest. However, the intensity of intraseasonal NHF is slightly

weaker, suggesting the important role of mixed layer depth or other oceanic processes on regulation of the SST variation.

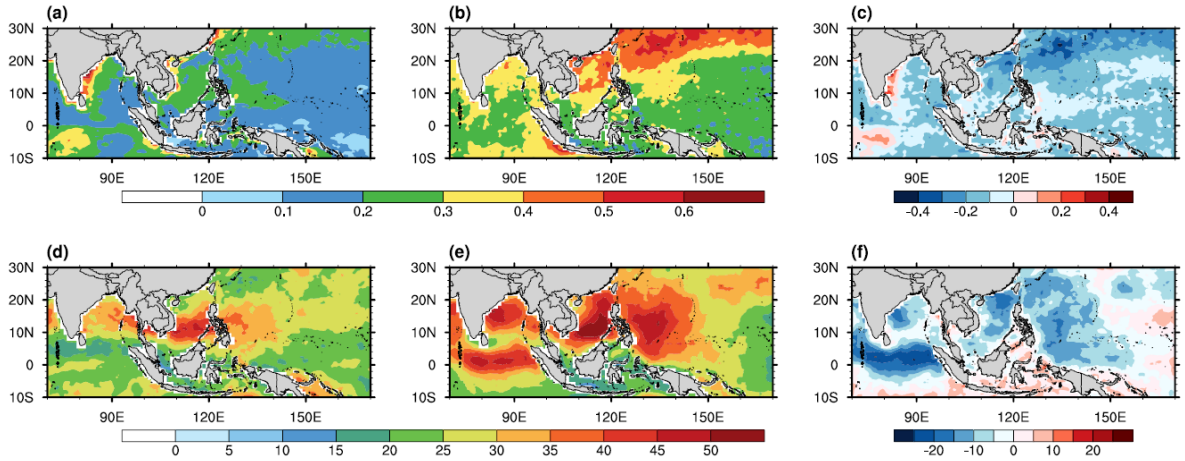

Figure 4.1 Standard deviation of JJA intraseasonal (10-60-day) sea surface temperature (a-c, unit: °C) in the (a) coupled run, (b) observation and (c) difference (model minus observation) between coupled run and observation for the period 1999-2008.

The lower panel is same as the upper panel, but for the intraseasonal net surface heat flux (unit: W/m^2).

4.3.2 Mixed layer depth

The upper ocean mixed layer plays a crucial role in regulating the global climate. The mixed layer depth is an important parameter in determining the quantity of available heat flux for exchange with the atmosphere at the air-sea interface. The net heat flux could exchange with the atmosphere and trigger several air-sea coupled processes (e.g., convection) through the mixed layer depth. The different coherence between intraseasonal SST and surface heat flux depends on the mixed layer depth (Wu et al., 2015). Based on the SST tendency equation (equation 4.1), given the same net heat flux forcing, the shallower mixed layer tend to induce faster response of SST variation (Roxy et al., 2013). Thus, exploration of mixed layer depth simulation in coupled model helps to understand the discrepancies of RSM-ROMS in simulating the SST variation.

The observed MLD exhibits poleward decrease with the deepest MLD larger than 60 meters over Tropical Western North Pacific (Figure 4.2(b)). The distribution of MLD is opposite to that of intraseasonal SST variation (Figure 4.1(b)), implying the shallower mixed layer depth is more effective in inducing the NHF variation. In the coupled model, the meridional variation in the mixed

layer depth is not so apparent compared with the observation (Figure 4.2(a)). There are overall shallower mixed layer depth in RSM-ROMS with largest negative bias (around 25 meters) detected over the Indian Ocean and subtropical Western Pacific. Lower SST variation occurs over Indian Ocean and Eastern Philippine Sea accompanying with shallower mixed layer depth. It is supposed that the negative bias in the net heat flux might overcome the effect of the mixed layer depth.

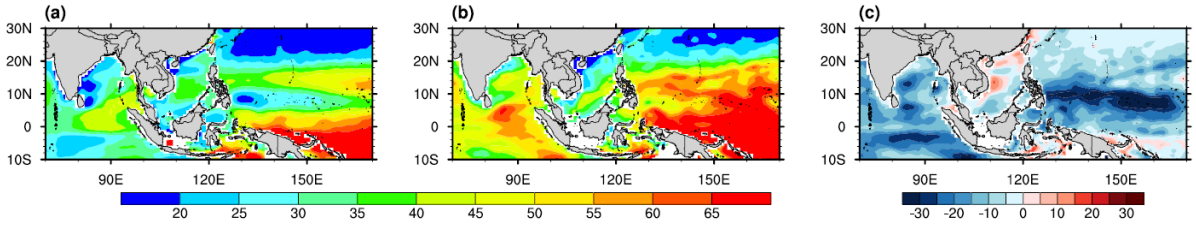

Figure 4.2 JJA mixed layer depth in the (a) coupled simulation, (b) observation and (c) difference (model minus observation) between the coupled run and observation (unit: meter).

4.3.3 Local correlation with SST tendency

SST tendency (SSTn) is an important indicator for the change of ocean. The positive correlation between SST tendency and heat fluxes indicates that the heat fluxes contributes positively to SST variation. The simultaneous correlation between heat fluxes and SST tendency for observation and coupled model simulation is given in Figure 4.3. In observation, the statistically significant positive NHF-SSTn feedbacks are found over almost the whole ocean region (Figure 4.3(b)), signifying remarkable contributions of heat flux to SST variation. The shortwave radiation and latent heat flux contribute positively to the net heat flux variations and consequently the SST variation (Figure 4.3(d-f)). The observed large positive correlation extends northeastward from Bay of Bengal while that extends eastward in coupled run (Figure 4.3(a)). The magnitude of NHF-SSTn correlation is larger by around 0.2-0.4 over Bay of Bengal, South China Sea and subtropical Western Pacific, compared with the observation. It indicates that the coupled model tends to overestimate the contribution of net heat flux to SST variation, which is also found in other coupled GCM (Wu and You 2018). The latent heat flux exhibits larger correlation with SST tendency than shortwave radiation (Figure 4.3(d-f)), which agrees well with the results of Wu and You (2018).

The surface wind speed exhibits twofold effects on the SST variation through latent heat flux and entrainment (Wu et al., 2015). Stronger near-surface wind speed could cause more turbulent fluxes to emit from ocean surface. It is observed that there are large-scale negative surface wind speed-SSTn feedback over almost the entire oceanic region except the coastal region of Tropical

Western Pacific (Figure 4.3(h)), with largest negative correlation (around -0.5~-0.7) found over the oceanic region east of China. The distribution of SSTn-wind speed relationship displays a northeastward extension, which resembles to that of SSTn-NHF relationship (Figure 4.3(b)). In the coupled model, the negative correlation coefficient between SST tendency and near-surface wind speed is larger than that in the observation by the magnitude of 0.2, which might contribute to the stronger effects of heat fluxes to SST variation. The mean state bias in the air-sea humidity difference could affect the contribution of wind speed to the latent heat variations (Wu and You 2018), which needs further detailed analysis.

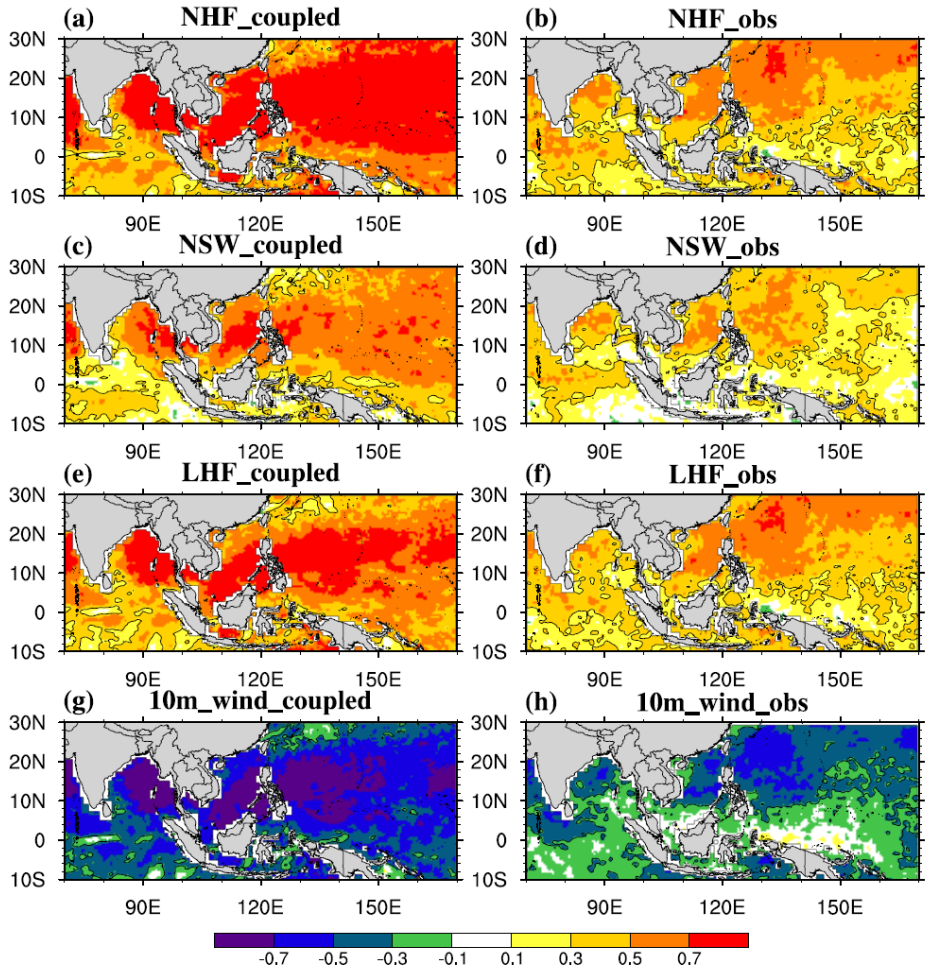

Figure 4.3 Simultaneous relationship between JJA SST tendency and (a-b) net surface heat flux, (c-d) shortwave radiation, (e-f) latent heat and (g-h) 10-meter wind speed during 1999-2008.

4.3.4 Contribution of surface heat fluxes to SST variation

To quantify the contribution of atmospheric process (i.e., surface heat flux) to the SST variation, the regressed anomalies of net surface heat flux and four heat flux components (i.e., SWR, LWR, LHF and SHF) with respect to the SST tendency at each grid point are calculated. The regressed surface heat fluxes are then converted to the unit of SST tendency based on the monthly observed and simulated mixed layer depth.

Figure 4.4 shows the contribution percentage of NHF, LHF and SWR to the SST tendency in coupled run and observation. In observation, the large contribution percentage extends northeastward from head of Bay of Bengal to SWNP with the magnitude of around 30%. The distribution of contribution percentage is similar to the NHF-SSTn relationship (Figure 4.3). Much smaller contribution percentage of NHF occurs in the near-equatorial regions, implying that the oceanic processes dominates the SST variation over these regions (He et al., 2017). However, in the RSM-ROMS, the contribution percentage displays slightly different distribution, with prominent contribution extending from the Southeast Bay of Bengal to subtropical western Pacific at the magnitude more than 70%. The SST tendency explained by the surface heat flux is much larger in coupled model compared with observation, which is closely associated with the bias in the simulated mixed layer depth (Figure 4.2(c)). The shallower mixed layer depth tends to cause the net heat flux to be more effective in inducing the SST variation (Wu et al., 2015).

The effect of NHF to SST variation could be attributed to the SWR and LHF. The contribution percentage of these two heat flux components exhibits regional dependence. In observation, the LHF contributes approximately 5-10% more than the SWR over the SWNP while the SWR contributes nearly 10% more than the LHF over South China Sea and head of BOB. Based on the SST dataset from Tropical Rainfall Measuring Mission Microwave (TMI) and the daily surface heat flux from NCEP-DOE Reanalysis 2, Wu et al. (2015) shows that the latent heat flux contributes much larger than shortwave radiation to SST variation. It is contrary to the results in our study, implying the estimated contribution is also affected by validation dataset.

The regional-mean contribution percentage over South China Sea (indicated as the black box in Figure 4.4) in model simulation and observation is further calculated in Table 4.1. In observation, all the heat fluxes have positive contribution to SST variation except longwave radiation. The contributions of shortwave radiation and latent heat flux are comparable, which combinedly account for almost 100% of the net heat flux contribution. The longwave radiation and sensible heat flux contribute much less. In the coupled model, the net heat flux has a leading contribution to SST variation. However, it produces 30% more of the net heat flux contribution than the

observation, which is attributed to the overestimated contribution of net shortwave radiation (around 20% more) and latent heat flux (around 10% more).

Figure 4.5 gives the temporal evolution of the total SST tendency and heat fluxes over South China Sea. Net heat flux accounts for approximately two thirds of the peak SST tendency in observation while it could explain almost the whole SST variation in RSM-ROMS. It is noted that there is 1-2 days phase lag between NHF and total SST tendency, indicative of the important role of other contribution terms (e.g., oceanic processes). The estimation contains uncertainties from various aspects, such as validation dataset, calculation of mixed layer depth and so on (Wu et al., 2015).

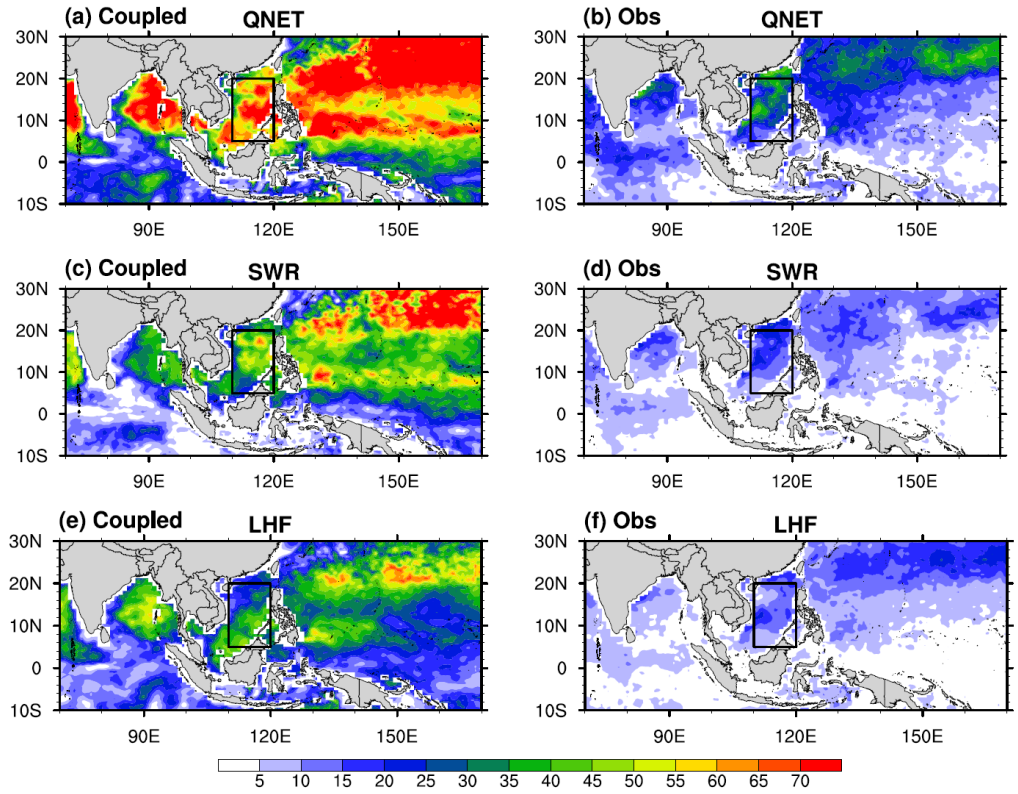

Figure 4.4 Percentage (unit: %) of JJA SST tendency explained by net surface heat flux (a-b), shortwave radiation(c-d) and latent heat flux (e-f) in the coupled model (left column) and observation (right column). (The black box indicates South China Sea)

Table 4.1 Contribution percentage of JJA surface heat fluxes to SST tendency over South China Sea during 1999-2008 (denoted by black box in Figure 4.4).

Contribution Percentage (%)	Coupled model	Observation
Net heat flux	**61**	**29**
Net shortwave radiation	**40**	**16**
Latent heat	**31**	**13**
Longwave radiation	**-9**	**-1**
Sensible heat	**-1**	**1**

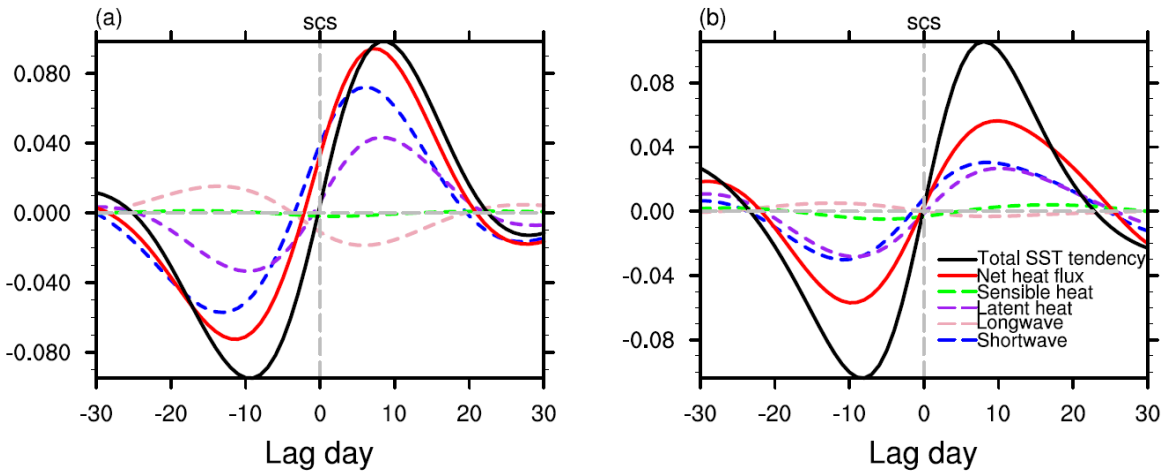

Figure 4.5 Lead-lag regressed anomalies of JJA intraseasonal (10-60-day) total SST tendency (black solid line), net surface heat flux (red solid line), shortwave radiation (blue dash line), longwave radiation (pink dash line), latent heat (purple dash line) and sensible heat (green dash line) with respect to the SST averaged over South China Sea in the (a) coupled model RSM-ROMS and (b) observation during 1999-2008.

4.4 Discussion

To testify the uncertainties of the quantification of heat flux contribution to the SST variation, the daily SST from the TropFlux (Kumar et al., 2012) at a horizontal resolution of 1 degree is used to testify the fidelity of the estimations. Compared with the result shown in Figure 4.4, the contribution percentage is larger when TropFlux SST is used. The net heat flux contributes around 50% to the SST variation. The spatial variations of contribution percentage are similar when the two different SST validation datasets are used (Figure 4.4(b) and Figure 4.6(b)). However, the contribution percentage is approximately 10% larger over most of the oceanic region when the TropFlux SST dataset is used. However, the overestimation of the heat flux contribution in coupled run is still prominent. Thus, the conclusion will not change when either the OISST or TropFlux SST dataset is used. Apart from the uncertainties from the validation dataset, the estimation uncertainties are also derived from other aspects, which needs further confirmation.

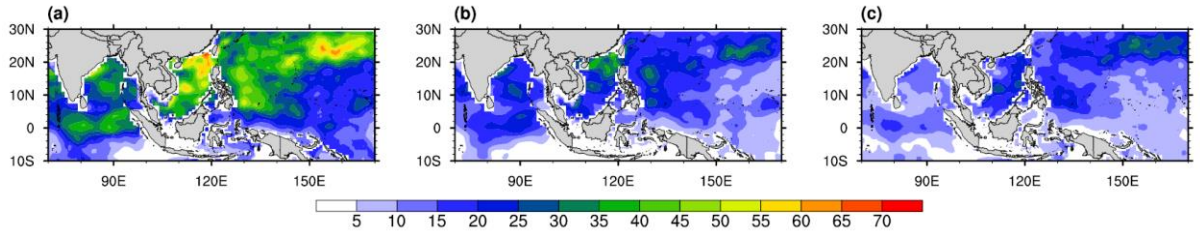

Figure 4.6 Percentage (unit: %) of JJA SST tendency explained by (a) net surface heat flux, (b) shortwave radiation and (c) latent heat flux in the observation (SST is derived from the TropFlux product; heat fluxes are derived from the OAFlux products).

4.5 Summary

The main process responsible to the SST variation in RSM-ROMS is well clarified according to the above analysis of upper ocean heat budget. It is found that the SST variation is primarily contributed by atmospheric processes in RSM-ROMS, but its relative contribution is overestimated possibly due to the shallower mixed layer depth. In addition to the contribution from surface heat fluxes, other contribution terms (e.g., Ekman entrainment) needs to be taken into consideration, especially over the equatorial regions. The surface heat budget cannot be fully balanced due to diverse reasons (He et al., 2017), reliable ocean dataset with high temporal resolution is needed to accurately estimate the contribution from oceanic processes.

Chapter 5

Impacts of higher resolution on mean climate and intraseasonal variability over East Asia

5.1 Introduction

The benefit of air-sea coupling has been well demonstrated in Chapter 3. However, it is revealed that there are some deficiencies in the simulation of intraseasonal air-sea interaction for RSM-ROMS. In chapter 4, the summer intraseasonal SST variation is underestimated in RSM-ROMS, in particular over the regions with active air-sea interactions. The thermodynamics in the upper ocean are not well represented such as shallower mixed layer depth. The reproduction of boreal summer intraseasonal oscillation and MJO events over East Asia monsoon region demands not only the air-sea coupling but also the realistic underling intraseasonal SST variability (Zhang et al., 2019). Thus, a realistic representation of intraseasonal SST variation in coupled model is essential for the intraseasonal rainfall prediction.

Previous studies demonstrated that the increase of coupling frequency (e.g., Hu et al., 2015), upper ocean vertical resolution (e.g., Ge et al., 2017) or horizontal resolution (e.g., Peatman and Klingaman, 2018) are effective methods to improve the simulation of intraseasonal variabilities. Accurate simulation of the MJO could be achieved by capturing the temperature variations in the upper few meters through finer ocean vertical resolution (Tseng et al., 2015). Based on a partially coupling global climate model, Klingaman et al. (2011) showed that simultaneous increase in both vertical resolution and coupling frequency could produce organized, northward-propagation convection. Ge et al. (2017) demonstrated that 1-meter vertical resolution helped to produce stronger diurnal and intraseasonal variability using an ocean general circulation model.

The 10-meter uppermost layer for the ocean component is commonly used in most of the current coupled CGMs and RCMs, which might be insufficient to reproduce the large vertical ocean temperature gradient near the ocean surface in the regions where the upper-ocean air-sea exchange is active. The uppermost thickness for the model experiments in chapter 2 and 3 is around 10 meters over most open-ocean areas, which is still insufficient to realistically simulate the SST variability. Thus, an appropriate vertical resolution for RSM-ROMS is essential for the simulation and prediction of SST accompanying with better representation of upper ocean thermodynamic process.

In another aspect, chapter 2 shows that finer resolution (i.e., 10-km) could improve the simulation of ocean thermodynamics over Subtropical Western North Pacific. In terms of the tropical intraseasonal activities, based on the coupled GCM MetUM-GOML2.0 with coupling activated over Indian Ocean only, Peatman and Klingaman (2018) found that the atmospheric mean state was significantly improved when the resolution moved from 200-km to 90-km, but no substantial improvement was detected when the resolution increased to 40-km. However, it is still not clear whether the atmospheric mean state will improve when the horizontal resolution goes down to the convective-scale (e.g., 10-km). Misra et al., (2018) showed that the finer spatial resolution (i.e., 10-km) might be one of the reasons for the major improvements in the northward propagation characteristics (e.g., larger amplitude, northwest-southeast tilt and faster phase speed) of ISV over Indian summer monsoon region for RSM-ROMS. The impact of finer resolution on tropical MJO phenomenon has not yet been examined. In addition, despite more realistic eastward propagation features over Western Pacific in coupled run, some deficiencies still remain over maritime continents (from the longitude of 100°E to 140°E) with lower amplitude compared with uncoupled one (Figure 3.5). Whether the finer resolution benefits the simulation of MJO or not is required to be tested.

In fact, the effects of increasing resolution could be model dependent. In addition, most of works use partially coupled global climate model or ocean general circulation models, few studies are based on regional climate models. The main purpose of the study in this chapter is to clarify the impact of higher resolution on mean climate and intraseasonal variability over East Asia.

5.2 Impacts of higher ocean vertical resolution

5.2.1 Experimental design and validation dataset

The ocean component ROMS uses sigma coordinate system with the ocean layers distributed unevenly. The vertically stretched coordinates of oceanic component ROMS allows an increased resolution at the surface and at the bottom by modifying the stretching parameters Theta_s and Theta_b, respectively. The temperature at the top layer is taken as the sea surface temperature. The detailed experiment settings are shown in Table 5.1. Two sets of experiments are conducted to explore the effect of higher vertical ocean resolution. The control run uses 30 layers with uppermost thickness at around 10 meters in most open ocean region. The second runs uses 50 layers with uppermost thickness at around 0.5 meters. Figure 5.1 and Figure 5.2 show the uppermost thickness and vertical distribution of depths, respectively. In the higher resolution run, the stretching

parameters Theta_s and Theta_b are set to 0.7 and 0.1 to make the upper ocean layers more dense. There are around 20 (6) layers in the top 150 meters for the EXP_50lev (EXP_30lev) run. The vertical resolution gradually increases with the depth. The bottom layers are similar in these two runs with around 16 (13) layers in the EXP_30lev (EXP_50lev) at the depths between 1000 and 4200 meters. For each experiment, same atmospheric and oceanic forcing are used as shown in Table 3.1. In each run, the model is integrated from January 1998 to December 2000 at a horizontal resolution of 25-km. The results in warmer season (May-August) during 1998-2000 are analyzed.

Table 5.1 List of experiments performed

Experiment Names	Model Components	Number of Ocean Levels	Uppermost Thickness	Stretching Parameters	Horizontal Resolution	Integration Time
EXP_30lev	Coupled atmosphere-ocean	30 layers	~ 10 meters	Theta_s = 4.0 Theta_b = 0.4	25km	01/01/1998~ 31/12/2000
EXP_50lev		50 layers	~ 0.5 meters	Theta_s = 7.0 Theta_b = 0.1		

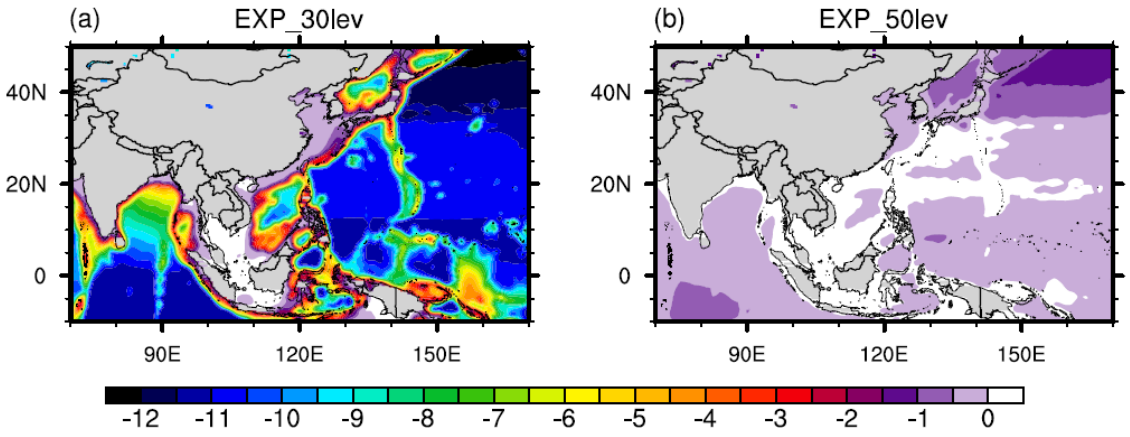

Figure 5.1 Uppermost layer thickness (unit: meter) in the experiment of (a) EXP_30lev and (b) EXP_50lev.

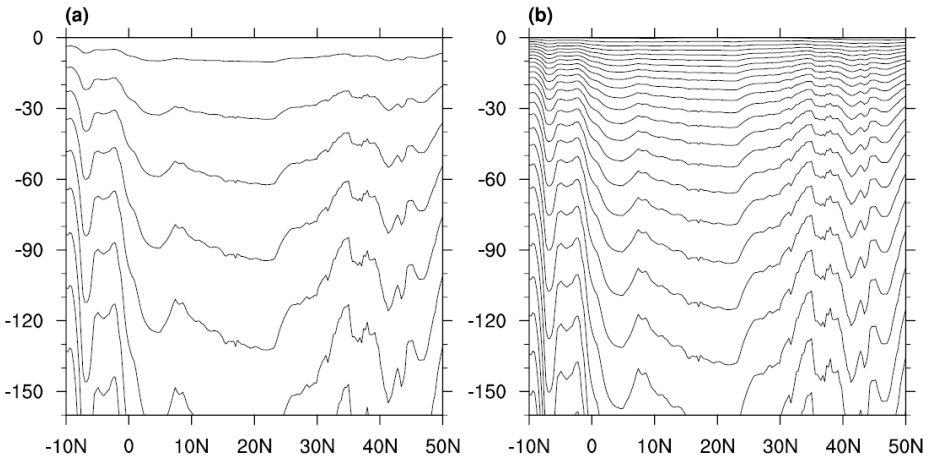

Figure 5.2 Vertical distribution of depths averaged across the longitude of 120-170°E in the top 150 meters for the experiment of (a) EXP_30lev and (b) EXP_50lev.

(x-axis indicates the latitude; y-axis indicates the depth)

5.2.2 Effects on mean state of the climate

5.2.2.1 Sea surface temperature and precipitation

Figure 5.3 shows monthly variations of SST bias averaged over Western Pacific (130°E-170°E) in the two experiments. The warmer SST bias at latitudes north of 40°N during colder season and the pronounced cold SST biases at latitudes north of 20°N during warmer season are significantly alleviated. It is supposed that the thinner uppermost thickness in the finer-resolution run helps to make the modeled SST warmer than that in coarser resolution. Increasing resolution tends to exhibit the most prominent improvement of the SST over the Kuroshio-Oyashio Current region (Figure 5.4(a-c)). It is supposed that the finer resolution tends to better capture the features because there is sharp ocean temperature gradient in the upper ocean over those regions. Additionally, little significant positive impacts are exerted on the simulation of precipitation under the effects of increasing vertical resolution (Figure 5.4(f)).

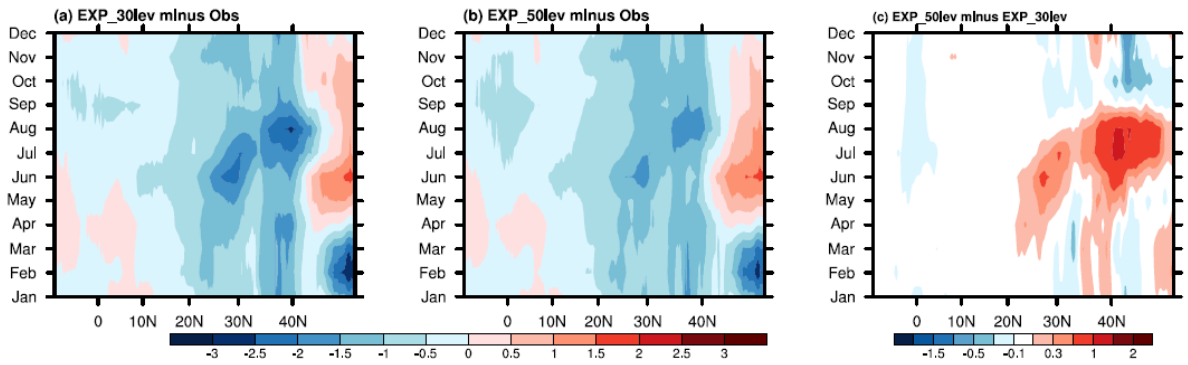

Figure 5.3 Time-latitude cross section of difference in the mean monthly SST (unit: °C) averaged along 110 °E -170°E between (a) EXP_30lev and observation (EXP_30lev minus observation), (b) EXP_50lev and observation (EXP_50lev minus observation) and (c) EXP_50lev and EXP_30lev (EXP_50lev minus EXP_30lev) during May-August.

(x-axis indicates the latitude; y-axis indicates the months)

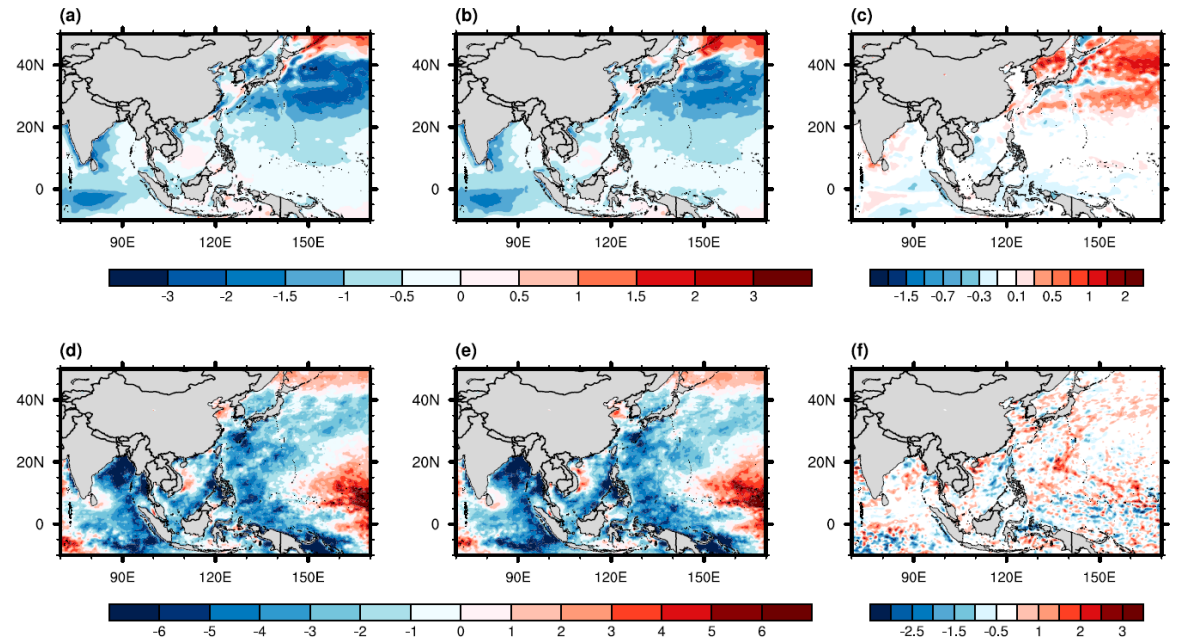

Figure 5.4 Climatological differences in MJJA mean sea surface temperature (upper panel; unit: °C) and rainfall (lower panel; unit: mm/day) between (a) EXP_30lev and observation (EXP_30lev minus observation), (b) EXP_50lev and observation (EXP_50lev minus observation) and (c) EXP_50lev and EXP_30lev (EXP_50lev minus EXP_30lev).

5.2.2.2 Ocean temperature, salinity and vertical velocity

Temperature and salinity are predominant oceanographic parameters, and impacts of higher vertical resolution on these variables are assessed in this subsection. Figure 5.5 shows the vertical profiles of ocean temperature in the above 500 meters over four sub-regions (i.e., Indian Ocean, South China Sea, Tropical Western Pacific and Subtropical Western North Pacific). The ocean temperature is consistently warmed up in the EXP_50lev run compared with the EXP_30lev run at depths above 500 meters over Indian Ocean, SCS and TWP. The maximum reduction of the cold temperature bias (around 0.5 ℃) occurs in the upper ocean at the depth of around -50 and -120 meters over Indian Ocean and TWP region, respectively (Figure 5.5(a) and 5.5(c)). However, increasing resolution remarkably enhances the cold ocean temperature bias in the above 50 meters over SWNP with the maximum increase magnitude of around 0.3 ℃ (Figure 5.5(d)). In general, the colder temperature bias over the entire East Asia is overall improved in the top 500 meters (Figure 5.6(a)), which is due to the alleviation of the strong upwelling motion(Figure 5.6(b)).

The subsurface ocean temperature exhibits the prominent improvement over the coastal region of BOB, Tropical Eastern Indian Ocean and Near-Equatorial Western Pacific (Figure 5.7(c)). However, the effects are slightly different over the Kuroshio-Oyashio Current region with aggravation of cold ocean temperature bias. Compared with the coarser resolution run, the upper ocean salinity is greatly overestimated in the finer resolution run, in particular over shallow water region and coastal regions (e.g., East China Sea, Bay of Bengal) where there is huge input of grand rivers (Figure 5.7(f)). The strong link between salinity between surface salinity and freshwater fluxes has been clarified in previous studies (e.g., Vinogradova and Ponte, 2013). There are significant positive bias in net freshwater flux (defined as evaporation minus precipitation) over the maritime continent and coastal regions in the two experiments, indicating that the excessive evaporation takes place (Figure 5.8(a-b)). This discrepancy is due to lack of river runoff input. The crucial role of river discharge on upper-ocean stratification and feedback in the coupled climate system over East Asia has been demonstrated in some previous studies (e.g., Sandeep et al., 2018; Kako et al., 2016). Misra et al. (2018) mentioned that the absence of discharge in RSM-ROMS was likely to affect the intraseasonal variabilities of SST and precipitation followed by the impact on MLD. It is supposed that the unrealistic large salinity could be improved by including the river discharge in the coupled model. When the vertical ocean resolution is increased, the net freshwater flux does not exhibit large significant difference over the whole domain (Figure 5.8(c)). However, in some sub-regions (e.g., South China Sea), the positive net freshwater flux is consistent with the higher salinity, implying that the net freshwater flux partially contributes to the higher salinity in higher vertical resolution run. Increasing vertical resolution might degrade the simulation of

horizontal advection and vertical movement of salinity, which need to do more analysis on the upper-ocean salinity budget.

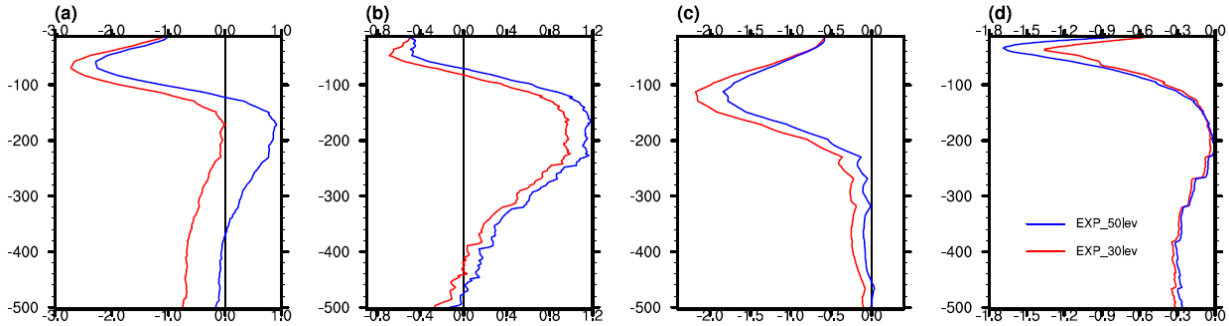

Figure 5.5 Vertical profiles of difference (model minus observation) in the MJJA ocean temperature (unit: ℃) averaged over (a) Indian Ocean(10°S-25°N, 70°E-100°E); (b) South China Sea (5°N-20°N, 110°E-120°E); (c) Tropical Western Pacific (5°N-20°N; 130°E-170°E) and (d) Subtropical Western North Pacific (25°N-50°N, 130°E-170°E) in the top 500 meters for the experiment of EXP_30lev and EXP_50lev.

(Red line indicates the EXP_30lev run; blue line indicates the EXP_50lev run)

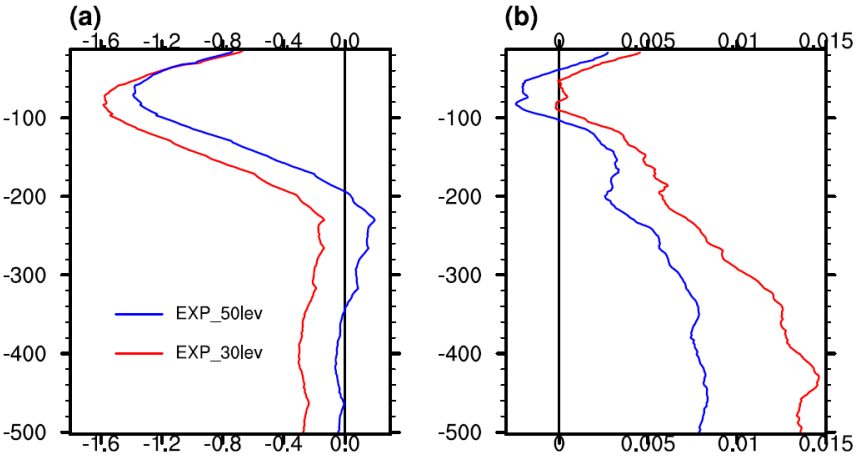

Figure 5.6 Vertical profiles of difference (model minus observation) in the MJJA (a) ocean temperature (unit: ℃) and (b) vertical velocity (unit: $\times 10^{-4}$ m/s) averaged over East Asia (10°S-50°N; 70°E-170°E) in the top 500 meters for the experiment of EXP_30lev and EXP_50lev.

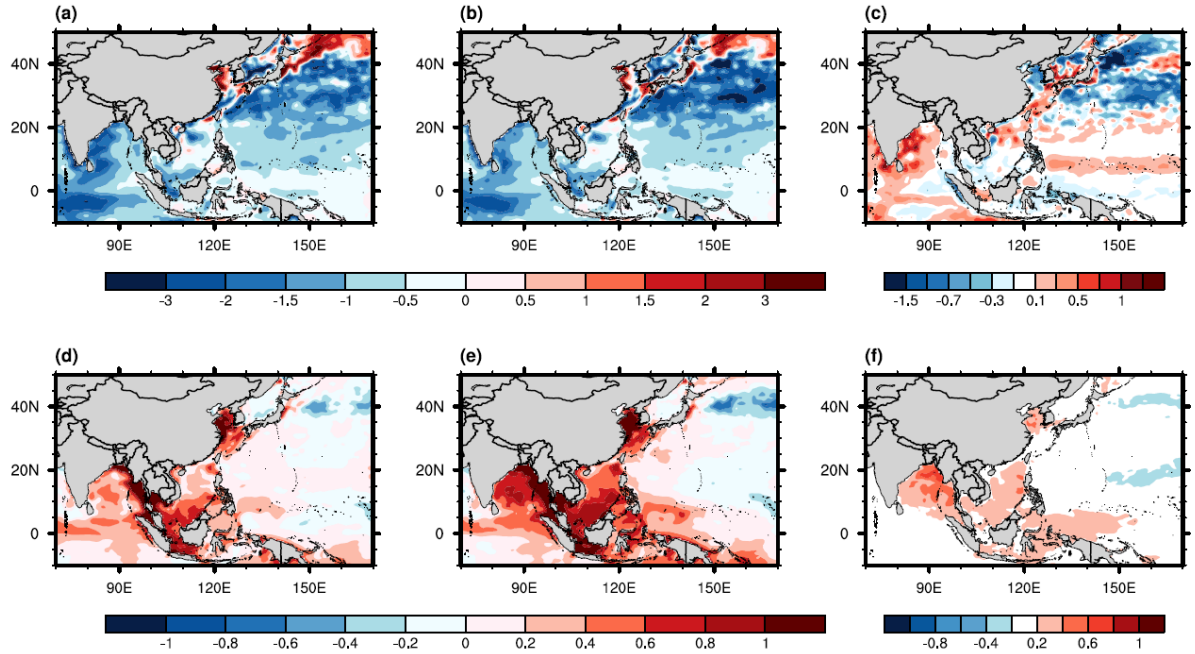

Figure 5.7 Climatological difference in MJJA ocean temperature (upper panel; unit: °C) and salinity (lower panel; unit: PSU) in the top 30 meters between (a) EXP_30lev and observation (EXP_30lev minus observation), (b) EXP_50lev and observation (EXP_50lev minus observation) and (c) EXP_50lev and EXP_30lev (EXP_50lev minus EXP_30lev).

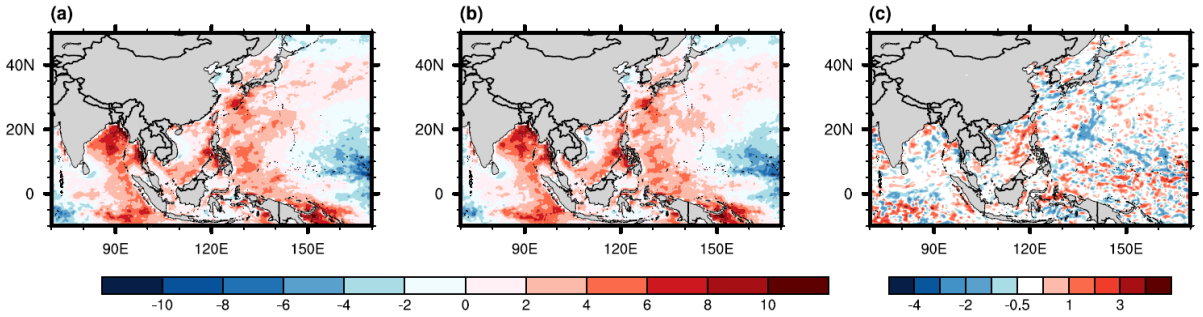

Figure 5.8 Climatological difference in MJJA net freshwater flux (evaporation minus precipitation, unit: mm/day) between (a) EXP_30lev and observation (EXP_30lev minus observation), (b) EXP_50lev and observation (EXP_50lev minus observation) and (c) EXP_50lev and EXP_30lev (EXP_50lev minus EXP_30lev).

5.2.2.3 Mixed layer depth

The mixed layer depth determines how the ocean and atmosphere interact in the air-sea interface, which could indicate the change of oceanic thermodynamic under the impact of the increasing vertical resolution. The definition of the mixed layer depth is already given in sub-section 4.2 of chapter 4.

The effect of higher resolution on the distribution of MLD is not so apparent with slight increase of pattern correlation from 0.84 in the EXP_30lev to 0.87 in the EXP_50lev (Figure 5.9 (a-b)). In the control run (i.e., EXP_30lev), there is pronounced shallower mixed layer depth over Indian Ocean and TWP with the maximum magnitude of around 40 meters (Figure 5.9(d)). When the vertical resolution is enhanced, the shallower mixed layer depth deepens with the maximum increase magnitude of around 10 meters over Indian Ocean and TWP (Figure 5.9(f)). However, the effects of increasing resolution on MLD is tiny over the high-latitude regions where there is smaller MLD bias in the control run. The RMSE(bias) of MLD over East Asia in the EXP_30lev and EXP_50lev run is 16.48(-11.26) meters and 14.06(-8.85) meters, respectively. These improvements are due to more realistic simulated vertical temperature profiles (Figure 5.5).

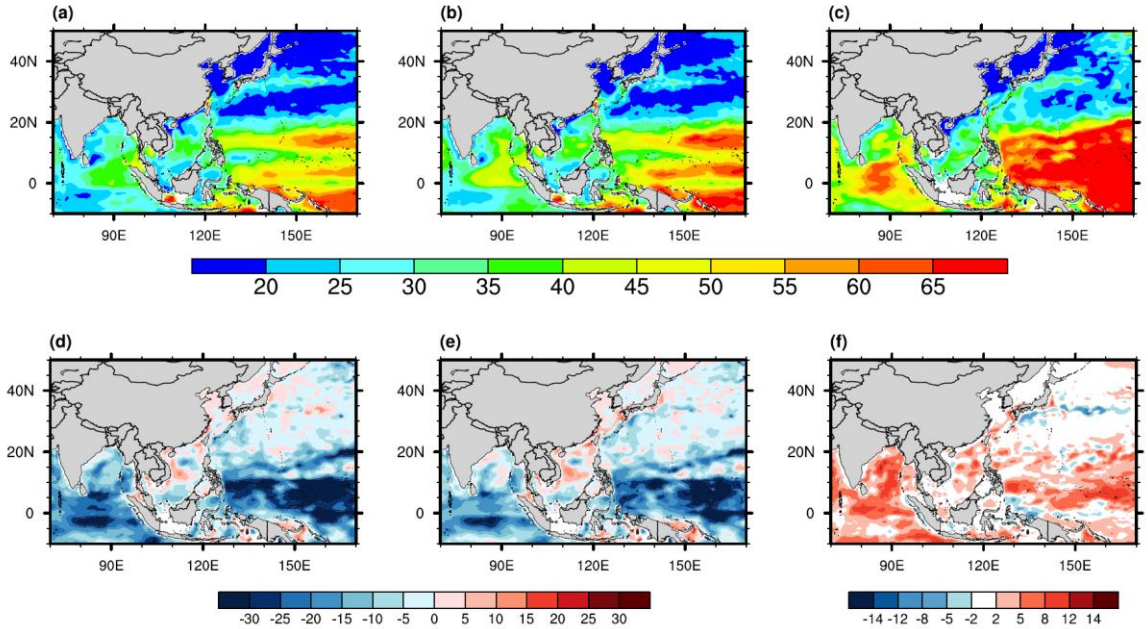

Figure 5.9 Climatological mean MJJA mixed layer depth (unit: meter) in the (a) EXP_30lev run , (b) EXP_50lev run and (c) observation and difference between (d) EXP_30lev and observation(EXP_30lev minus observation), (e) EXP_50lev and observation(EXP_50lev minus observation) and (f) EXP_50lev with EXP_30lev (EXP_50lev minus EXP_30lev) during 1998-2000.

5.2.3 Effects on Intraseasonal variability

Similar to the effects on mean state SST, the lower intraseasonal SST variation over Kuroshio-Oyashio Current region in the EXP_30lev run is remarkably enhanced in the EXP_50lev run due to the lower thermal inertia caused by the thinner uppermost ocean layer thickness(Figure 5.10(f)). However, increasing vertical resolution causes tiny change over Indian Ocean and Western Pacific. The pattern correlation coefficient (RMSE) of intraseasonal SST variability is increased(reduced) by around 0.13 (0.02 °C) in the EXP_50lev compared with the EXP_30lev. Additionally, increasing vertical resolution exhibits little impact on intraseasonal precipitation variability (Figure not shown). Based on a partially coupled global climate model, Klingaman et al.(2011) shows that increasing either vertical resolution or air-sea coupling frequency alone makes smallest increase in the intraseasonal variabilities. Only increasing coupling frequency and vertical resolution simultaneously could improve the intraseasonal precipitation accompanying with the northward propagation. The impacts could be model dependent. Generally speaking, a straightforward resolution increase in ocean sub-model ROMS doesnot facilitate the improvement of the intraseasonal variation of precipitation, which emphasizes the need for the optimization of the parameterization scheme that go hand in hand with the resolution increase in RSM-ROMS.

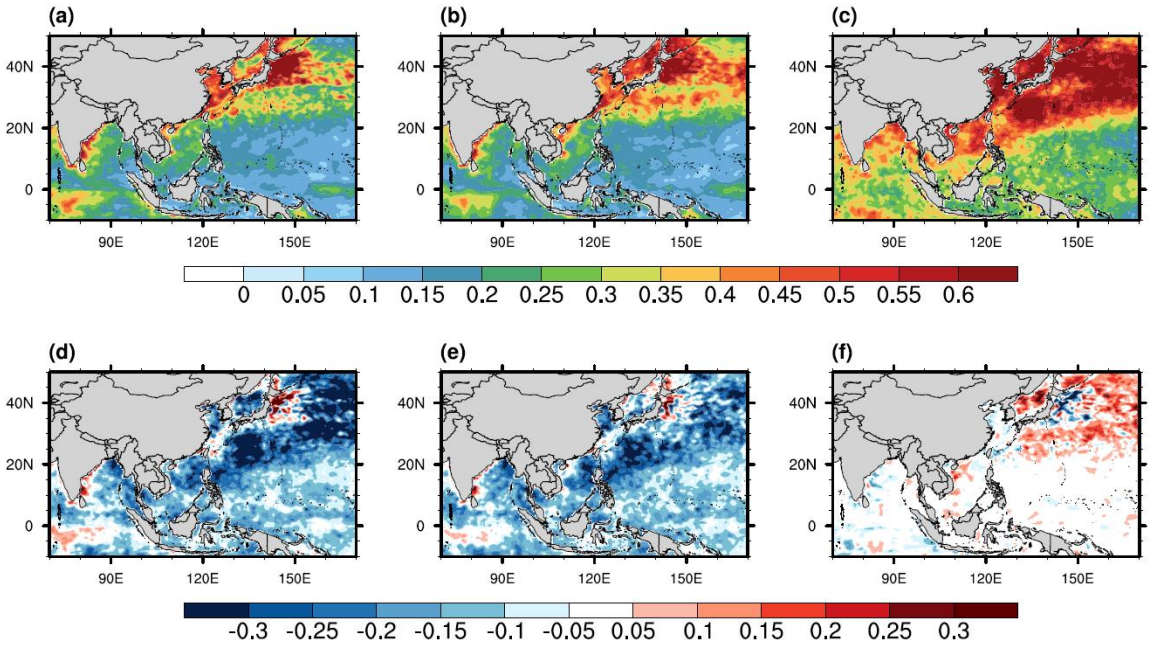

Figure 5.10 Standard deviation of intraseasonal (10-60-day) sea surface temperature (unit: °C) in the (a) EXP_30lev, (b) EXP_50lev and (c) observation, and difference between (d) EXP_30lev and observation (EXP_30lev minus observation), (e) EXP_50lev and observation (EXP_50lev minus observation) and (f) EXP_50lev with EXP_30lev (EXP_50lev minus EXP_30lev).

5.2.4 Contribution of surface heat fluxes to SST variation

Following the budget equation in chapter 4, contribution of net heat flux, shortwave radiation and latent heat flux to the SST variation is quantified in two experiments and observation (Figure 5.11). The magnitude of contribution percentage of net heat flux in EXP_50lev is much closer to the observation, compared with that in EXP_30lev (Figure 5.11 (a-c)). The reduction in the overestimated heat fluxes contribution to the SST variation is resulted from the improved mixed layer depth in EXP_50lev (Figure 5.9). The regional-averaged contribution percentage over South China Sea are reduced by 10% in the net heat flux, which is primarily caused by the reduced contribution percentage from shortwave radiation (Table 5.2).

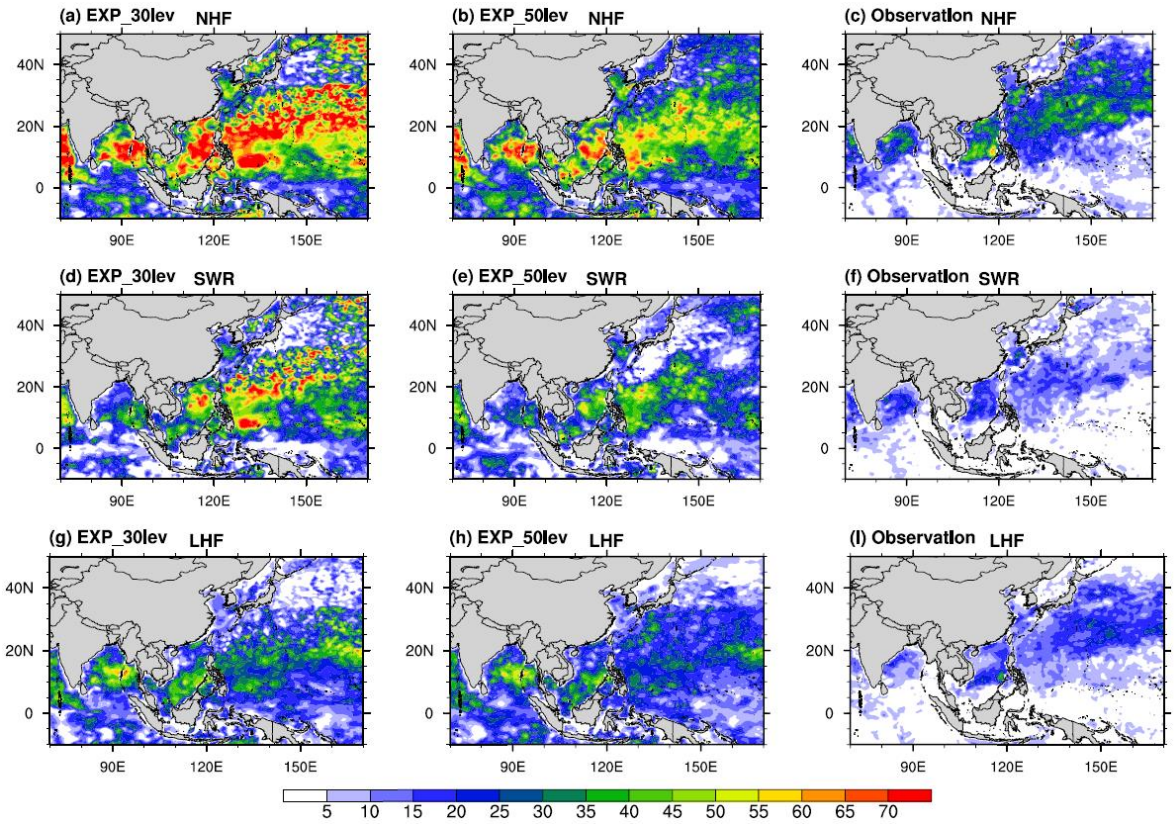

Figure 5.11 Percentage (unit: %) of MJJA SST tendency explained by net surface heat flux (a-c), shortwave radiation (d-f) and latent heat flux (g-i) in the EXP_30lev (left column), EXP_50lev(middle column) and observation(right column) during May-August. (The black box indicates South China Sea).

Table 5.2 Contribution percentage (unit: %) of MJJA surface heat fluxes to SST tendency over South China Sea during 1998-2000 (denoted by black box in Figure 4.4).

Contribution Percentage (%)	EXP_30lev	EXP_50lev	Observation
Net surface heat flux	**58**	**46**	**27**
Net shortwave radiation	**39**	**29**	**13**
Latent heat	**28**	**25**	**13**

5.3 Impacts of finer horizontal resolution

5.3.1 Experimental design

Two additional experiments at a horizontal resolutions of 25-km (i.e., EXP_Trop_25-km) and 10-km (i.e., EXP_Trop_10-km) are carried out to testify the finer resolution effects on the tropical intraseasonal climate simulation (Table 5.3). The simulation domain is slightly different in the 25-km and 10-km resolution runs (Figure 5.12). The simulation domain in 25-km resolution run is set to be in (15.543°S~15.76°N, 69.766°E~170.936°E). Considering the limitation of computer resources, the simulation domain in 10-km resolution is set to be (11.258°S~11.522°N, 75.611°E~165.541°E). The model outputs in this domain (10°S ~10°N, 79°E~ 162°E) are analyzed. Each experiment is integrated for one year (January 1st ~ December 31st 2001).

Table 5.3 List of experiments performed

Experiment Names	Model Components	Resolution (Grid number)	Integration Time
EXP_Trop_25km	Coupled atmosphere-ocean (RSM-ROMS)	25-km (142×451)	01/01/2001~ 31/12/2001
EXP_Trop_10km		10-km (256×1001)	

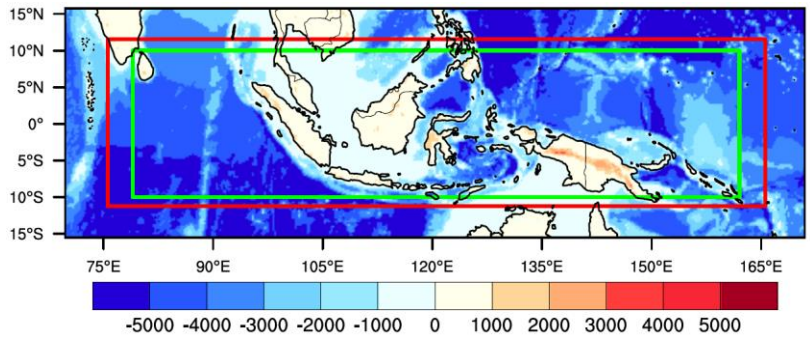

Figure 5.12 Simulation domain, model topography and bathymetry (unit: meter) from ETOPO5 for RSM-ROMS simulation. The whole domain indicates the 25-km simulation domain; the red box indicates the 10-km simulation domain; the green box indicates the analyzed domain.

5.3.2 Effects on intraseasonal variability

There are still less studies using the models with resolution going down to less than 10-km resolution, thus it is necessary to explore the model performances when the resolution goes down to 10-km resolution. Figure 5.13 illustrated the eastward propagation of the intraseasonal rainfall from January 1st to March 31st. It is found that the amplitude and direction of the propagating ISO during this strong MJO event is improved when the resolution is increased, in particular at the longitudes east of 110 °E. The pattern correlation against observation during the most intense period of the MJO event (around Jan 20th ~Feb 28th) increases from 0.36 in the EXP_Trop_25-km to 0.43 in the EXP_Trop_10-km. It is noted that the amplitude of the intraseasonal rainfall is slightly larger than that in Figure 3.5. This difference might be caused by some factors (e.g., simulation domain, integration starting time). Additionally, the two peak rainfall events occurred in early February (indicated by green dashed circle in Figure 5.14) over a small maritime region are better captured in the 10-km resolution run.

As for the northward propagation, it is found that the weaker amplitude of northward propagation could be improved at a higher-horizontal resolution (Misra et al., 2018). Thus, it is expected that the weaker amplitude of northward propagation ISO could be alleviated under the 10-km resolution if there are long-term finer-resolution simulations over larger domain.

Figure 5.15 illustrates the standard deviation of MJJAS intraseasonal precipitation. These two experiments exhibit the similar distribution with pattern correlation coefficient of 0.18 (0.19) in the experiment of EXP_Trop_25-km (EXP_Trop_10-km). The wet biases of intraseasonal rainfall over the Tropical Eastern Indian Ocean and the coastal region of Tropical Western Pacific are effectively alleviated. The dry bias in most oceanic regions of Tropical Indian Ocean and Western Pacific. The significant improvement could be found in the reduction of RMSE (4.17 mm/day in the EXP_Trop_25-km and 3.87 mm/day in the EXP_Trop_10-km). However, to make the conclusion more robust, the finer resolution effects on tropical climate should be tested based on long-term simulation experiments.

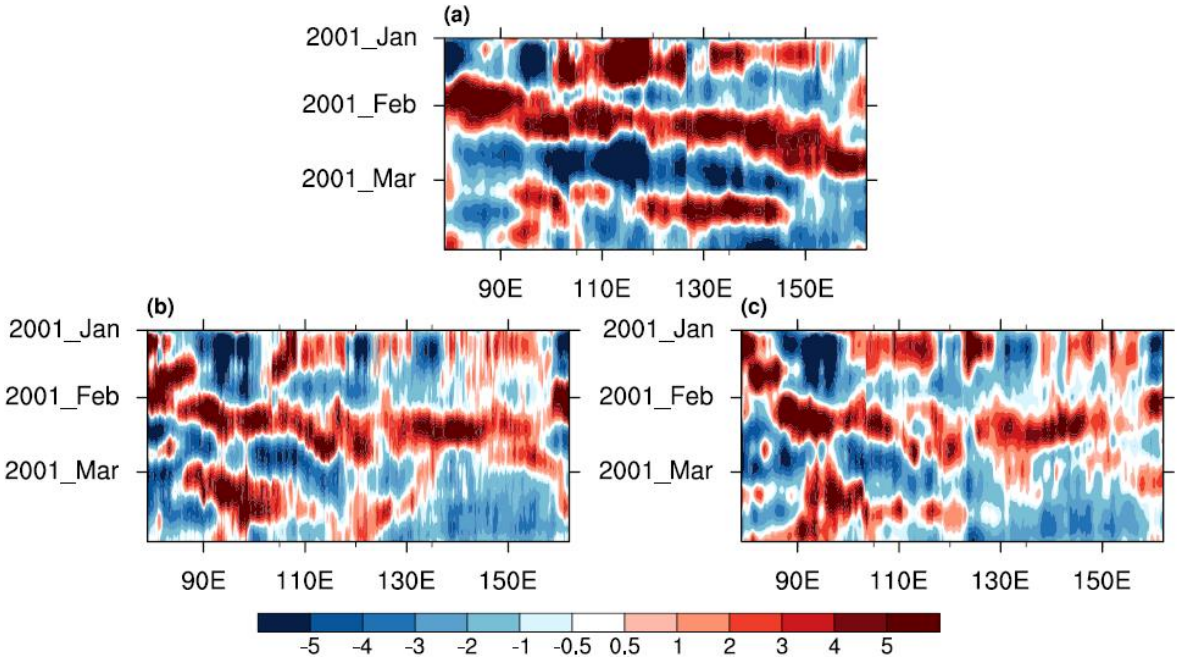

Figure 5.13 Time-longitude (10°S-10°N) diagram of intraseasonal (10-60-day) precipitation anomalies in the (a) observation, (b) EXP_Trop_10-km and (c) EXP_Trop_25-km during January-March 2001.

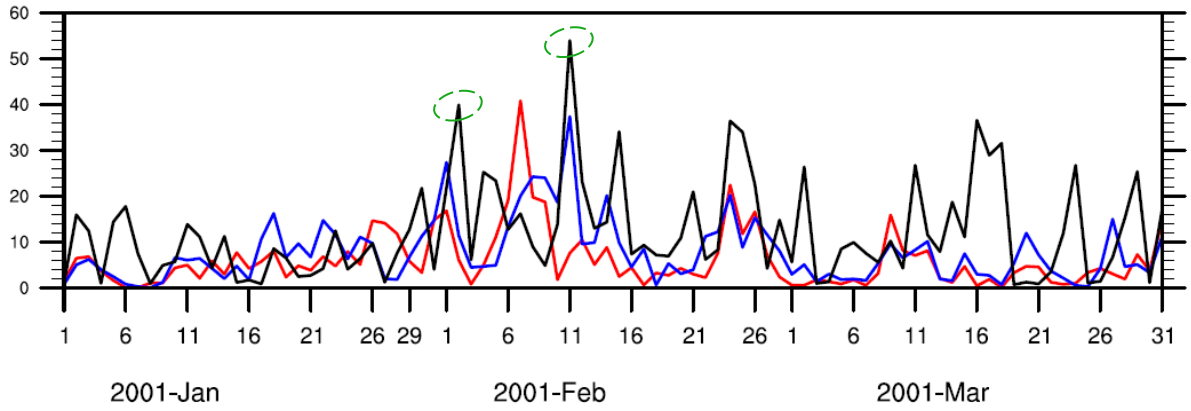

Figure 5.14 Time series of daily precipitation (unit: mm/day) over the sub-region (0-5°N, 145-150°E) in the experiment of EXP_Trop_10-km (blue line), EXP_Trop_25-km (red line) and observation (black line) during January-March 2001.

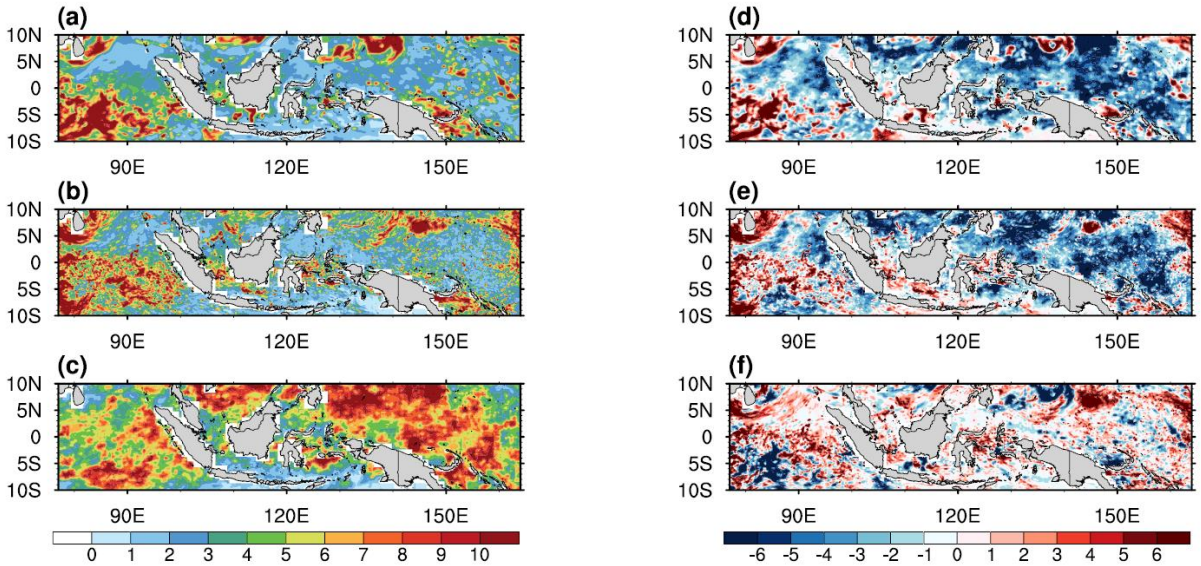

Figure 5.15 Standard deviation of MJJAS intraseasonal (10-60-day) precipitation (unit: mm/day) in the (a) EXP_Trop_25-km, (b) EXP_Trop_10-km, (c) TRMM_3B42 , and difference between (d) EXP_Trop_25-km and TRMM_3B42, (e) EXP_Trop_10-km and TRMM_3B42 and (f) EXP_Trop_10-km and EXP_Trop_25-km (the former minus the latter) in 2001.

5.3.3 Effects on ocean thermodynamics

The mean biases of the ocean temperature in the top 60 meters are shown in Figure 5.16(a-c). The pattern correlation of the ocean temperature is significantly increased. The cold biases are found in most of the Tropical oceanic regions at a coarser resolution (i.e., 25-km), in particular over Indian Ocean with the bias magnitude large than 2 °C. In the finer run (i.e., 10-km), the cooler ocean temperature in most regions are effectively alleviated, with the magnitude (larger than 1.5 °C) over the marine region. The regional averaged bias (RMSE) is reduced from -0.69 (1.08 °C) to -0.44 (0.75 °C). And the pattern distribution is also better reproduced in the 10-km resolution run with spatial correlation coefficient enhanced from 0.73 to 0.84.

In the section 5.2, it shows that the simulation of salinity in the maritime continents is degraded when the uppermost thickness is enhanced (Figure 5.16(d-f)). However, increasing the horizontal resolution has positive effects on the salinity simulation, which could effectively eliminate the higher salinity over the Maritime Continent. The pattern correlation (RMSE) increases (decreases) from 0.90(0.38 PSU) in the EXP_Trop_25-km to 0.93(0.31 PSU) in the EXP_Trop_10-km in the EXP_50lev. The combined effects of increasing horizontal and vertical

resolution should be examined, which might enhance the model skills in different aspects. It is expected that the ocean salinity could be improved when increasing horizontal resolution and introduction of river discharge are combined.

The shallower mixed layer depth in the Tropical Western Pacific and Indian is effectively improved (Figure 5.16(g-i)). The spatial correlation coefficient (RMSE) of mixed layer depth increases (decreases) from 0.44 (21.30 meters) to 0.50(17.89 meters). The finer horizontal resolution performs better at both high and low latitudes.

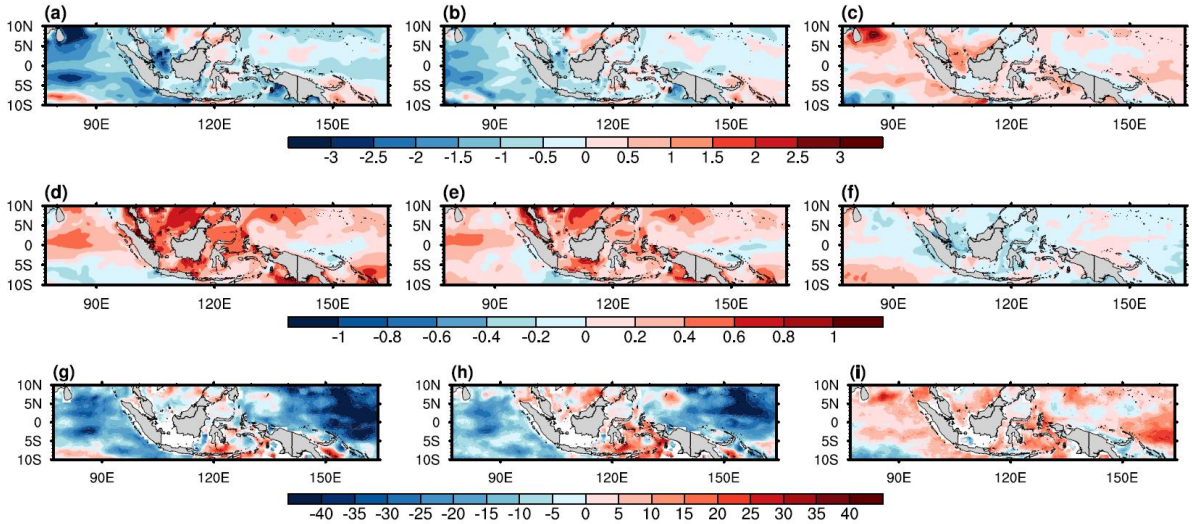

Figure 5.16 Difference in MJJAS ocean temperature (upper panel, unit: °C), ocean salinity (middle panel, unit: PSU) in the top 60 meters and mixed layer depth (lower panel, unit: meter) between EXP_Trop_25km and observation (left column), EXP_Trop_10km and observation (middle column) and EXP_Trop_10km and EXP_Trop_25km(right column) (the former minus the latter) in 2001.

5.3.4 Effects on sea surface temperature and surface net heat flux

The spatial patterns of differences in mean state of sea surface temperature are shown in Figure 5.17(d-f). Prominent negative biases occur over the Indian Ocean while positive bias over Western Pacific. In contrast with the significant improvement in upper ocean temperature, no fundamental improvement is found in the sea surface temperature when the horizontal resolution is increased. The pattern correlation (RMSE) is 0.86(0.51°C) and 0.86(0.47°C) in the experiment of EXP_Trop_25-km and EXP_Trop_10-km, respectively. This tiny change might be due to the

change in surface net heat flux (Figure 5.18). There are pronounced negative downward net heat flux over the entire tropical region. It is supposed that the negative surface net heat flux largely contributes to the cold SST bias over the Indian Ocean while the warmer SST bias over Tropical Western Pacific upper ocean thermodynamics could be attributed by the upper ocean thermodynamics. The pattern correlation (RMSE) is 0.74(42.48 W/m^2) and 0.69(47.77 W/m^2) in the experiment of EXP_Trop_25-km and EXP_Trop_10-km, respectively. The degradation in the surface net heat flux leads to the tiny change in sea surface temperature. In some sub-regions (e.g., Bay of Bengal, Tropical Western Pacific), the positive SST difference between two runs is corresponding to the negative downward net heat flux, this inconsistency between SST and surface heat flux indicates that the coupling processes in RSM-ROMS is still imperfect.

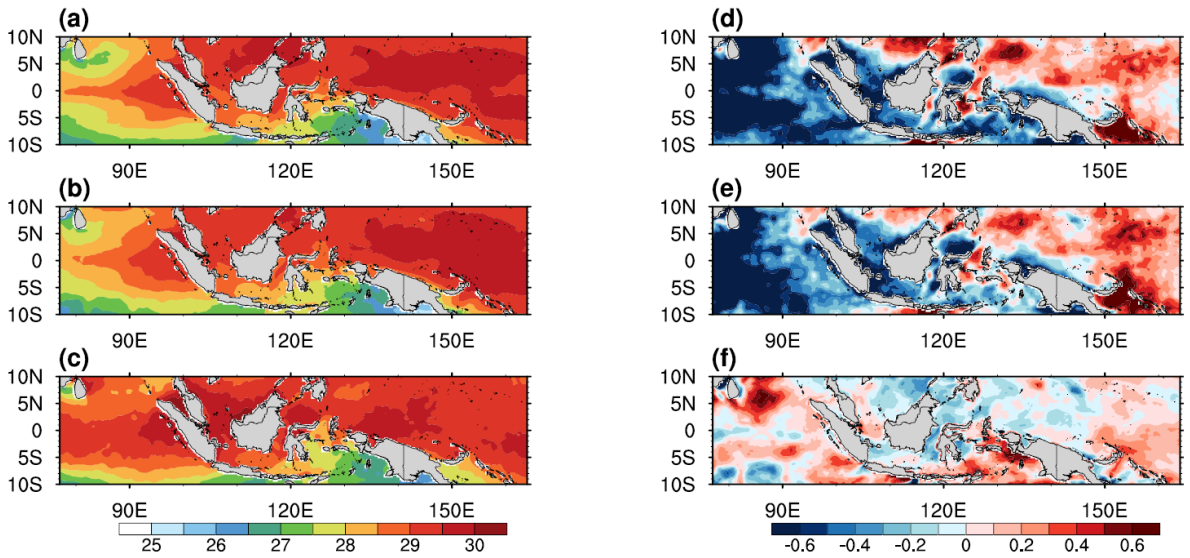

Figure 5.17 Mean state of MJJAS sea surface temperature (unit:°C) in the (a) EXP_Trop_25-km, (b) EXP_Trop_10-km, (c) observation, and difference between (d) EXP_Trop_25-km and observation, (e) EXP_Trop_10-km and observation and (f) EXP_Trop_10-km and EXP_Trop_25-km (the former minus the latter) in 2001.

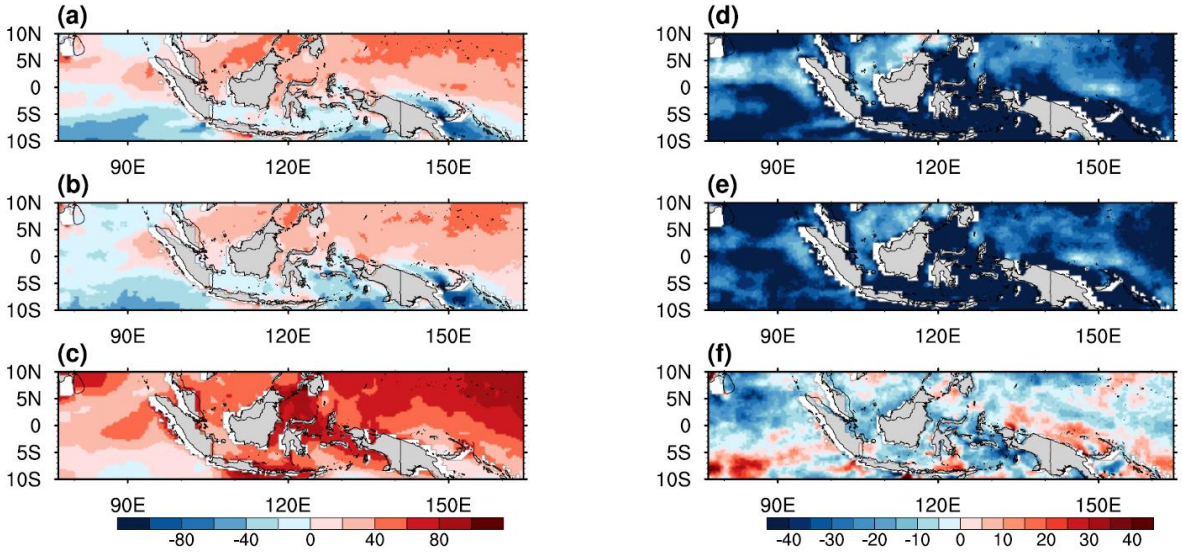

Figure 5.18 Same as Figure 5.17, but for the net downward surface heat flux (unit: W/m^2**)**.

5.4 Discussion

The coupling frequency in the above model simulation are 24 hours. To examine the impacts of coupling frequency on the simulation of intraseasonal variation, two-year (1998-1999) experiments with the coupling frequency of 1 hour (hereafter coupled_ fre1h) are conducted. The model outputs are compared with the coupled experiment with 24-hour coupling frequency (hereafter coupled_fre24h). Some previous studies (e.g., Ge et al., 2017) point out that increasing coupling frequency can lead to improved intraseasonal variation simulation. Interestingly, our results are slightly different from the previous studies. It shows that the intraseasonal precipitation did not improve in the 1-hour coupling frequency experiment (Figure 5.19). The spatial correlation coefficient (RMSE) is 0.32(2.62 mm/day) and 0.30(2.63 mm/day) in the whole domain for the experiment of coupled_fre24h and coupled_fre1h, respectively. Further analysis show that the there is no significant improvement in the temporal evolution of daily SST, precipitation and net heat flux during the monsoon season (Figure 5.20). Note that most of the previous studies are based on the global climate models, it is possible that our findings are model dependent.

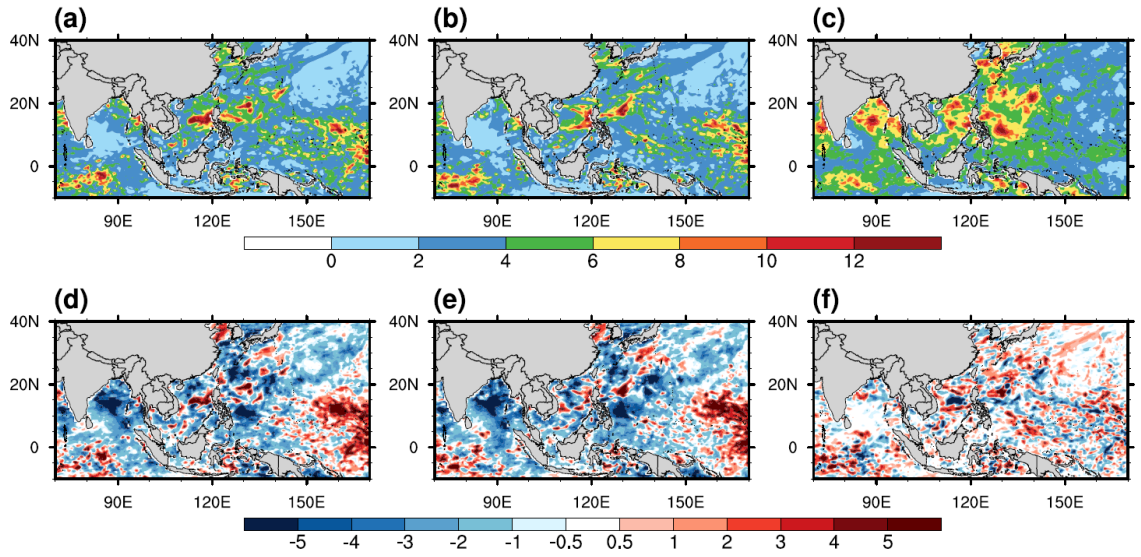

Figure 5.19 Standard deviation of MJJAS intraseasonal (10-60-day) precipitation variation (unit: mm/day) in the (a) coupled_fre24h, (b) coupled_ fre1h and (c) observation, and differences between (d) coupled and observation, (e) coupled_ fre1h and observation and (f) coupled and coupled_ fre1h (the former minus the latter) in 1999.

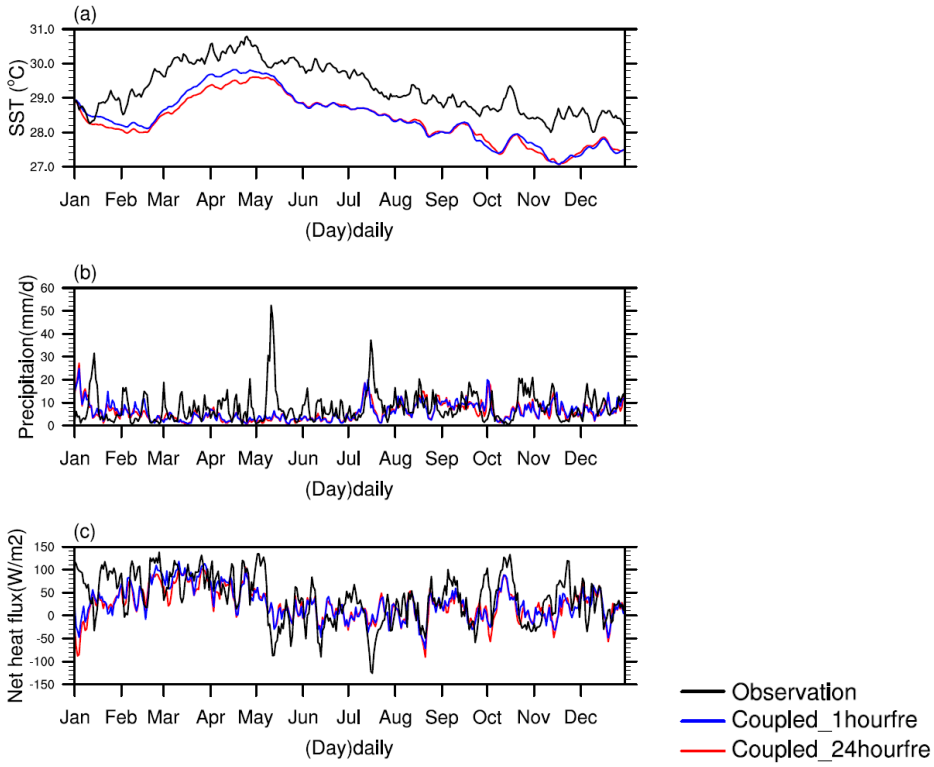

Figure 5.20 Time series of daily (a) sea surface temperature , (b) precipitation and (c) net surface heat flux in the experiment of coupled_fre24h (red solid line), coupled_fre1h (blue solid line), and observation(black solid line) over the Eastern Indian Ocean (5°S-5°N, 70°E-100°E) during January-December 1999.

5.5 Summary

The positive effects of the increased ocean model vertical resolution include: (a) the colder SST bias and lower SST intraseasonal variation in subtropical regions (e.g., Kuroshio-Oyashio Current region, Japan Sea) in warmer season is well removed due to the increasing uppermost thickness; (b) the shallower mixed layer depth over the Tropical Western Pacific and Indian Ocean is improved; (c) the contribution of net heat flux to intraseasonal SST variation is more realistically represented caused by the improved thermodynamics (e.g., mixed layer depth).

In another aspect, increasing horizontal resolution exhibits essential positive effects on the tropical climate. The intensity of boreal summer tropical intraseasonal rainfall is slightly improved as well as the eastward propagating MJO precipitation. The ocean thermodynamics (e.g., ocean temperature) is also reproduced more realistically, which provides an essential supplement for the studies in Chapter 2.

In generally, the benefit of increasing vertical resolution is apparent in the mean state SST, intraseasonal SST variation and mixed layer depth. The effects of vertical resolution on the oceanic state simulation rely more heavily on the region, compared with the effects of horizontal resolution. The combined effects of increasing horizontal and vertical resolution need to be further examined.

Chapter 6

Conclusions and future work

6.1 Summary and conclusions

The aim of this research is to provide a more general and comprehensive assessments of simulation skills for regional climate model RSM-ROMS and further combat the model deficiencies. Three diverse studies are carried out based on this fully coupled atmosphere-ocean regional climate model (RSM-ROMS).

First, chapter 2 aims to remove the pronounced cold summer SST bias over Subtropical Western North Pacific. A set of experiments are carried out by employing the two methods (i.e., flux adjustment and increasing model horizontal resolution), combined and separately.

The main conclusion could be draw as follows:

(a) Heat flux adjustment outperforms the non-flux adjustment in most aspects of climate simulation. Following by the improvement of cold SST biases, most near-surface atmospheric variables and some oceanic variables are also better reproduced.

(b) The increasing model resolution greatly contributes to the improvements in the simulation of ocean state (e.g., vertical motion, ocean currents, ocean heat content) throughout the whole ocean layers and Kuroshio Current path due to better representation of mesoscale eddy activities. The reduced positive wind stress curl bias in the Kuroshio coastal region partially contributes to the reduction in vertical upwelling.

Second, chapter 3 and chapter 4 aim to explore the benefit of air-sea coupling in the simulation of air-sea interaction by comparing the coupled model RSM-ROMS with the uncoupled model RSM. The main processes responsible to the intraseasonal SST variation are also clarified.

The main conclusion could be drown as follows:

(a) The intensity of summer intraseasonal precipitation variation is remarkably improved, in particular the pattern distribution. Air-sea coupling slightly improves some aspects of northward propagation simulation of boreal summer ISO in the near-equatorial region. The features (e.g., direction) of eastward propagating ISO in the strong boreal winter MJO events are also better captured.

(b) The observed features (e.g., response time, coupling intensity) of local intraseasonal SST-precipitation relationship are better reproduced by the coupled model due to a better

representation of air-sea feedbacks, particularly over Western Pacific. The uncoupled model RSM misrepresents these features due to the spurious SST forcing.

(c) The improved surface shortwave radiation-SST feedback in the coupled run is due to more realistic simulated cloud-SST feedback. The SST variation is primarily contributed by atmospheric processes in RSM-ROMS, but its relative contribution is overestimated possibly due to the shallower mixed layer.

With the aim to tackle the model deficiencies clarified in the second study, in chapter 5, we try to enhance the horizontal and ocean vertical resolution to obtain a better representation of the mean climate and intraseasonal variability.

The main conclusion could be drown as follows:

(a) In terms of the effects on mean climate, increasing horizontal resolution (10-km) could obtain generally better representations of ocean thermodynamics. Increased vertical resolution exhibits regional-dependence, which favors the SST simulation at higher latitude while improved thermodynamics (e.g., mixed layer depth) at lower latitudes.

(b) In terms of the effects on intraseasonal variabilities, increasing horizontal resolution has slight improvements in simulating the intensity of intraseasonal rainfall and MJO-related convection propagation while increased vertical resolution has little effects. Improved intraseasonal SST variation could be obtained in finer vertical resolution.

To conclude, this dissertation provides a comprehensive evaluation of RSM-ROMS performance in various aspects, which could make essential supplements for the previous studies. The fully AO coupled regional climate model RSM-ROMS is to some extent an effective and powerful tool to study the climate and conduct impact assessments for providing scientific basis for adaptation measures. By including the air-sea feedback, the coupled model RSM-ROMS could better simulate the natural climate system. In particular, the local intraseasonal SST-precipitation and boreal winter eastward propagating ISO is more realistically captured. In addition, increasing the horizontal and ocean model vertical resolution in the upper ocean leads to subtle but significant changes in the mean climate and intraseasonal variability over East Asia. In particular, enhancement of horizontal resolution has overall positive effects on the simulation of ocean thermodynamics over East Asia.

It is noted that the higher resolution is not always superior in simulating the atmospheric

variables such as the mean state of net heat flux in Tropical region, possibly implying that the model physical and dynamical configuration at this resolution might not be optimal. It confirms the necessities of the development of higher resolution coupled RCM with improved physics schemes. Additionally, the finest horizontal resolution is set to be 10-km in Tropical regions. It needs to analyze further whether the model still performs well or even better in the simulation of tropical intraseasonal activities when the resolution goes down to less than 10-km.

In another aspect, both the mean state climate and intraseasonal variabilities are assessed by the effects of increasing resolution, but it is hard to obtain a consensus of the model performance from such various aspects. It is necessary to focus on the specific scientific question such as some important climate phenomena related to air-sea interaction (e.g., MJO event, ENSO). In addition, the models still suffer from heavy computations with model resolution increased. Note that RSM and ROMS share the same grid, it should be well clarified how to choose the optimized horizontal resolution for the atmospheric and oceanic components of the coupled RCM, which could give some hints to fully utilize the available computation resources (Sein et al., 2018).

On the whole, we still have a long way to go to develop a coupled RCM with more realistic physical and thermodynamic processes.

6.2 Limitations and future work

There are still some limitations in this study, some further work needs to be conducted in future:

(a) The effects of increasing horizontal resolution are only based on one-year simulation outputs. It is necessary to conduct long-term simulations to confirm the robustness of improvement in the mean climate and intraseasonal variabilities (e.g., boreal winter eastward propagation ISO) under the effect of the higher resolution.

(b) The typical large meander path in 2004 summer only persists in short-time period when the horizontal resolution is enhanced. The underlying mechanism (e.g., evolution of mesoscale eddy activities) for this model discrepancy should be elucidated.

(c) The MJO simulation in RSM-ROMS still remains deficient such as weaker amplitude. More research is needed to examine the role of other factors (e.g., SST, wind, evaporation) in shaping the MJO event, which further clarifies the reason for the discrepancies and facilitates the accurate prediction of strong MJO events.

(d) The contribution from oceanic process should be estimated using the high-temporal

resolution dataset in order to provide a general assessment of mixed-layer heat budget simulation in RSM-ROMS.

(e) In this thesis, the effects of increased either horizontal resolution or ocean vertical resolution are evaluated without modifying the representation of physical processes in RSM-ROMS. The impacts of straightforward resolution increase are not overall positive. First, the shallower mixed layer depth is still prominent although it is slightly improved when the ocean vertical resolution is enhanced. Parameter tuning on the mixing scheme GLS is potentially an effective and fundamental approach to improve the upper-ocean thermodynamic simulation through modifying the vertical motion. Second, the boreal summer intraseasonal precipitation variation in the tropical regions did not exhibit pronounced improvement. Implementation of the model physics schemes in the atmospheric sub-model RSM is also needed to make a fundamental improvement. Third, to improve the freshwater flux and ocean salinity simulation in the coastal region, a river routing model CaMa-Flood with explicate representation of river discharge and flood stage (e.g., water level and flood area) needs be introduced in RSM-ROMS.

(f) To make the study more integratedly, combined effects of increasing horizontal and ocean vertical resolution need to be examined to check whether the optimized improvement in the model could be obtained.

(g) Only the local atmosphere-ocean interaction is elucidated in this study. Remote SST forcing also exhibits pronounced influence on the local intraseasonal variability through modifying the atmospheric and oceanic processes, which needs to be further explored.

References

Akhtar, N., J. Brauch, and B. Ahrens, 2018: Climate modeling over the Mediterranean Sea: impact of resolution and ocean coupling. *Clim. Dyn.*, **51**, 933–948, doi:10.1007/s00382-017-3570-8.

Ashfaq, M., C. B. Skinner, and N. S. Diffenbaugh, 2011: Influence of SST biases on future climate change projections. *Clim. Dyn.*, **36**, 1303–1319, doi:10.1007/s00382-010-0875-2.

Barnier, B., L. Siefridt, and P. Marchesiello, 1995: Thermal forcing for a global ocean circulation model using a three-year climatology of ECMWF analysis. *J. Mar. Sys.*,**6,** 363–380, doi: https://doi.org/10.1016/0924-7963(94)00034-9.

Carton, J. A., and B. S. Giese, 2008: A Reanalysis of Ocean Climate Using Simple Ocean Data Assimilation (SODA). *Mon. Weather Rev.*, **136**, 2999–3017, doi:10.1175/2007MWR1978.1.

Centre ERS d'Archivage et de Traitement, 2002: QuikSCAT scatterometer mean wind field products user manual, *Rep.C2 - MUT - W - 04 - IF*, Brest, France. [Available at ftp://ftp.ifremer.fr/ifremer/cersat/documentation/gridded/mwf-quikscat/mwf_vol2.pdf.]

Chelton, D. B., and S.-P. Xie, 2010: Coupled ocean–atmosphere interaction at oceanic mesoscales. *Oceanography*, **23**, 52–69. doi: 10.5670/oceanog.2010.05.

Dai, Y., H. Li, and L. Sun, 2018: The Simulation of East Asian Summer Monsoon Precipitation With a Regional Ocean-Atmosphere Coupled Model. *J. Geophys. Res. Atmos.*, 1–15, doi:10.1029/2018JD028541.

Ding, H., R. J. Greatbatch, M. Latif, and W. Park, 2015: The impact of sea surface temperature bias on equatorial Atlantic interannual variability in partially coupled model experiments. *Geophys. Res. Lett.*, **42**, 5540–5546, doi:10.1002/2015GL064799.

Dommenget, D., and M. Rezny, 2018: A Caveat Note on Tuning in the Development of Coupled Climate Models. *J. Adv. Model. Earth Syst.*, **10**, 78–97, doi:10.1002/2017MS000947.

Dunbar, S., and Coauthors, 2006: QuikSCAT science data product user manual, version 3.0, Doc. D-18053—Rev A, Jet Propul. Lab., Pasadena, Calif. [Available at ftp://podaac-ftp.jpl.nasa.gov/allData/quikscat/L2B/docs/ QSUG_v3.pdf.]

Ducet, N., P. Y. Le Traon, S. Oceanography, R. Saint-agne, and G. Reverdin, 2000: Global high-resolution mapping of ocean circulation. *J. Geophys. Res.*, **105**, 19477–19498. doi: 10.1029/2000JC900063.

Duvel, J. P., and J. Vialard (2007), Indo-Pacific sea surface temperature perturbations associated with intraseasonal oscillations of the tropical convection, *J. Clim.*, **20**, 3056–3082.

Ek, M. B., 2003: Implementation of Noah land surface model advances in the National Centers for Environmental Prediction operational mesoscale Eta model. *J. Geophys. Res.*, **108**, 8851, doi:10.1029/2002JD003296.

Fedorov, A. V, 2008: Ocean-Atmosphere Coupling. *Oxford Companion to Glob. Chang.*, 369–374.

Feng, X., K. Haines, C. Liu, E. de Boisséson, and I. Polo, 2018: Improved SST-Precipitation Intraseasonal Relationships in the ECMWF Coupled Climate Reanalysis. *Geophys. Res. Lett.*, **45**, 3664–3672, doi:10.1029/2018GL077138.

Gao, Y., N. P. Klingaman, C. A. DeMott, and P. C. Hsu, 2019: Diagnosing Ocean Feedbacks to

the BSISO: SST-Modulated Surface Fluxes and the Moist Static Energy Budget. *J. Geophys. Res. Atmos.*, **124**, 146–170, doi:10.1029/2018JD029303.

Ge, X., W. Wang, A. Kumar, and Y. Zhang, 2017: Importance of the vertical resolution in simulating SST diurnal and intraseasonal variability in an oceanic general circulation model. *J. Clim.*, **30**, 3963–3978, doi:10.1175/JCLI-D-16-0689.1.

Giorgi, F., and X.-J. Gao, 2018: Regional earth system modeling: review and future directions. *Atmos. Ocean. Sci. Lett.*, **11**, 189–197, doi:10.1080/16742834.2018.1452520.

Giorgi, F., 2019: Thirty years of regional climate modeling: Where are we and where are we going next? *J. Geophys. Res. Atmos.*, 2018JD030094, doi:10.1029/2018JD030094.

Ham, S., K. YOSHIMURA, and H. LI, 2016: Historical Dynamical Downscaling for East Asia with the Atmosphere and Ocean Coupled Regional Model. *J. Meteorol. Soc. Japan. Ser. II*, **94A**, 199–208, doi:10.2151/jmsj.2015-046.

Han, Z.-Y., T.-J. Zhou, and L.-W. Zou, 2012: Indian Ocean SST biases in a Flexible Regional Ocean Atmosphere Land System (FROALS) model. *Atmos. Oceanic Sci. Lett.*, **5**, 273-279, doi:10.1080/16742834.2012.11447012

Harris, C. M., 2018: Coupled atmosphere-ocean modelling. GODAE Oceanview International School in "New Frontiers in Operational Oceanography", E. P. Chassignet, A. Pascual, J. Tintore, and J. Verron, Eds.

He, Z., R. Wu, W. Wang, Z. Wen, and D. Wang, 2017: Contributions of surface heat fluxes and oceanic processes to tropical SST changes: Seasonal and regional dependence. *J. Clim.*, **30**, 4185–4205, doi:10.1175/JCLI-D-16-0500.1.

Hong, S.-Y., and E.-C. Chang, 2012: Spectral nudging sensitivity experiments in a regional climate model. *Asia-Pacific J. Atmos. Sci.*, 48, 345–355, doi: https://doi.org/10.1007/s13143-012-0033-3.

Hu, W., A. Duan, and G. Wu, 2015: Impact of subdaily air-sea interaction on simulating intraseasonal oscillations over the tropical Asian monsoon region. *J. Clim.*, **28**, 1057–1073, doi:10.1175/JCLI-D-14-00407.1.

Huang, Q., S. Yao, and Y. Zhang, 2012: Analysis of Local Air-Sea Interaction in East Asia Using a Regional Air-Sea Coupled Model. *J. Clim.*, **25**, 767–776, doi:10.1175/2011jcli3783.1.

Huffman, G. J., R. F. Adler, M. M. Morrissey, D. T. Bolvin, S. Curtis, R. Joyce, B. McGavock, and J. Susskind, 2002: Global Precipitation at One-Degree Daily Resolution from Multisatellite Observations. *J. Hydrometeorol.*, **2**, 36–50, doi:10.1175/1525-7541(2001)002<0036:gpaodd>2.0.co;2.

——, and Coauthors, 2007: The TRMM Multisatellite Precipitation Analysis (TMPA): Quasi-Global, Multiyear, Combined-Sensor Precipitation Estimates at Fine Scales. *J. Hydrometeorol.*, **8**, 38–55, doi:10.1175/JHM560.1. http://journals.ametsoc.org/doi/abs/10.1175/JHM560.1.

——, and E. Al., 2007: The Global Precipitation Climatology Project (GPCP) combined dataset. *J. Hydrometeorol.*, **8**, 78, 5e20. doi: 10.1175/1520-0477(1997)078<0005:TGPCPG>2.0.CO;2.

Juang, H-M. H., and M. Kanamitsu, 1994: The NMC nested Regional Spectral Model. *Mon. Wea. Rev.*, **122**, 3–26, doi : 10.1175/1520-0493(1994)122<0003:TNNRSM>2.0.CO;2.

Juang, H. M. H., S. Y. Hong, and M. Kanamitsu, 1997: The NCEP Regional Spectral Model: An

Update. *Bull. Am. Meteorol. Soc.*, **78**, 2125–2143, doi:10.1175/1520-0477(1997)078<2125:TNRSMA>2.0.CO;2.

Kako, S., T. Nakagawa, K. Takayama, N. Hirose, and A. Isobe, 2016: Impact of Changjiang River Discharge on Sea Surface Temperature in the East China Sea. *J. Phys. Oceanogr.*, **46**, 1735–1750, doi:10.1175/jpo-d-15-0167.1.

Kanamitsu, M., W. Ebisuzaki, J. Woollen, S.-K. Yang, J. J. Hnilo, M. Fiorino, and G. L. Potter, 2002: NCEP-DOE AMIP-II Renalalysys (R-2). *Bull. Am. Meteorol. Soc.*, **83**, 1631–1643, doi:10.1175/BAMS-83-11.

Kawabe, M., 1995: Variations of current path, velocity, and volume transport of the Kuroshio in relation with the large meander. *J. Phys. Oceanogr.*, **25**, 3103–3117, doi: https://doi.org/10.1175/1520-0485(1995)025<3103:VOCPVA>2.0.CO;2.

Klingaman, N. P., and S. J. Woolnough, 2014: The role of air-sea coupling in the simulation of the Madden-Julian oscillation in the Hadley Centre model. *Q. J. R. Meteorol. Soc.*, **140**, 2272–2286, doi:10.1002/qj.2295.

Klingaman, N. P., P. M. Inness, H. Weller, and J. M. Slingo, 2008: The importance of high-frequency sea surface temperature variability to the intraseasonal oscillation of Indian monsoon rainfall. *J. Clim.*, **21**, 6119–6140, doi:10.1175/2008JCLI2329.1.

Kumar, A., L. Zhang, and W. Wang, 2012: Sea Surface Temperature–Precipitation Relationship in Different Reanalyses. *Mon. Weather Rev.*, **141**, 1118–1123, doi:10.1175/mwr-d-12-00214.1.

Miyazawa, Y., X. Guo, and T. Yamagata, 2004: Roles of Mesoscale Eddies in the Kuroshio Paths. *J. Phys. Oceanogr.*, **34**, 2203–2222, doi:10.1175/1520-0485(2004)034<2203:romeit>2.0.co;2.

Praveen Kumar, B., J. Vialard, M. Lengaigne, V. S. N. Murty, M. J. McPhaden, M. F. Cronin, F. Pinsard, and K. Gopala Reddy, 2013: TropFlux wind stresses over the tropical oceans: Evaluation and comparison with other products. *Clim. Dyn.*, **40**, 2049–2071, doi:10.1007/s00382-012-1455-4.

Large, W. G., J. C. Mcwilliams, and S. C. Doney, 1994: Oceanic With Vertical Mixing : a Review Layer and a Model a Nonlocal Boundary. *Rev. Geophys.*, **32**, 363–403, doi:10.1029/94rg01872.

Li, H., M. Kanamitsu, and S. Y. Hong, 2012: California reanalysis downscaling at 10 km using an ocean-atmosphere coupled regional model system. *J. Geophys. Res. Atmos.*, **117**, 1–16, doi:10.1029/2011JD017372.

——, ——, ——, K. Yoshimura, D. R. Cayan, V. Misra, and L. Sun, 2014: Projected climate change scenario over California by a regional ocean–atmosphere coupled model system. *Clim. Change*, **122**, 609–619, doi:10.1007/s10584-013-1025-8.

Manabe, Syukuro, and Kirk Bryan. "Climate calculations with a combined ocean-atmosphere model." *Journal of the Atmospheric Sciences* 26.4 (1969): 786-789.

Mellor, G. L., and T. Yamada, 1982: Development of a turbulence closure model for geophysical fluid problems. *Rev. Geophys. Space Phys.*, **20,** 851–875. doi: 10.1029/RG020i004p00851

Milinski, S., J. Bader, H. Haak, A. C. Siongco, and J. H. Jungclaus, 2016: High atmospheric horizontal resolution eliminates the wind-driven coastal warm bias in the southeastern tropical Atlantic. *Geophys. Res. Lett.*, **43**, 10,455-10,462, doi:10.1002/2016GL070530.

Misra, V., A. Mishra, and A. Bhardwaj, 2018: Simulation of the intraseasonal variations of the Indian summer monsoon in a regional coupled ocean-atmosphere model. *J. Clim.*, **31**, 3167–3185, doi:10.1175/JCLI-D-17-0434.1.

Moorthi, S., and M. J. Suarez, 1992: Relaxed Arakawa-Schubert. A parameterization of moist convection for general circulation models. *Mon. Wea. Rev.*, **120,** 978–1002, doi: 10.1175/1520-0493(1992)120<0978:RASAPO>2.0.CO;2.

Pan, X., B. Huang, and J. Shukla, 2011: Sensitivity of the tropical Pacific seasonal cycle and ENSO to changes in mean state induced by a surface heat flux adjustment in CCSM3. *Clim. Dyn.*, **37**, 325–341, doi:10.1007/s00382-010-0923-y.

Peatman, S. C., and N. P. Klingaman, 2018: The Indian summer monsoon in MetUM-GOML2.0: Effects of air-sea coupling and resolution. *Geosci. Model Dev.*, **11**, 4693–4709, doi:10.5194/gmd-11-4693-2018.

Pookkandy, B., D. Dommenget, N. Klingaman, S. Wales, C. Chung, C. Frauen, and H. Wolff, 2016: The role of local atmospheric forcing on the modulation of the ocean mixed layer depth in reanalyses and a coupled single column ocean model. *Climate Dyn.*, **47**, 2991–3010, doi: 10.1007/s00382-016-3009-7.

Prodhomme, C., P. Terray, S. Masson, T. Izumo, T. Tozuka, and T. Yamagata, 2014: Impacts of Indian Ocean SST biases on the Indian Monsoon: As simulated in a global coupled model. *Clim. Dyn.*, **42**, 271–290, doi:10.1007/s00382-013-1671-6.

Qiu, B., 2002: The Kuroshio Extension system: Its large-scale variability and role in the midlatitude ocean–atmosphere interaction. *J. Oceanogr.*, **58,** 57–75, doi:10.1023/A:1015824717293.

Qiu, C., H. Kawamura, H. Mao, and J. Wu, 2015: Sea surface height and mixed layer depth responses to sea surface temperature in northwestern Pacific subtropical front zone from spring to summer. *Ocean Sci. Discuss.*, **12**, 83-101, doi:10.5194/osd-12-83-2015.

Rajendran, K., R. S. Nanjundiah, S. Gadgil, and J. Srinivasan, 2012: How good are the simulations of tropical SST-rainfall relationship by IPCC AR4 atmospheric and coupled models? *J. Earth Syst. Sci.*, **121**, 595–610, doi:10.1007/s12040-012-0185-7.

Reynolds, R. W., T. M. Smith, C. Liu, D. B. Chelton, K. S. Casey, and M. G. Schlax, 2007: Daily high-resolution-blended analyses for sea surface temperature. *J. Climate*, 20, 5473–5496, doi: 10.1175/2007JCLI1824.1.

Roxy, M., Y. Tanimoto, B. Preethi, P. Terray, and R. Krishnan, 2013: Intraseasonal SST-precipitation relationship and its spatial variability over the tropical summer monsoon region. *Clim. Dyn.*, **41**, 45–61, doi:10.1007/s00382-012-1547-1.

Rummukainen, M., 2010: State-of-the-art with regional climate models. *Wiley Interdiscip. Rev: Climate Change*, **1**, 82–96. doi:10.1002/wcc.008.

Sandeep, K. K., V. Pant, M. S. Girishkumar, and A. D. Rao, 2018: Impact of riverine freshwater forcing on the sea surface salinity simulations in the Indian Ocean. *J. Mar. Syst.*, **185**, 40–58, doi:10.1016/j.jmarsys.2018.05.002. https://doi.org/10.1016/j.jmarsys.2018.05.002.

Sausen, R., K. Barthel, and K. Hasselmann, 1988: Coupled ocean–atmosphere models with flux correction. *Climate Dyn.*, **2**, 145–163, doi: 10.1007/BF01053472.

Schrum, C., 2017: Regional Climate Modeling and Air-Sea Coupling. In Oxford Research Encyclopedia of Climate Science. doi:10.1093/acrefore/9780190228620.013.3.

Sein, D. V., and Coauthors, 2018: The Relative Influence of Atmospheric and Oceanic Model Resolution on the Circulation of the North Atlantic Ocean in a Coupled Climate Model. *J. Adv. Model. Earth Syst.*, **10**, 2026–2041, doi:10.1029/2018MS001327.

Sharmila, S., and Coauthors, 2013: Role of ocean-atmosphere interaction on northward propagation of Indian summer monsoon intra-seasonal oscillations (MISO). *Clim. Dyn.*, **41**, 1651–1669, doi:10.1007/s00382-013-1854-1.

Shchepetkin, A. F., and J. C. McWilliams, 2003: A method for computing horizontal pressure-gradient force in an oceanic model with a nonaligned vertical coordinate. *J. Geophys. Res.*, **108**, 3090, doi: 10.1029/2001JC001047.

Shelly, A., P. Xavier, D. Copsey, T. Johns, J. M. Rodríguez, S. Milton, and N. Klingaman, 2014: Coupled versus uncoupled hindcast simulations of the Madden-Julian Oscillation in the Year of Tropical Convection. *Geophys. Res. Lett.*, **41**, 5670–5677, doi:10.1002/2013GL059062.

Slingo, J. M., 1987: The Development and Verification of A Cloud Prediction Scheme For the Ecmwf Model. *Q. J. R. Meteorol. Soc.*, **113**, 899–927, doi:10.1002/qj.49711347710.

Song, Z., S. K. Lee, C. Wang, B. P. Kirtman, and F. Qiao, 2015: Contributions of the atmosphere-land and ocean-sea ice model components to the tropical Atlantic SST bias in CESM1. *Ocean Model.*, **96**,280–290,doi:10.1016/j.ocemod.2015.09.008.

Tian, H., Q. Yang, R. G. Najjar, W. Ren, M. A. M. Friedrichs, C. S. Hopkinson, and S. Pan, 2015: Journal of Geophysical Research: Biogeosciences. *J. Geophys. Res. Biogeosciences*, **120**, 752–772, doi:10.1002/2014JG002760.

Tompkins, A. M., 2001: On the relationship between tropical convection and sea surface temperature. *J. Clim.*, **14**, 633–637, doi:10.1175/1520-0442(2001)014<0633:OTRBTC>2.0.CO;2.

Tseng, W. L., B. J. Tsuang, N. S. Keenlyside, H. H. Hsu, and C. Y. Tu, 2015: Resolving the upper-ocean warm layer improves the simulation of the Madden–Julian oscillation. *Clim. Dyn.*, **44**, 1487–1503, doi:10.1007/s00382-014-2315-1.

Umakanth, U., and A. P. Kesarkar, 2018: Performance evaluation of regional climate model to simulate sub-seasonal variability of Indian Summer Monsoon. *Clim. Dyn.*, **50**, 3595–3612, doi:10.1007/s00382-017-3827-2.

Umlauf, L., and H. Burchard, 2003: A generic length-scale equation for geophysical turbulence models. *J. Mar. Res.*, **61**, 235–265, doi:10.1357/002224003322005087.

Vinogradova, N. T., and R. M. Ponte, 2013: Clarifying the link between surface salinity and freshwater fluxes on monthly to interannual time scales. *J. Geophys. Res. Ocean.*, **118**, 3190–3201, doi:10.1002/jgrc.20200.

Wang, C., Zou, L., & Zhou, T. (2018). SST biases over the Northwest Pacific and possible causes in CMIP5 models. *Science China Earth Sciences*, *61*(6), 792–803. https://doi.org/10.1007/s11430-017-9171-8

Wang, S., C. Dieterich, R. Döscher, A. Höglund, R. Hordoir, H. E. Markus Meier, P. Samuelsson, and S. Schimanke, 2015: Development and evaluation of a new regional coupled atmosphere-ocean model in the North Sea and Baltic Sea. *Tellus, Ser. A Dyn. Meteorol. Oceanogr.*, **67**, doi:10.3402/tellusa.v67.24284.

Warner, J. C., C. R. Sherwood, H. G. Arango, and R. P. Signell, 2005: Performance of four turbulence closure models implemented using a generic length scale method. *Ocean Model.*,

8, 81–113, doi:10.1016/j.ocemod.2003.12.003.

Wu, R., and B. P. Kirtman, 2007: Regimes of seasonal air-sea interaction and implications for performance of forced simulations. *Clim. Dyn.*, **29**, 393–410, doi:10.1007/s00382-007-0246-9.

Wu, R., Cao, X., & Chen, S. ‐ F. (2015). Co ‐ variations of SST and surface heat flux on 10–20 ‐ day and 30–60 ‐ day time scales over the South China Sea and western North Pacific. J. Geophys. Res. Atmos., **120**, 12,486– 12,499, doi: 10.1002/2015JD024199

——, and T. You, 2018: Summer Intraseasonal Surface Heat Flux-Sea Surface Temperature Relationship Over Northern Tropical Indo-Western Pacific in Climate Models. *J. Geophys. Res. Atmos.*, **123**, 5859–5880, doi:10.1029/2018JD028468.

Wei, J., P. Malanotte-Rizzoli, E. A. B. Eltahir, P. Xue, and D. Xu, 2014: Coupling of a regional atmospheric model (RegCM3) and a regional oceanic model (FVCOM) over the maritime continent. *Clim. Dyn.*, **43**, 1575–1594, doi:10.1007/s00382-013-1986-3.

Xu, H., H. Tokinaga, and S. P. Xie, 2010: Atmospheric effects of the Kuroshio large meander during 2004-05. *J. Clim.*, **23**, 4704–4715, doi:10.1175/2010JCLI3267.1.

Yu, L., X. Jin, and R. A. Weller, 2008: Multidecade global flux datasets from the Objectively Analyzed Air–Sea Fluxes (OAFlux) Project: Latent and sensible heat fluxes, ocean evaporation, and related surface meteorological variables. *Woods Hole Oceanogr. Inst. OAFlux Proj. Tech. Rep.*, 1–64, doi:10.1007/s00382-011-1115-0.

Zhang, Y., W. B. Rossow, A. A. Lacis, V. Oinas, and M. I. Mishchenko, 2004: Calculation of radiative fluxes from the surface to top of atmosphere based on ISCCP and other global data sets: Refinements of the radiative transfer model and the input data. *J. Geophys. Res. Atmos.*, **109**, 1–27, doi:10.1029/2003JD004457.

Zhang, Y., M.-P. Hung, W. Wang, and A. Kumar, 2019: Role of SST feedback in the prediction of the boreal summer monsoon intraseasonal oscillation. *Clim. Dyn.*, doi:10.1007/s00382-019-04753-w. http://link.springer.com/10.1007/s00382-019-04753-w.

Zou, L., and T. Zhou, 2011: Sensitivity of a regional ocean-atmosphere coupled model to convection parameterization over western North Pacific. *J. Geophys. Res. Atmos.*, **116**, doi:10.1029/2011JD015844.

——, and ——, 2013: Can a regional ocean-atmosphere coupled model improve the simulation of the interannual variability of the western North Pacific summer monsoon? *J. Clim.*, **26**, 2353–2367, doi:10.1175/JCLI-D-11-00722.1.

Zuidema, P., and Coauthors, 2016: Challenges and prospects for reducing coupled climate model sst biases in the eastern tropical atlantic and pacific oceans: The U.S. Clivar eastern tropical oceans synthesis working group. *Bull. Am. Meteorol. Soc.*, **97**, 2305–2327, doi:10.1175/BAMS-D-15-00274.1.